Università degli Studi "Federico II" di Napoli

Dottorato Internazionale

in

Tecnologie Innovative per Materiali, Sensori ed Imaging

21° Ciclo

Characterization of epitaxial thin films and multilayers of manganites

Thesis by

Dr. Nathascia Lampis

Coordinatore:

Prof. Giancarlo Abbate

Contents

Used abbreviations

AF: Antiferromagnetic

AFI: Antiferromagnetic Insulating

AFM: Antiferromagnetic Metallic, Atomic Force Microscopy

CMR: Colossal Magnetoresistance

CE: Charge Exchange

CO: Charge Ordering

FC: Field cooled

FM: Ferromagnetic

FMM: Ferromagnetic Metallic

HREM: High Resolution Electron Microscopy

HRXRD: High Resolution X-ray Diffraction

JT: Jahn Teller

LAO: $LaAlO_3$

LSMO: $La_{1-x}Sr_xMnO_3$, $La_{0.7}Sr_{0.3}MnO_3$

MI: Metal-Insulator

MODA: Modular facility for the Oxides Deposition and Analysis

MR: Magneto Resistance

MTJ: Magnetic Tunnel Junction

NGO: $NdGaO_3$

OO: Orbital Ordering

PLD: Pulsed Laser Deposition

PM: Paramagnetic

PMI: Paramagnetic Insulator

PMM: Paramagnetic Metallic

RHEED: Reflection High Energy Electron Diffraction

RSG: Reentrant Spin Glass

SG: Spin glass

STM: Scanning Tunnelling Microscopy

STO: $SrTiO_3$

T_C: Curie Temperature

TMO: Transition Metal Oxides

UHV: High Ultra vacuum

ZFC: Zero field cooled

XPS: X-ray Photoelectron Spectroscopy

XRR: X-Ray Reflectivity

Introduction

The up-to-date electronics is based on classical semiconductors, but the technological development has generated an increasing request of new materials. Moreover, in a few years the microchips based on classical semiconductors will reach up their physical limit. This limit could be overthrow by the advent of a digital logic based on quantum effects, in which the information is elaborated through the polarization of the spin of the electrons (spintronics), doubling the information transported by the carriers (charge + spin). In this respect, a fundamental result was the observation that the alignment of spins can be preserved during the passage across the interface between different materials. Besides, new materials and techniques are required to develop devices of new conception. In this respect, the progress in the techniques devoted to the growth of thin films has created the premises for the discovery and the application of new multifunctional oxides and for their integration in complex multilayer devices. Such materials have enormous applicative interest, so much to constitute the foundation of a new important field of the electronic industry called "oxide electronics".

The basic idea of the oxide electronic is that it is possible to realize new devices by using thin films deposited in an ordered way onto crystalline substrates (epitaxial films), with the aim of obtaining special structures and physical properties. Integration of multifunctional oxides in devices requires a good compatibility between oxides and substrates, as well as between materials with different physical properties (ferroelectricity, magnetism, transport). The transition metal oxides (TMO) that crystallize in variants of the perovskite structure ABO_3 are the most suitable materials for their complex behavior, which includes such phenomena as high T_C superconductivity, multiferroicity and colossal magnetoresistance (CMR). The TMO properties can change drastically when they are deposited as epitaxial film; due to the effect of the adhesion forces to the substrate, in the deposition plane the films are subject to biaxial tensile strain or to biaxial compressive strain, determining physical properties that are not obtainable in massive samples. For sufficiently small thickness the epitaxial films show a long range deformation (pseudomorphous) and are lacking in relaxation defects as dislocations or twinnings. This is an

important factor for the application in the devices, in which the control of the quality of surfaces and interfaces pushed to the atomic level is essential.

Object of this research is the characterization of the chemical, structural and physical property of epitaxial thin films and multilayers of manganites, a class of transition metals oxides, also with regards to surfaces and interfaces, by means of advanced techniques of surveying.

In the activity carried out within the doctorate, thin and ultrathin epitaxial films of perovskite manganites have been studied. The characterized thin films and multilayers have been deposited with the system called MODA (Modular facility for Oxide Deposition and Analysis), at the CNR-INFM Coherentia laboratory, c.o. the Physics department of the University of Napoli "Federico II". MODA is a multi-chamber system for the deposition by laser ablation of targets of different crystalline materials. The growth of the film is controlled in situ by a modified RHEED (Reflection High Energy Electron Diffraction) that can operate in regime of high pressure. The films are transferred to the analytic chambers of surface characterization by means of manipulators in UHV (High Ultra vacuum), so to not contaminate the surface.

The characterization of the samples has been performed by means of the in situ techniques: RHEED, X-ray Photoelectron Spectroscopy (XPS), and by ex situ techniques, as High Resolution X-ray Diffraction (HRXRD) and X-ray Reflectivity (XRR), High Resolution Electron Microscopy (HREM), that give both long range crystallographic properties and the real structure of films, and SQUID magnetometry. The HRXRD, XRR and magnetic characterization has been carried out under the supervision of Dr. A. Geddo Lehmann and Dr. F. Congiu of the Physics department of the University of Cagliari.

The investigated materials are $La_{0.7}Sr_{0.3}MnO_3$ (LSMO) and $Pr_{1-x}Ca_xMnO_3$ (PCMO) thin films, which are members of the manganites family. The manganites, deposited as thin film, present physical property of remarkable interest as the phenomenon of the CMR and are widely studied for possible technological outcomes in the field of the spintronics, as good substitutes for giant magnetoresistive (GMR) materials already successfully used in devices for microelectronics. The films deposited in the MODA laboratory have been characterized with the aim to determine the best conditions concerning chemical, structure, and physical property and in order to determine the

influence of the structural properties, as the strain (varying the substrate or its orientation on which the film is deposited), on the magnetic and transport properties. The films and multilayers characterization also concerns the surface and interfaces properties. Therefore, thin films with different stoichiometry (having varied the doping) and manganitic multilayers have been deposited and then structurally, magnetically characterized.

The thesis is divided in four chapters, in which the characterization of $La_{0.7}Sr_{0.3}MnO_3$ and $Pr_{1-x}Ca_xMnO_3$ thin films and multilayers will be treated.

- In the first chapter the main properties of transition metal oxides will be discussed, and in particular, the general characteristics of $La_{0.7}Sr_{0.3}MnO_3$ and $Pr_{1-x}Ca_xMnO_3$ compounds will be described.
- In the second chapter a description of thin films properties is given. The deposition technique will be also described.
- The effect of strain on the structural and magnetic properties of epitaxial $La_{0.7}Sr_{0.3}MnO_3$ and $Pr_{1-x}Ca_xMnO_3$ with x = 0.3, 0.5 thin films grown on $SrTiO_3$ substrate with the two different (001) and (110) orientations will be discussed in the 3rd chapter.
- In the 4th chapter the effect of strain on epitaxial manganites multilayers will be presented and discussed.

CHAPTER 1

Colossal magnetoresistive manganites.

In 1950 Jonker and Van Santen [1] reported about the first crystallization and magnetic characterization of the mixed-valence "manganites", belonging to the pseudo-binary systems $LaMnO_3$-$CaMnO_3$, $LaMnO_3$-$SrMnO_3$, $LaMnO_3$-$BaMnO_3$ and $LaMnO_3$-$CdMnO_3$. They used the name "manganite" to indicate all compositions containing both trivalent and tetravalent manganese, although, as they themselves stressed out, the term would be better reserved to phases of tetravalent Mn only.

All manganites, treated in this thesis, crystallize in the perovskite structure whose atomic arrangements was first described in the 1830s by the geologist Gustav Rose, who named it after the famous Russian mineralogist, Count Lev Alekseevich Perovskii.

The manganites present a rich variety of magnetic states strongly coupled with transport properties and structure. In particular for these materials the role of structure and in particular of the distortion of the MnO_6 octahedra is of great importance for the magnetic and transport properties. Anyway, the coupling of structure and physical properties of manganites is not completely understood. Several works have been addressed to the exploration of this coupling [2, 3, 4], but more must be done to understand it. The control of the magnetic and transport properties is fundamental for the application of manganites in devices. Besides, the perovskite manganese oxides exhibiting a metal-insulator (MI) transition accompanied by magnetoresistive effects soon raised the interest of the scientific community because of their potential technological applications.

In this chapter, I report on the structural, transport and magnetic properties of manganite compounds with particular regards to $La_{0.7}Sr_{0.3}MnO_3$ and $Pr_{1-x}Ca_xMnO_3$ compounds.

1.1. The perovskite structure.

The term perovskite was first used for $CaTiO_3$, in honour of its discoverer Perovskii. The ideal perovskite structure (formula ABO_3), that crystallizes in cubic symmetry with space group $Pm\bar{3}m$ and lattice parameter $a \approx 4$ Å (figure 1.1), consists of a three-dimensional framework of corner-sharing BO_6 octahedra in which the A cations reside in the dodecahedral sites surrounded by twelve oxygen anions. The described structure is centrosymmetric. Only very few perovskites have this simple cubic structure at room temperature, but many of them acquire this ideal structure at higher temperatures.

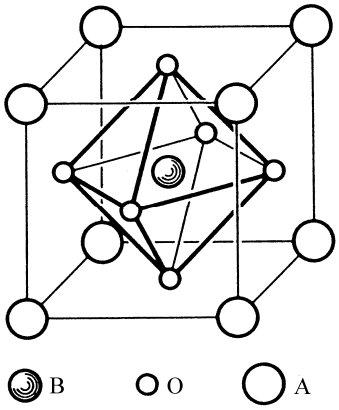

Figure 1.1. Simple cubic perovskite ABO_3.

To rationalize the tendency towards distortions, Goldschmidt introduced the so called *tolerance factor t* defined, as follows, in term of the ionic radii of the atomic species of the structure [5]:

$$t = \frac{R_A + R_O}{\sqrt{2}(R_B + R_O)},$$

with R_A, R_O and R_B being the ionic radii for the A ion, oxygen and B ion respectively. For the ideal cubic closest packing of atoms results $t = 1$. Goldschmidt himself underlined that the perovskite structure is stable only if the t parameter lies between 0.8 and 1. As t approaches unity, the cubic structure becomes more stable. A deviation of t value from 1 indicates the likely formation of a distorted perovskite structure. Every specific distortion is due to

a rotation (tilt) of the oxygen octahedra. Which structure is realized depends on both the magnitude and the relative rotation of the octahedra around the crystallographic axes.

By varying the A and B cations, and consequently their ionic radii, it is possible to obtain a lot of perovskite compounds with different structural and electronic properties.

Starting from the simple ABO_3 perovskite, new compounds are derived upon substitution in one or both of the two cation sites A or B, with a different specie. These complex perovskites have $A_{1-x}A'_xBO_3$ or $AB_{1-x}B'_xO_3$ formulas. The A' and B' are termed dopant species. The insert of a dopant specie modifies some properties depending on the doping fraction x.

The perovskite manganites have the general formula $AMnO_3$, but most interesting for the applicative research are the $A_{1-x}A'_xMnO_3$ complex perovskites that in the following will be indicate with $RE_{1-x}AE_xMnO_3$ formula, where RE stands for a trivalent rare earth element such as La, Pr, Nd, Sm, Eu, Gd, Ho, Tb, Y etc, and AE for a divalent alkaline earth ion such as Sr, Ca and Ba. The large sized RE trivalent ions and AE divalent ions occupy the perovskite A-site with 12-fold oxygen coordination. The smaller Mn ions in the mixed-valence state Mn^{3+}–Mn^{4+} are located in the B-site at the centre of an oxygen octahedron, with 6-fold coordination. For the stoichiometric oxide, the proportions of Mn ions in the valence states 3+ and 4+ are respectively, $1 - x$ and x.

Generally in the manganites the tolerance factor is appreciably different from unit [6], leading to rhombohedral or orthorhombic structures of lower symmetry than the cubic one, as showed in table 1 for some of the most studied manganites. As r_A or equivalently t decreases, the lattice structure transforms to the rhombohedral ($0.93 < t < 1$) and then to the orthorhombic structure ($f < 0.93$), in which the B–O–B bond angle (θ) is bent and deviates from 180^o.

It is noteworthy that at the microscopic level, one of the possible origins of the lattice distortion is the deformation of the MnO_6 octahedron arising from the Jahn–Teller (JT) effect (see par. 1.3). Another lattice deformation comes from the connecting pattern of the MnO_6 octahedra in the perovskite structure, forming a rhombohedral or orthorhombic lattice, as shown in figure 1.2. In these distorted perovskites, the MnO_6 octahedra show alternating buckling.

Composition	Structure	*t*
$La_{0.7}Ba_{0.3}MnO_3$	R	0.953
$La_{0.7}Sr_{0.3}MnO_3$	R	0.936
$Gd_{0.7}Ba_{0.3}MnO_3$	O	0.926
$Pr_{0.7}Sr_{0.3}MnO_3$	O	0.926
$La_{0.7}Ca_{0.3}MnO_3$	O	0.922
$Pr_{0.7}Ca_{0.3}MnO_3$	O	0.912
$Gd_{0.7}Sr_{0.3}MnO_3$	O	0.908

Table 1.1. Structural characteristic of $RE_{0.7}AE_{0.3}MnO_3$ manganites (RE = La, Gd, Pr and AE = Ba, Ca, Sr). R = rhombohedral and O =orthorhombic.

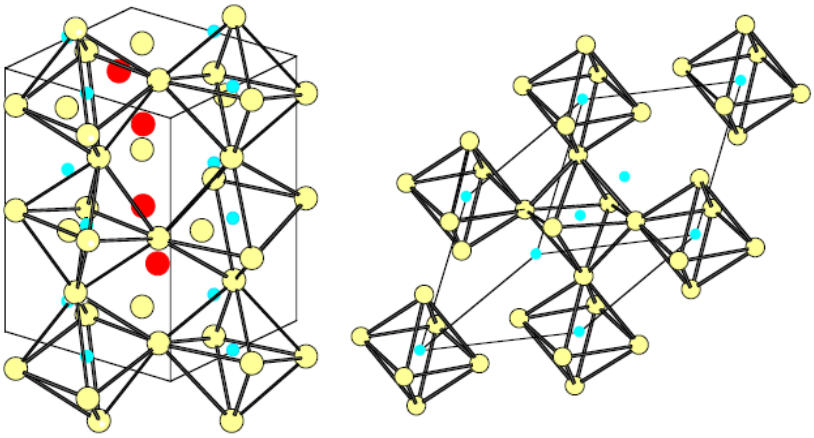

Figure 1.2. Structures of distorted perovskites of manganite: orthorhombic (left) and rhombohedral (right). After reference [7].

1.2. Electronic configuration.

For an isolated Mn atom (Z = 25, electronic configuration $3d^5 4s^2$), the five-fold degenerate 3*d* levels are occupied singly with electrons of parallel spin, according to the first Hund's rule.

If the Mn atom is not isolated, but it is instead in the center of the MnO_6 octahedra, the effect of the octahedral crystal field, due to the p orbitals of the six neighbouring oxygens, is to partially lift the orbital degeneracy, generating a triplet of lower-energy states called t_{2g} (d_{xy}, d_{xz}, d_{yz}) and a doublet higher-energy states called e_g ($d_{x^2-y^2}$, d_{z^2}), with a separation $\Delta \sim 1.5$ eV [8], as showed in figure 1.3.

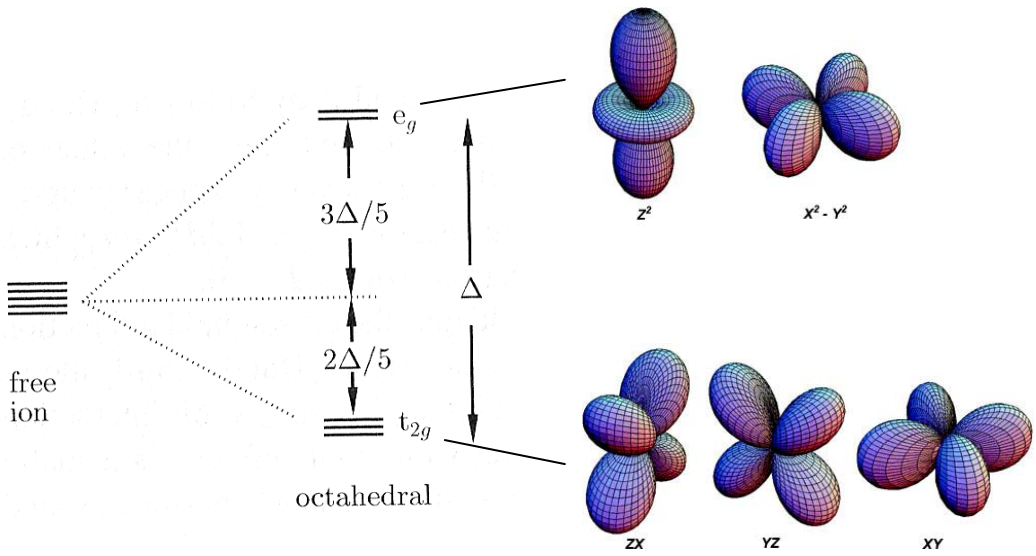

Figure 1.3. Effect of the octahedral crystal field on *d* states of a transition metal atom.

The nominal electronic configurations of Mn^{3+} ion is $3d^4$ and it contains four *d* electrons. On the basis of the Hund rule, it turns out that the configuration with three electrons in the t_{2g} level aligned in the same direction is the most favourable. The electrons aligned in the t_{2g} level form a "core spin" with total spin $S = 3/2$. The t_{2g} states form a half filled band and therefore do not contribute to the conductivity. The last *d* electron (e_g electron) is well separated in energy and aligned to the core spin via strong Hund coupling [9] (see fig. 1.4). It forms a loosely bound state. This e_g electron plays a key role in conducting and other properties of manganites (see below) as well as in determining its magnetic order.

As already pointed out, the main effect of the doping in manganites is the change in manganese-ion valence. The Mn ion loses its e_g electron leading to

the change of valence: $Mn^{3+} \rightarrow Mn^{4+}$ ($3d^3$ electronic configuration). The missing electron can also be described as the creation of a hole (see fig. 1.4).

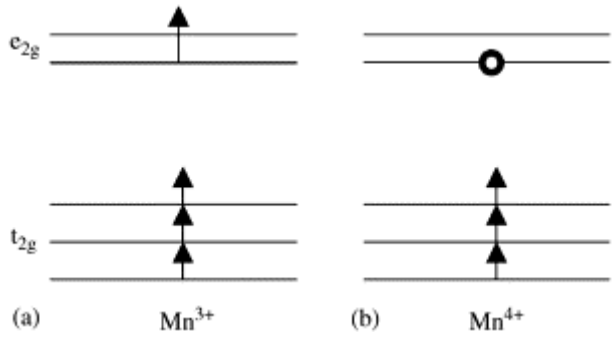

Figure 1.4. (a) d-shell of the Mn^{3+}; e_g degenerate level is splitted for clarity; (b) Mn^{4+} ion; o-hole. After reference [10].

1.3. The manganites and the Jahn-Teller effect.

In the manganites the presence of the Mn^{+3} produces the Jahn-Teller (JT) effect [11], that affects the crystalline structure and the physical properties of the materials.

As already mentioned, the Mn^{3+} electronic configuration is $t^3_{2g}\, e^1_g$, that is characterized by the presence of a single electron in the two-fold degenerate e_g level. As such, Mn^{3+} is a Jahn-Teller active chemical specie. According to the Jahn-Teller theorem, the $Mn^{3+}O_6$ groups in $RE_{1-x}AE_xMnO_3$ are energetically unstable towards distortions aiming to reduce the total energy of the system, as a consequence of a lifting of degeneracy of the e_g levels. The degree of distortion is determined by the competition between the gain in energy due to the e_g splitting and the increase of the elastic energy associated to the lattice distortion itself.

Supposing that the octahedra distorts elongating, for example, along *z*-axis. The crystalline field has no more a cubic symmetry around the Mn ion, and the energies of the $d_{x^2-y^2}$ and d_{xy} orbital increase, because they result closer to the *p* oxygen orbitals. On the contrary, the energy of the d_{z^2}, d_{xz}, and d_{yz} orbitals decreases, because they are further from the *p* oxygen orbitals as showed in figure 1.5. The distort system has a lower electronic energy, but a

higher elastic energy caused by the deformation. Therefore, the system tends to distort spontaneously if the gain in electronic energy is greater than the loss in elastic energy. This distortion is termed Jahn-Teller effect.

The Mn^{4+} ion is JT inactive, because of the absence of an unpaired electron in the e_g orbitals. The JT effect is local since regards the environment of a single Mn ion.

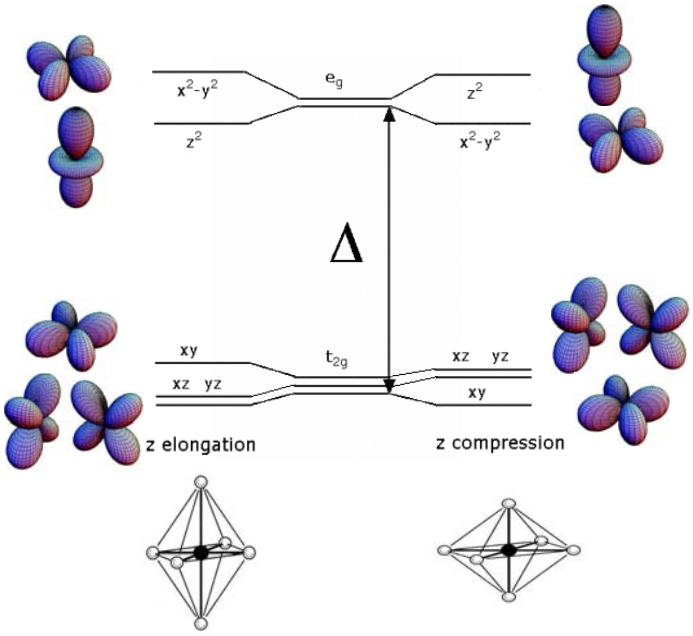

Figure 1.5. Jahn-Teller effect on d energy levels in the case of elongation (on the left) and of compression (on the right) along z direction of the $Mn^{3+}O_6$ octahedra.

When the phenomenon of JT distortion involves the octahedra cooperatively throughout the crystal, a distortion of the whole lattice occurs, the so called cooperative JT effect (figure 1.6).

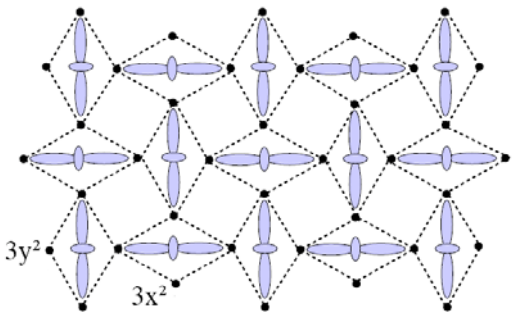

Figure 1.6. Cooperative JT distortions and resulting lattice.

Cooperative JT effect occurs in manganites when the concentration of Mn^{3+} ions is sufficiently high, i.e. at low doping level. The cooperative JT effect gives rise to a structural phase transition at a certain critical temperature T_{JT} [12], associated to an orbital ordering (OO), not present above T_{JT}. The effect of cooperative Jahn-Teller effects in manganites is to localize the e_g electrons on Mn^{3+} sites, and to stabilize insulating phases, either locally or at long range.

When Mn^{3+} is diluted into Mn^{4+} species by doping, the possibility of cooperative effects among JT active octahedra is reduced, and no static distortion will be observed.

In opposition to the cooperative JT effect, the effects that are observed for high dilutions are called dynamic JT effects. A dynamic effect involves rapid hopping of the distortion from site to site. This is important in manganites which contain a mixture of Mn^{3+} and Mn^{4+} ions with low Mn^{3+} content.

1.4. Orbital and charge ordering.

The orbital ordering consists in a spatially ordered arrangement of d orbitals in the crystal. Strongly associated with the carrier concentration, it develops when the d electron occupies an asymmetric orbital. The direct electrostatic repulsion of the charge clouds, coupled with cooperative JT distortions, stabilises the effect generating an ordered sublattice of orbitals. A scheme of OO can be found in figure 1.7.

The ratio Mn^{3+}/Mn^{4+} is responsible for the phenomenon of charge ordering (CO). This consists of a periodic distribution of electric charge (i.e. e_g electrons of Mn^{3+} ions in the crystal lattice), driven by Coulomb interaction. The mobile e_g electrons may become localised at certain Mn ion positions in the lattice, forming an ordered sublattice. In principle, however, these charges do not need to be necessarily localized on the Mn sites, and in fact they could sit on the bond centres as well, or, in the most general case, on some intermediate point between those two. Such an intermediate CO state can be more generally seen as a charge-density wave, lacking inversion symmetry and then potentially capable to develop ferroelectric ordering.

CO is mainly observed at special concentration of dopant, namely at rational fractions (as for example x = 1/8, 3/10, 1/2, 3/4). In this case the extra electron of Mn^{3+} are localised on alternate manganese ions, creating an ordered path of charge in the lattice (as shown in figure 1.7). The CO can be either long-ranged or short-ranged. It is clear that CO is competitive with the electron conductivity, because it tends to inhibit the movement of the charges through the crystal. Compounds with long-range CO are generally insulating, but localised CO (polarons) is responsible for an enhancement of resistivity, introducing scattering centers for the mobile electrons.

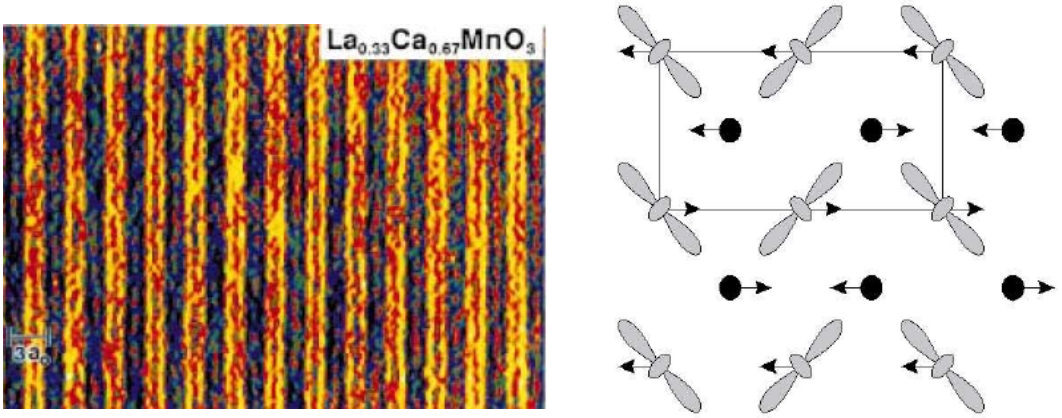

Figure 1.7. On the left, high-resolution lattice image showing pairing of CO $Mn^{3+}O_6$ stripes in $La_{0.33}Ca_{0.67}MnO_3$. After reference [13]. On the right, two-dimensional scheme of OO and CO. The dots represent the Mn^{4+} ions, while the Mn^{3+} are represented by the orbital d_{z^2}. The sublattice of orbitals is highlighted by the solid line. The possibility of spin order is also shown.

1.5. Exchange interaction in magnetism: direct exchange.

Exchange interactions lie at the heart of the phenomenon of long range magnetic order. Although the consequences of the exchange interaction are magnetic in nature, the cause is not; exchange interactions being due primarily to electrostatic interactions, arising because charges of the same sign cost energy when they are close together and save energy when they are apart. Indeed, in general, the direct magnetic interaction between a pair of electrons is negligibly small compared to this electric interaction.

If the electrons on nearest neighbour magnetic atoms interact via exchange interaction, this is know as direct exchange. The direct exchange is modelled by the Heisenberg exchange Hamiltonian:

$$H_{ex} = -\sum_{iJ} J_{iJ} S_i \cdot S_j$$

where J_{ij} is the exchange constant between the i^{th} and j^{th} spins, distributed on a regular lattice. Only nearest neighbours are usually included in the summation. The magnetic properties of the crystal depend on the sign and the strength of the interaction between spins: if $J_{ij} = J > 0$ the parallel orientation of the spins is favoured, giving a ferromagnetic state. If $J_{ij} = J < 0$, the magnetic order is antiferromagnetic, with the spins of nearest neighbours antiparallel.

However for the manganites, as for many other magnetic materials, it is necessary to consider some kind of indirect exchange interaction, because the Mn ions are alternated with O in the lattice.

1.6. Indirect exchange: superexchange.

Superexchange is an indirect exchange interaction between non-neighbouring magnetic ions, which is mediated by a non-magnetic ion, that is placed in between them. This interaction was first proposed by Kramers [14] in 1934 to the aim of finding an explanation for the magnetic properties observed in insulating transition metal oxides, in which the magnetic ions are so distant that a direct exchange interaction could not explain the presence of magnetically ordered states, so the longer-range interaction that is operating in this case should be "super". The problem was thereafter treated theoretically by Anderson [15], who in 1950 gave the first quantitative formulation showing that the superexchange favours antiferromagnetic order.

1.7. Double exchange model.

In some oxides, it is possible to have a ferromagnetic exchange interaction which occurs because the magnetic ion shows mixed valency. Examples of this include the doped manganites $RE_{1-x}AE_xMnO_3$, in which the Mn ion can be present in 3+ and 4+ oxidation states. The ferromagnetic coupling between

Mn^{3+} and Mn^{4+} ions, participating in electron transfer, is due to the double exchange mechanism, first introduced by Zener in 1951 [16], that can be understood with reference to figure 1.8. The e_g electron on a Mn^{3+} ion can hop to a neighbouring site only if there is a vacancy there of the same spin (since hopping proceeds without spin-flip of the hopping electron). If the neighbour is a Mn^{4+} ion that has not electrons in its e_g shell, this should present no problem. However there is a strong exchange interaction (first Hund rule) between the e_g electron and the three electrons in the t_{2g} level that want to keep them all aligned. This is not favourable for an e_g electron to hop to a neighbouring ion in which the t_{2g} spins will be antiparallel to the e_g electron. Ferromagnetic alignment of neighbouring ions is therefore required to maintain the high spin arrangement on both the donating and receiving ion.

Because the ability to hop gives a kinetic energy saving, allowing the hopping process reduces the overall energy. Thus, the ions align ferromagnetically to save energy. Moreover, the ferromagnetic alignment allows the e_g electrons to hop through the crystal and the material became metallic.

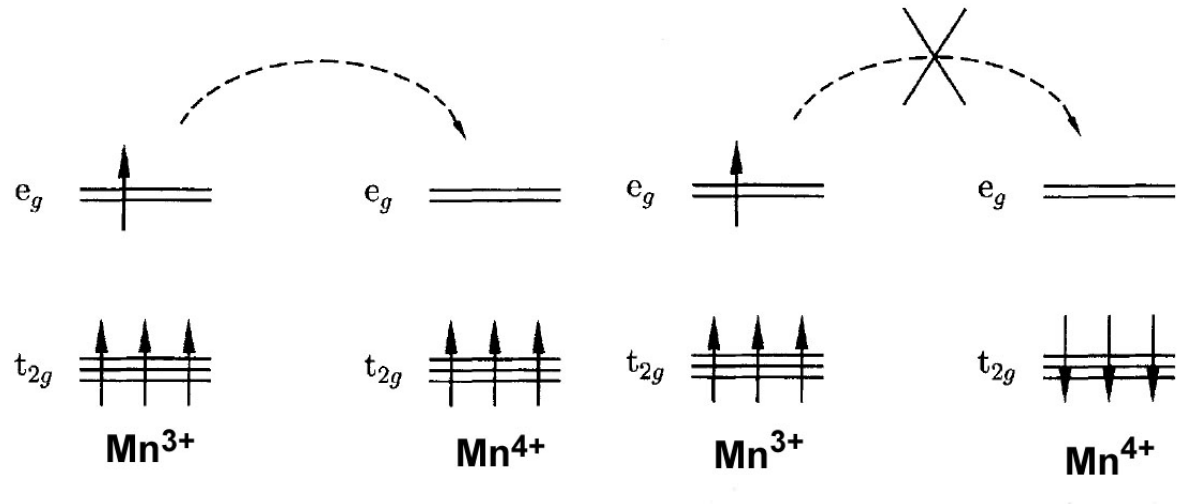

Figure 1.8. The double exchange interaction favours hopping if (a) neighbouring ions are ferromagnetically aligned, and not if (b) neighbouring ions are antiferromagnetically aligned.

It has been shown [17], that the electron transfer integral t between Mn ions in the double exchange process depends on the angle θ between their two core spins: $t = t_o \cos(\theta/2)$.

1.8. Electron-phonon coupling.

As pointed out by Millis [18], the magnetic degree of freedom is not the only one to be taken into account for the complete explanation of the transport properties in manganites. The picture of strong interactions between electronic configuration and structural symmetry (e.g. JT distortions) fits well the idea of Millis, which is that a perturbation of the crystal symmetry (buckling of O-Mn-O bond or rigid rotation of MnO_6 octahedra) might favour an overlap of orbitals. This can be responsible of a change in the hopping amplitude and consequently in the conductivity. The idea of Millis is that the one-electron approach used in the double exchange theory does not account for most of the properties of manganites, and for a more complete description of the physics of the manganites, the structural degree of freedom must be taken into account in the form of electron-lattice interaction.

The strong electron-phonon coupling, relative to the distortion of MnO_6 octahedra in the JT effect, may localise carriers, because the presence of an electron in a given Mn orbital causes local distortion, which produces a potential minimum: this minimum tends to trap the electron in that orbital. If the coupling is strong enough, these tendencies lead to the formation of a "self-trapped" state called polaron [19]. This short range charge order, which disappears in the FM phase, is believed to be responsible for the insulating properties of the paramagnetic phase.

1.10. Colossal magnetoresistance.

The colossal magnetoresistance (CMR) effect consists in a drastic reduction of the resistivity of a material and in a shift of the resistivity curves versus higher temperature in presence of an external magnetic field. The effect, observed in the manganese perovskites, was called "colossal" magnetoresistance to

distinguish it from the giant magnetoresistance observed in magnetic multilayers.

In doped manganites $RE_{1-x}AE_xMnO_3$ the origin of the CMR is connected with the presence of a metal-insulator transition. The CMR effect is observed in manganites of a narrow range of composition between x = 0.3 and 0.4, where the coexistence of two micrometric magnetic phases in the absence of the magnetic field exists: a ferromagnetic insulating phase and an antiferromagnetic insulating one are observed. In the presence of a magnetic field, these phases transform into a ferromagnetic metallic phase at a Curie temperature T_C. The maximum effect of the CMR appears near the T_C. The magnetoresistance is usually defined as:

$$\frac{\Delta R}{R} = \frac{R(H) - R(0)}{R(0)}$$

where R(H) and R(0) represent the resistance in presence and in absence of the external magnetic field, respectively.

Resistivity measurements versus temperature and applied magnetic field for the CMR $La_{0.67}Ca_{0.33}MnO_3$ single crystals are shown in figure 1.9.

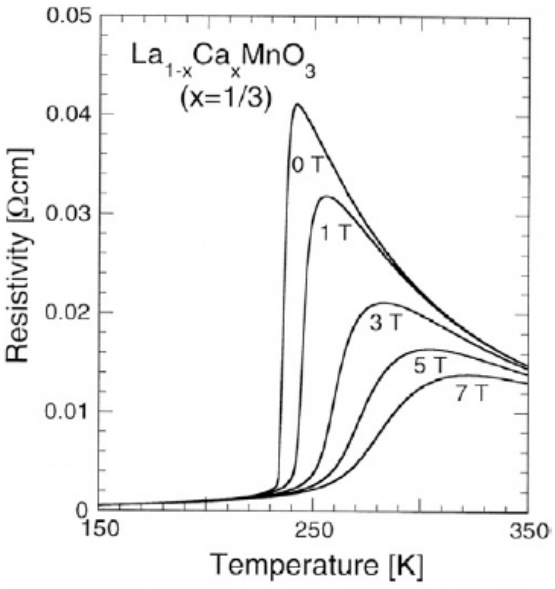

Figure 1.9. CMR behavior for the $La_{0.67}Ca_{0.33}MnO_3$ single crystal. After reference [7].

In manganites, the origin of the CMR is partly connected with the double-exchange phenomena. In a Mn^{3+} ion, the t_{2g} electrons are tightly bound to the ion but the e_g electron is itinerant. Because of the double exchange interaction, the hopping of e_g electrons between Mn sites is only permitted if the two Mn core spins are aligned. The magnetic field aligns the core spins and therefore increases the conductivity, especially near T_C.

The situation is actually more complicated because the carriers interact with phonons because of the Jahn-Teller effect. The strong electron-phonon coupling in these systems implies that the carriers are actually polarons above T_C. The transition to the magnetic state can be regarded as an unbinding of the trapped polarons [20].

Within the framework of the models proposed to explain the origin of CMR in manganites, I should mention the recently proposed percolation mechanism [21, 22, 23, 24]. This model is based on the idea that the colossal magnetoresistance is due to percolation between nanoscale ferromagnetic metallic (FMM) clusters in an antiferromagnetic insulating (AFI) matrix [24]. The detailed explanation of such theory is beyond the scope of this work, referring to the literature for more details.

1.10. $La_{1-x}Sr_xMnO_3$ compounds.

The undoped $LaMnO_3$ has an orthorhombic Pbnm crystal structure at room temperature, characterized by the presence of orbital ordering due to a cooperative JT effect. The compound undergoes a structural phase transition at 780 K, above which the OO disappears [25]. An AFI state is stable below $T_{Néel}$ = 140 K.

Chemical doping through substitution of Sr^{2+} into La^{3+} sites, introduces holes in the compound that are accommodated in the e_g levels. In other terms, the doping changes the oxidation state of some of the Mn ions from Mn^{3+} to Mn^{4+}. Therefore, as described in paragraph 1.8, the carriers can hop through the bridging oxygen ions of the Mn^{3+}-O-Mn^{4+} bonds and the material eventually becomes ferromagnetic metallic.

In figure 1.10 the phase diagram of $La_{1-x}Sr_xMnO_3$, indicating the different magnetic phases, is shown.

At high temperatures, for all Sr doping levels, the $La_{1-x}Sr_xMnO_3$ system is in a paramagnetic state, denoted by *P* in the phase diagram. Doped phases undergo different transitions as a function of temperature. For low doping ($0 < x < 0.08$) the system retains insulating properties with AF ordering. The AF state is spin canted, phase that is hardly distinguished experimentally from a mixture of AF and FM phases.

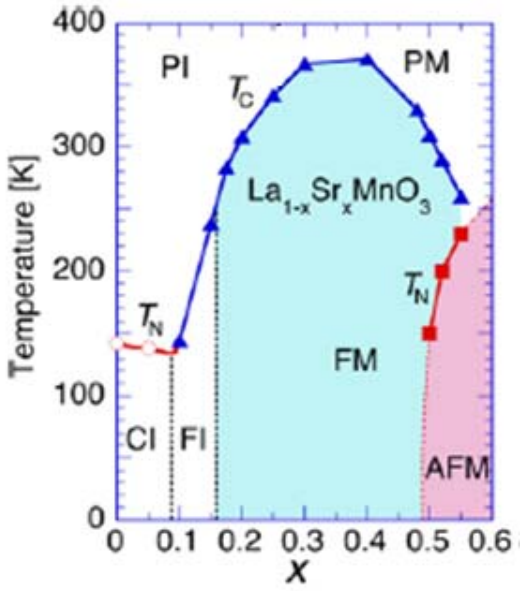

Figure 1.10. The phase diagram of $La_{1-x}Sr_xMnO_3$. After reference [7].

For $0.08 < x < 0.16$ the system is still insulator but ferromagnetic. Spin canting is still present. Jahn-Teller distortion is also present, confirmed by the structural transition from orthorhombic (typical for Jahn-Teller distortion) to rhombohedral symmetry.

In the $0.16 < x < 0.3$ range, a phase transition from ferromagnetic insulator to ferromagnetic metal as well as a structural transition occurs. There is no more Jahn-Teller effect as the number of Mn^{3+} Jahn-Teller active ions is too small to produce a cooperative effect. As a consequence a rhombohedral structure with six equals Mn-O distances is stabilized.

It is worth to note that for $x = 0.175$, a structural transition has been observed (the most important for this system) from the orthorhombic to the

rhombohedral structure as well as a transition from a PI to a FMM phase leading for this concentration to the colossal magnetoresistance at the highest level.

For x > 0.3 the system is ferromagnetic at room temperature, and following an ideal line from low temperature to higher temperature the system experiences a transition from low temperature ferromagnetic metallic phase to high temperature paramagnetic less metallic phase.

In fact, even if the system is still metallic for $T > T_C$, the transition from PM to FM phase is accompanied by a large jump in the resistivity, while maintaining an overall metallic temperature dependence (figure 1.11) [26].

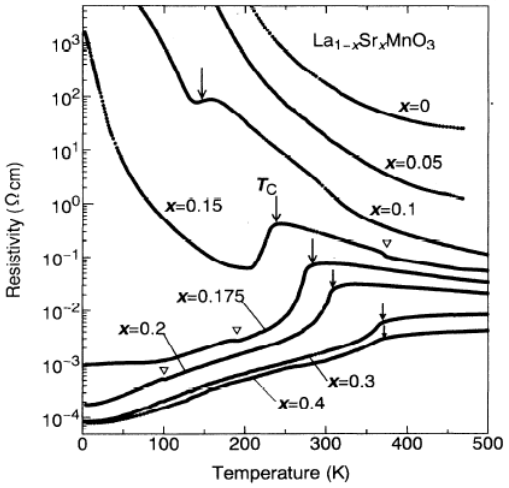

Figure 1.11. Temperature dependence of resistivity for $La_{1-x}Sr_xMnO_3$ crystals. Arrows indicate the T_C, while open triangles indicate anomalies due to structural transition. After reference [26].

The highest Curie temperature for $La_{1-x}Sr_xMnO_3$ is for x = 0.3 ($T_C \approx 380$ K) and this is the reason why this composition is the most relevant for applications.

The crystal structure at room temperature changes from orthorhombic (Pbnm, x < 0.175) to rhombohedral ($R\bar{3}c$, x ≥ 0.175) [26]. The change of the lattice parameters is shown versus x in figure 1.12. At room temperature $La_{0.7}Sr_{0.3}MnO_3$ has a rhombohedral structure with a_r = 5.477 Å and α_r = 60.38°, even if the pseudocubic approximation with $a_c = b_c = c_c$ = 3.873 Å is often adopted.

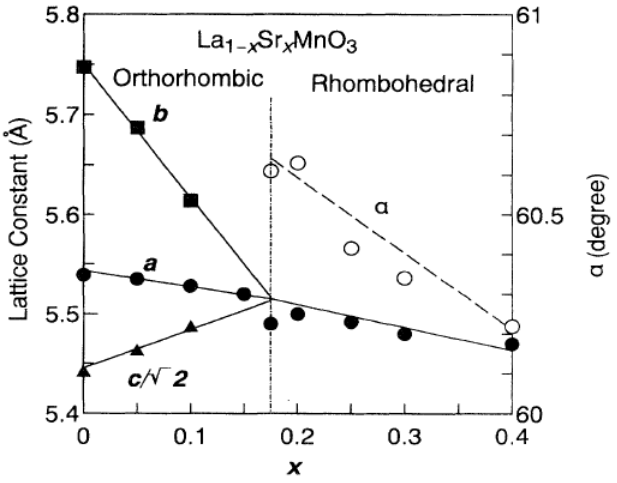

Figure 1.12. Lattice parameters for $La_{1-x}Sr_xMnO_3$ crystals at room temperature. After reference [26].

1.11. $Pr_{1-x}Ca_xMnO_3$ compounds.

The undoped $PrMnO_3$ exhibits an orthorhombic distorted structure (space group Pbnm) at room temperature, and a transition at T_N = 91 K to an antiferromagnetic order [27].

$Pr_{1-x}Ca_xMnO_3$ is obtained by chemical doping through substitution of Ca^{2+} into Pr^{3+} sites. Figure 1.13 shows the phase diagram of $Pr_{1-x}Ca_xMnO_3$ in function of the Ca content (x). $Pr_{1-x}Ca_xMnO_3$ is a unique example among manganites, exhibiting insulating behaviour over the entire chemical composition x and over the entire temperature range. This is a consequence of the small ionic radius of Ca, which results in a pronounced orthorhombic distortion (figure 1.14) that favours charge localization.

Antiferromagnetic insulating (AFI) phases are stable below 100 K for $0 \leq x \leq 0.1$ doping level, followed (for $0.15 \leq x \leq 0.3$) by a region of insulating ferromagnetic (FI) phases with $T_C \leq 140$ K. For $0.3 \leq x \leq 0.75$, at low temperature (≤ 240 K), $Pr_{1-x}Ca_xMnO_3$ (PCMO) shows a Jahn–Teller distortion that causes a charge ordered (CO) state at T_{CO} as described in paragraph 1.5. At lower temperature (≤ 175 K), *d* electrons of Mn ions show antiferromagnetic (AF) spin ordering, resulting in an AF insulator [28]. The magnetic state for $T_N < T < T_{CO}$ is paramagnetic. It has been reported that the CO state of AF insulating

PCMO collapses to a charge disordered state, which is observed as an insulator–metal transition, when an external stimulus such as a magnetic field [29, 30], light [31], x-rays [32], high pressure [33], and an electric field is applied.

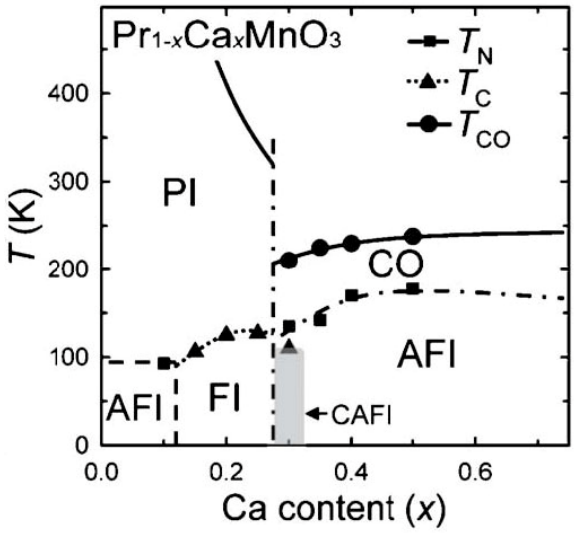

Figure 1.13. Phase diagram of $Pr_{1-x}Ca_xMnO_3$. After reference [35].

The canted AF insulating (CAFI) state also shows up below the AFI state in the COI phase $0.3 < x < 0.4$. A paramagnetic insulator (PI) phase is present at high temperatures.

Now I analyze in detail the compound $Pr_{0.7}Ca_{0.3}MnO_3$, that is a subject of this thesis. By x-ray and neutron diffraction Jirák *et al*. [28] have determined the structure of $Pr_{0.7}Ca_{0.3}MnO_3$ at room temperature, as orthorhombic (figure 1.14) with space group Pbnm (as for $0.1 \leq x \leq 0.5$), with lattice parameters a_o = 5.426 (2) Å, b_o = 5.478 (3) Å, c_o = 7.679 (4) Å.

As figure 1.13 shows, $Pr_{0.7}Ca_{0.3}MnO_3$ is between two different regions: one where the CO/AF phase is stabilized and the other where a transition from a PI state to a FMI one is observed at around 130 K. Several studies [28, 36, 37, 38] have evidenced the coexistence of both the two different magnetic phases (AFI and FI) in the narrow range of composition $0.3 \leq x \leq 0.4$ of bulk $Pr_{1-x}Ca_xMnO_3$, as, for example, showed in figure 1.15 for polycrystalline samples of $Pr_{0.67}Ca_{0.33}MnO_3$. When a magnetic field is applied a continuous transformation is induced of this phase separated compound. This

transformation occurs by the formation of mesoscopic ferromagnetic metallic (FMM) domains in the AFI phase and, eventually, in the FI phase, and subsequent growing and percolation of this conducting FM phase [39].

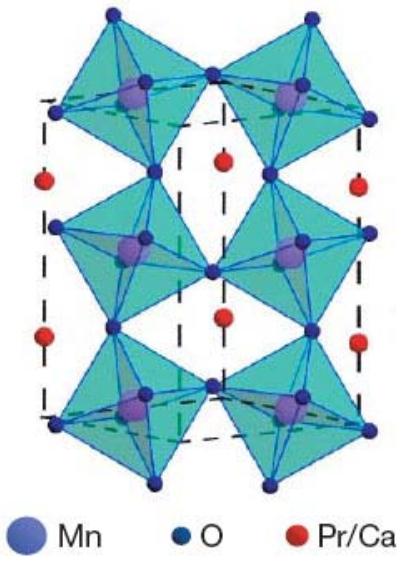

Figure 1.14. Orthorhombic unit cell of $Pr_{0.7}Ca_{0.3}MnO_3$. After reference [40].

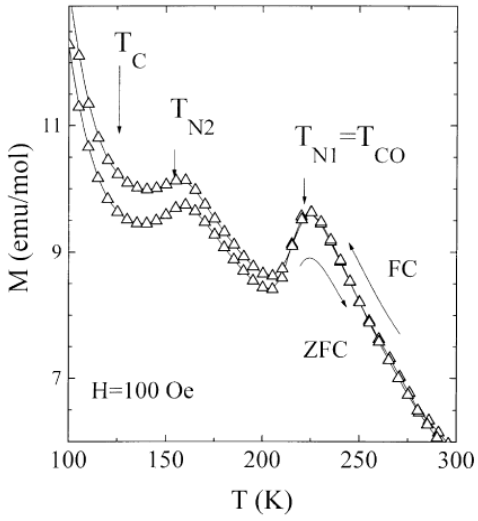

Figure 1.15. Magnetization (ZFC–FC) of polycrystalline samples of $Pr_{0.67}Ca_{0.33}MnO_3$. After reference [36].

The phase separation and the percolation process here described are considered to be essential to observe the CMR effect. In figure 1.16 the temperature dependence of resistivity for $Pr_{0.7}Ca_{0.3}MnO_3$ crystals under several magnetic fields is shown [30] (CMR effect).

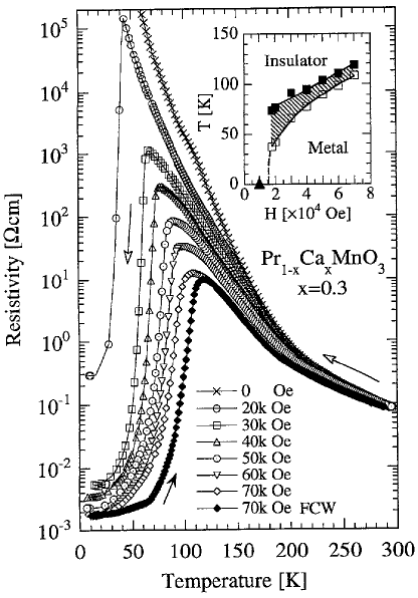

Figure 1.16. The temperature dependence of resistivity for $Pr_{0.7}Ca_{0.3}MnO_3$ crystals under several magnetic fields. Inset shows the phase diagram determined by resistivity measurements. The hatched area indicates the hysteretic region. After reference [30].

A second compound that I studied in this thesis is $Pr_{0.5}Ca_{0.5}MnO_3$, that is orthorhombic, but very close to cubic, with Pbnm space group and lattice parameters a_o = 5.3949(1) Å, b_o = 5.4042(2) Å, c_o = 7.6064(2) Å at room temperature [28, 41]. Thereby, the lattice constants are related to the simple cubic lattice parameter a_c as $a \sim b \sim c/\sqrt{2} \sim \sqrt{2}\, a_c \sim 5.4$ Å.

In $Pr_{0.5}Ca_{0.5}MnO_3$, the charge and orbital order develops in the paramagnetic phase below T_{co} = 250 K [41].

The ordering process is accomplished at T_N = 170 K [41] where the charge-exchange (CE) type antiferromagnetism sets in (figure 1.17) [42]. The ideal CE-type charge and orbital order implies a FM zigzag arrangement of the ordered $e_g(3x^2-r^2)$ and $e_g(3y^2-r^2)$ orbitals of Mn^{3+} ions in *ab* plane. The neighbouring zigzags are AF coupled; the ordering in the *c* direction is also AF.

By applying a magnetic field, the combined AF/CO state can go through a first-order phase transition (called the melting of the charge order) and transform to a FMM state. The melting fields are quite high, around 27 T at low temperatures [43].

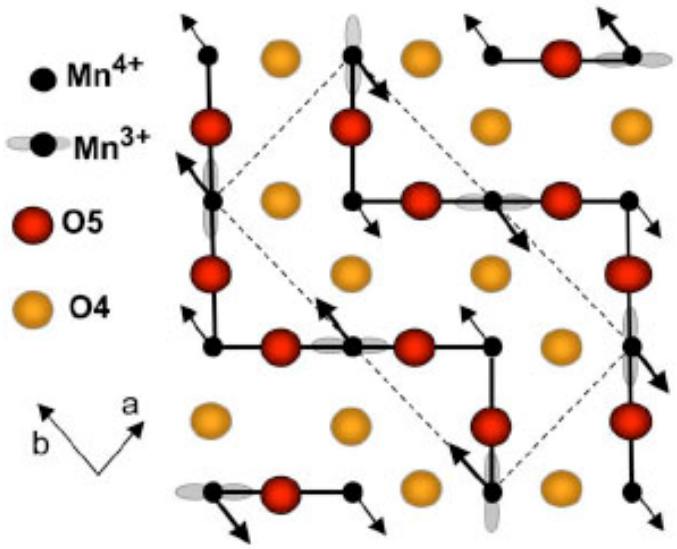

Figure 1.17. The CE-type magnetic structure in the site-centered CO/OO model. The ferromagnetic zigzags are indicated by the solid lines, and the dotted rectangle indicates the low temperature unit cell; only the *ab* plane is considered. The arrows show the Mn spins orientations. After reference [42].

CHAPTER 2

Manganite thin films.

The expertise reached in the growth of high T_C superconductor thin films with perovskite structure in the last fifteen years, using the technologies implemented for semiconductors (such as sputtering, Pulsed Laser Deposition - PLD, and Molecular Beam Epitaxy - MBE), has been successfully applied to the growth of high quality crystalline thin films of manganites [44, 45, 46].

The advantage of thin films consists in the possibility of studying crystals with high perfection and a controlled amount of grain boundaries or defects. However, the presence of a substrate introduces a new degree of freedom in the already rich landscape of variables, i.e. the external pressure in the form of biaxial stress.

This is why one of the major features of thin films is the strain, that induces changes of the physical properties (structure, transport and magnetic order) with respect to the bulk. These changes are the main interest of this PhD work.

Before discussing the effects of strain on manganite films, it is necessary to give a brief introduction to the basic idea of thin film growth and epitaxy. The growth technique, that was employed to fabricate the characterized films and multilayers, will be also described. A brief description of the principal effects of the strain on the structure and physical properties of $La_{0.7}Sr_{0.3}MnO_3$ and $Pr_{1-x}Ca_xMnO_3$ manganese perovskites, already studied, will be given.

2.1. Substrate choice and epitaxy of manganite films.

When a crystalline material is prepared as film form on a chosen monocrystalline substrate, the atoms can dispose in a way that produce a polycrystalline film or in a way that are in the same lattice positions of the substrate ones and also the orientation is identical to those of the substrate to produce an epitaxial film.

For a manganite, prepared as an epitaxial film, the crystallographic structure can differ from that of the parent distorted bulk, often assuming a

pseudo-cubic or a tetragonal structure. This is due to the biaxial stress determined by the substrate that results in a strained film structure. The stress affects many physical properties of the manganites, so that the choice of the substrate is of primary importance.

The basic requirements for the substrate can be summarized as follows: (a) it must be monocrystalline; (b) crystallographic lattice match with the Mn-compound; (c) similar thermal expansion coefficient; (d) absence of chemical interactions with the material to be deposited; (e) surface quality; (f) mechanical and chemical stability at the temperature and pressure conditions during the growth [47].

For compounds with cubic or pseudo-cubic but also orthorhombic crystal structures, oxide substrates with a square-planar surface orientation, such as the (001) face of a cubic oxide crystal (see figure 2.1), is ideal for oriented films. Table 2.1 lists most of the available oxide substrates that possess square-planar or near square-planar symmetry on one of its faces. Other cuts may be also considered, for instance (110) is another face often used to deposition (see figure 2.1). Typically, the in-plane lattice spacing of the oxide film should closely match that of the substrate or exhibit a reasonably close near-coincidence site lattice match, such as by rotating 45^{o} with respect to the principal axes.

The most common substrates for manganites films, which I also used in my work, are $SrTiO_3$, $LaAlO_3$, and $NdGaO_3$, which have perovskite structures with lattice parameters similar to the Mn-compounds, and that respond quite well to all the requirements listed above.

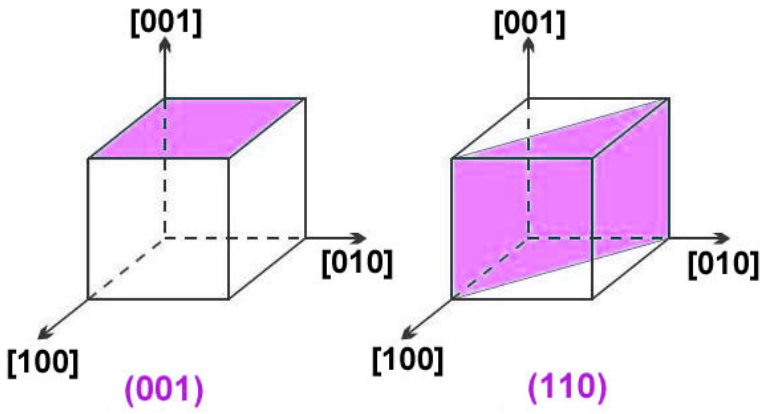

Figure 2.1. (001) and (110) planes of deposition in a cubic substrate.

Compound	Structure	a (Å)	b (Å)	c (Å)	α	Dielectric constant	Loss tangent	Thermal expansion coefficient ($\times 10^{-6}$/K)
$CaYAlO_4$	Tetragonal	3.645		11.874		20	4E−05	
$CaNdAlO_4$	Tetragonal	3.68		12.12		19	1E−4 (5 GHz)	12
$SrLaAlO_4$	Tetragonal	3.756		12.636		17	5E−4 (8 GHz)	12
$LaAlO_3$	Rhombohedral	3.788			90°4′	23	3E−5 (5 GHz)	11
$SrLaGaO_4$	Tetragonal	3.84		12.68		22	5E−05	10
$(LaSr)(AlTa)O_3$	Cubic	3.868				22	2E−4 (8.8 GHz)	10
$SrTiO_3$	Cubic	3.905				277	6E−2 (300 GHz)	10.4
$(LaSr)(GaNb)O_3$	Cubic	3.932						10
$KTaO_3$	Cubic	3.989				242	4E−4 (1.7 GHz)	6.8
MgO	Cubic	4.216				9.65	5E−4 (300 GHz)	10.5
TiO_2	Tetragonal	4.593		2.959		85, 190	2E−02	9.9 (c-axis), 7 (a-axis)
YSZ	Cubic	5.14				25	8E−3 (300 GHz)	8.80
$LiAlO_2$	Tetragonal	5.17		6.26				7.1 (a-axis), 15 (c-axis)
$YAlO_3$	Orthorhombic	5.176	5.307	7.355		16	1E−5 (10 GHz)	5
$NdAlO_3$	Rhombohedral	5.289			60°4′	17		
$LiGaO_2$	Orthorhombic	5.406	5.012	6.379		7 (a-axis), 6.5 (b-axis), 8.3 (c-axis)		11.8 (a-axis), 12.5 (b-axis), 3.7 (c-axis)
$NdGaO_3$	Orthorhombic	5.426	5.496	7.707		20	3E−4 (5 GHz)	8.00
$PrGaO_3$	Orthorhombic	5.465	5.495	7.729		24	3E−4 (1 kHz)	7.00
$LaGaO_3$	Orthorhombic	5.496	5.524	7.787		25	6E−3 (500 GHz)	10.30
YVO_4	Tetragonal	7.12		6.29		9.7	5E−5 (17 GHz)	4.4 (a-axis), 11.4 (c-axis)
$(NdSr)(AlNb)O_3$	Cubic	7.724						10
$MgAl_2O_4$	Cubic	8.083				12	5E−4 (1 MHz)	7.45
Mg_2TiO_4	Cubic	8.44				10	1E−03	12
Y_2O_3	Cubic	10.604				11.2		
$Y_3Al_5O_{12}$	Cubic	12.005				10	9E−04	7
$Gd_3Ga_5O_{12}$	Cubic	12.376				15	1.1E−3 (1 MHz)	

Table 2.1. Oxide substrates with square-planar surface symmetry.

Attractive substrate materials, for epitaxial films and multilayers, possess smooth surfaces with a unit cell high steps, as revealed by scanning force microscopy [48, 49]. Oxide materials for which surface termination and atomic steps have been reproducibly demonstrated are the perovskite-related materials [50], just $SrTiO_3$, $LaAlO_3$, and $NdGaO_3$.

Recent developments in understanding the surfaces of perovskites have enabled the reproducible termination of several perovskite crystalline surfaces with specific cation species [50, 51, 52, 53]. For example, a simple aqueous treatment, chemical etch, and annealing procedure yields (001) $SrTiO_3$ surfaces that are singularly TiO_2 terminated (see figure 2.2).

Figure 2.3 shows an atomic force microscopy (AFM) image of an atomically flat (001) $SrTiO_3$ surface that possesses a singular TiO_2 termination and the corresponding AFM line scan. This capability greatly enhances the ability to control phase nucleation and multilayer structure formation in oxide epitaxy.

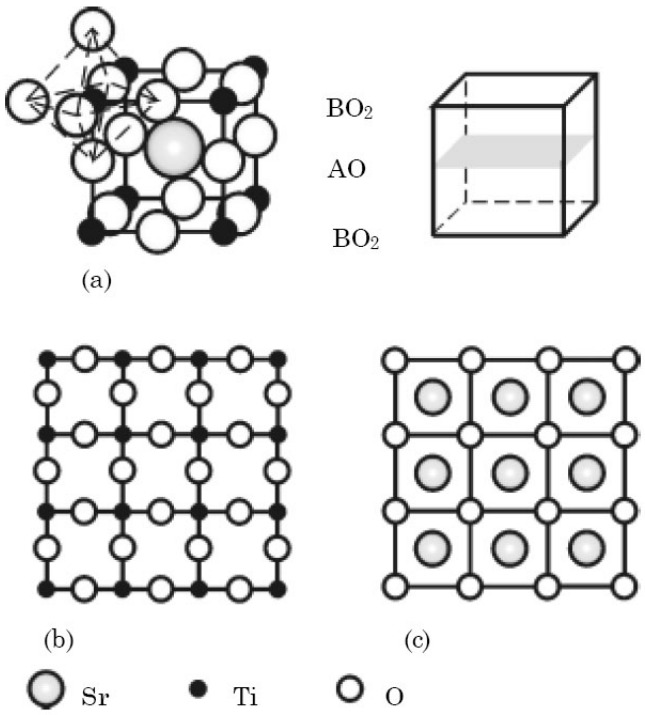

Figure 2.2. Schematic view of the $SrTiO_3$ unit cell with ABO_3 perovskite structure (a). The terminating plane can be either TiO_2, i.e. BO_2 (b) or SrO, i.e. AO (c). After reference [54].

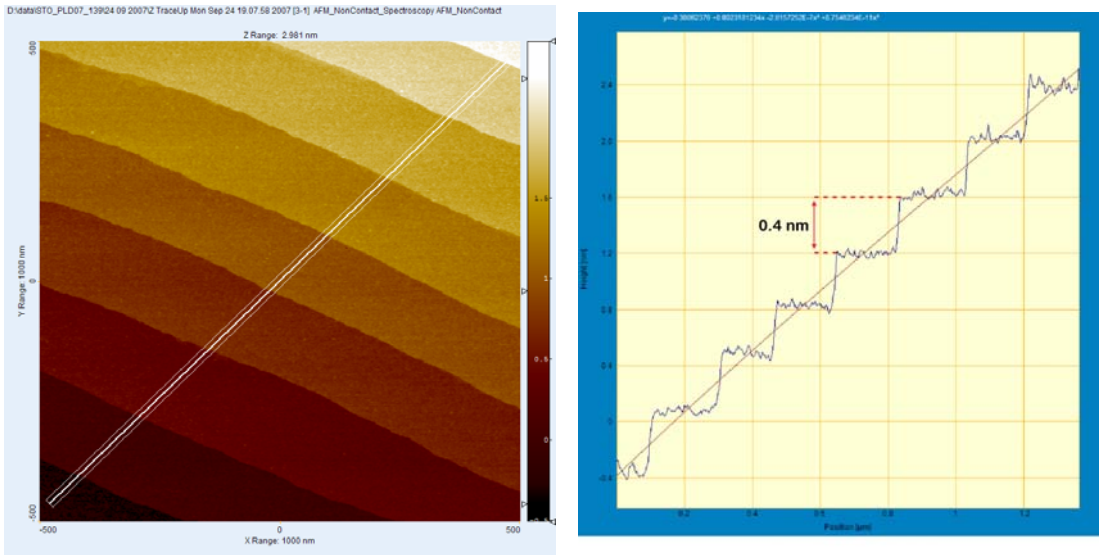

Figure 2.3. Atomic force microscopy image (on the left) and line scan analysis (on the right) of TiO_2-terminated $SrTiO_3$ (001) surface.

2.2. Strain effect in epitaxial films.

A film, that grows on a substrate with compatible crystal structure and slightly different lattice spacing, is under stress. The way in which a perovskite structure accommodates stress is mainly by using the internal degrees of freedom of the lattice, i.e. by rotation of MnO_6 octahedra, or small modifications of the Mn-O bond lengths, leading to JT distortions. Moreover, large variations of the unit cell lattice parameters are rather unusual, being energetically unfavourable. When a critical thickness is reached, the elastic energy stored in the structure is enough to create structural defects, or cracks. The critical thickness d_c is related to the mismatch:

$$\delta = \frac{a_{sub} - a_{film}}{a_{sub}},$$

where a_{sub} and a_{film} are the in plane lattice parameters of substrate and film, respectively. The higher is the mismatch, the smallest is the critical thickness.

In general the strain is elastic, and a deformation of the in plane lattice parameters produces an out of plane deformation of the cell, too. If $a_{sub} > a_{film}$, $\delta > 0$ implies in-plain tensile strain of the film, and the out of plane axis will be compressed. For $\delta < 0$ ($a_{sub} < a_{film}$), the strain is compressive and in plane lattice is compressed, while the out of plane axis will be expanded. Finally, if $a_{sub} \approx a_{film}$ no strain is applied (see figure 2.4).

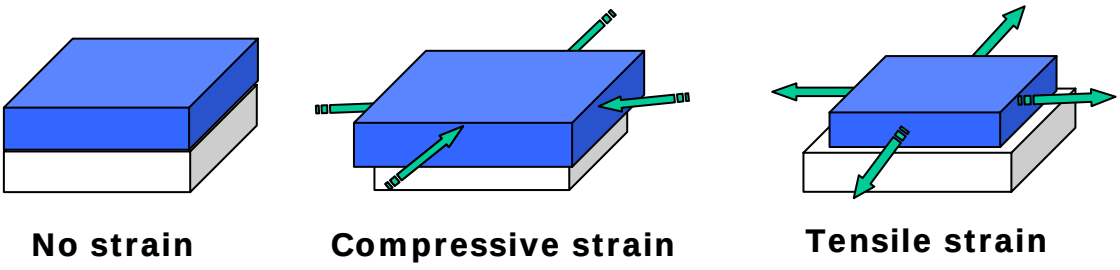

Figure 2.4. Schematic view of absent ($\delta = 0$), compressive ($\delta < 0$), and tensile ($\delta > 0$) strain.

In order to study the film deformations we can consider the stress-strain relations:

$$\sigma_{ij} = D_{ijkl} \cdot \varepsilon_{kl},$$

where σ_{ij} and ε_{kl} are the stress and strain tensor components, respectively, and D_{ijkl} are the stiffness components. The manganites are characterized by very small amplitude of lattice distortions out of cubic symmetry; in what follows, they are treated as cubic. In cubic symmetry the in plane and the out of plane strain components of the strain tensor are defined as follows:

$$\varepsilon_{||} = \frac{a_{||} - a_{bulk}}{a_{bulk}}, \qquad \varepsilon_{\perp} = \frac{c_{\perp} - c_{bulk}}{c_{bulk}},$$

where $a_{||}$ and $c_{\perp}$ are the in plane and out of plane lattice parameters of film, respectively. Since the substrate induces a biaxial strain symmetry in the growth plane, the three-dimensional strain states by symmetry can be decomposed into a bulk strain (hydrostatic term) ε_b and a biaxial strain (Jahn–Teller term) ε_{JT} [55]:

$$\varepsilon_b = \frac{1}{3}[2\varepsilon_{||} + \varepsilon_{\perp}], \qquad \varepsilon_{JT} = \frac{1}{2}[\varepsilon_{\perp} - \varepsilon_{||}].$$

In doped manganites the strain effect was demonstrated to be effective in modifying the electrical and the magnetic behavior of thin films [55, 56, 57, 58]. For example, Millis *et al.* [55] have developed a model to predict the dependence of strain on Curie temperature T_C for films with cubic symmetry:

$$T_C(\varepsilon_b, \varepsilon_{JT}) = T_C^0 [1 - \alpha \varepsilon_b - \beta \varepsilon_{JT}^2], \qquad \text{with } \alpha = \frac{1}{T_C^0}\frac{dT_C}{d\varepsilon_b}, \text{ and } \beta = \frac{1}{2T_C^0}\frac{dT_C}{d\varepsilon_{JT}},$$

where T_C^0 is the Curie temperature of the unstrained film. The bulk and the biaxial strain have opposite effects upon T_C. A hydrostatic compression will tend to increase the hopping and thereby reduce the electron-lattice coupling, inducing an increase in both the conduction band width and T_C. On the other hand, a biaxial strain increases the energy differences between the e_g levels imposed by the JT effect which reinforce the electrons tendency to become more localized decreasing T_C. Generally, a compressive strain induces an increase in T_C while a tensile strain a decrease in T_C. Therefore, the actual variation is dependent on the particular used substrate.

It is important to emphasize that a general determination of the structural properties of these compounds with respect to parameters such as strain and thickness is quite difficult. This is because of the extreme sensitivity

of the film properties to the details of growth process itself. A sensible comparative study among films versus a chosen parameter should be done only for films made in the same growth conditions of pressure, temperature, deposition rate, etc. The growth conditions need to be extremely well controlled for the production of high quality crystalline films.

2.3. $La_{0.7}Sr_{0.3}MnO_3$ films.

$La_{1-x}Sr_xMnO_3$ films are commonly grown by MBE and PLD techniques on numerous substrates (in particular, $LaAlO_3$ and $SrTiO_3$). Several interesting strain effects occur, which crucially depend on the lattice mismatch with the substrate.

The in plane compressive strain, enforced by the $La_{0.7}Sr_{0.3}MnO_3$ epitaxial growth on (001) oriented $LaAlO_3$, causes an out of plane tensile strain, a decrease of Curie temperature T_C, and a tendency to switch toward an orbital ordered antiferromagnetic phase [56, 59, 60, 61, 62, 63]. While, when the in plane applied strain is tensile, as, e.g., when the manganite is grown on (001) oriented $SrTiO_3$ or $BaTiO_3$, a compressive out of plane strain is induced, with a larger T_C than in case of in plane compression [56, 61, 62, 63, 64].

In general, $La_{1-x}Sr_xMnO_3$ films are reported to be very strain sensitive, with effects ranging from the formation of magnetic stripe domains [65] to inhomogeneities [66, 67], coexistence of different magnetic phases [60], anomalies in magnetostriction and thermal expansion [68, 69] and electric resistivity with a relevant dependence also from the film thickness [56, 60, 64, 65, 70].

It thus appears that an understanding of the coupling of magnetism and strain is an important requirement to design new devices.

2.4. $Pr_{1-x}Ca_xMnO_3$ films.

The structure of thick $Pr_{0.7}Ca_{0.3}MnO_3$ films deposited on $SrTiO_3$ (STO) (001) (thickness = 200 nm), where it is under tensile strain, was investigated by Fujimoto *et al*. [71]. The possibility of six growth modes of $Pr_{0.7}Ca_{0.3}MnO_3$

pseudo-cubic (p) perovskite on $SrTiO_3$ (001) substrate was discussed (see figure 2.5).

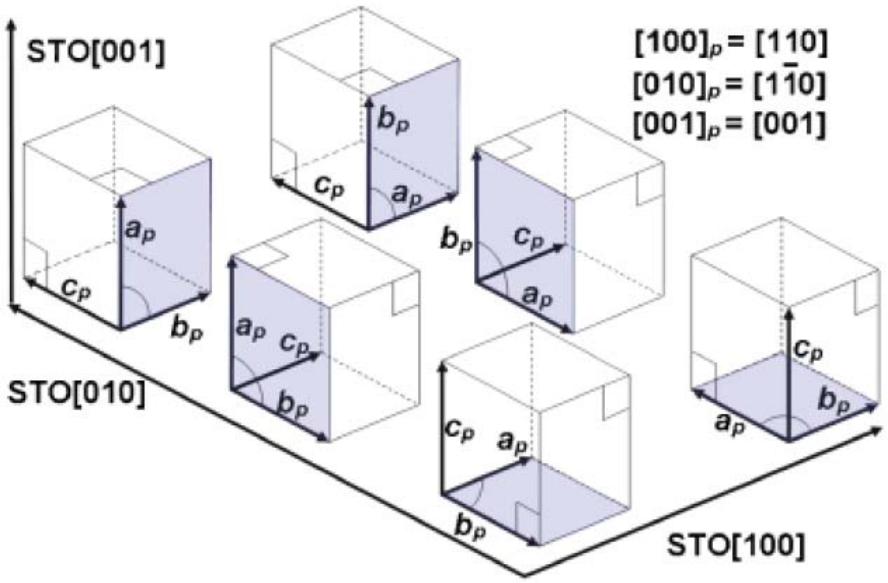

Figure 2.5. Schematic diagram showing six possible growth modes based on the pseudo-cubic unit cell of $Pr_{0.7}Ca_{0.3}MnO_3$ on the $SrTiO_3$ (001) substrate. The shadowed planes represent the $(001)_p$ of $Pr_{0.7}Ca_{0.3}MnO_3$ [71].

The structures of thick $Pr_{0.7}Ca_{0.3}MnO_3$ films deposited on $LaAlO_3$ (001) (thickness = 200 nm), where it is under compressive strain, and on $NdGaO_3$ (001) (thickness = 300 nm), where it is under slight tensile strain were investigated using transmission electron microscopy by MacLaren *et al*. [72].

The structures of $Pr_{0.5}Ca_{0.5}MnO_3$ films deposited on $LaAlO_3$ (001) (under compressive strain) and on STO (001) (under tensile strain) were investigated by Prellier *et al*. [73, 74].

The resistivity measurements of $Pr_{1-x}Ca_xMnO_3$ films with x = 0.2, 0.3, 0.4, and 0.5 show the insulating behavior in all temperature regions, and the resistivity itself monotonously decreases as x increases (see figure 2.6). However, no indication of the resistivity anomaly has been found associated with the onset of charge ordering irrespective of x. Therefore, the compressive strain suppresses the CO state in the $Pr_{0.7}Ca_{0.3}MnO_3$ films grown on $LaAlO_3$ (001) [75].

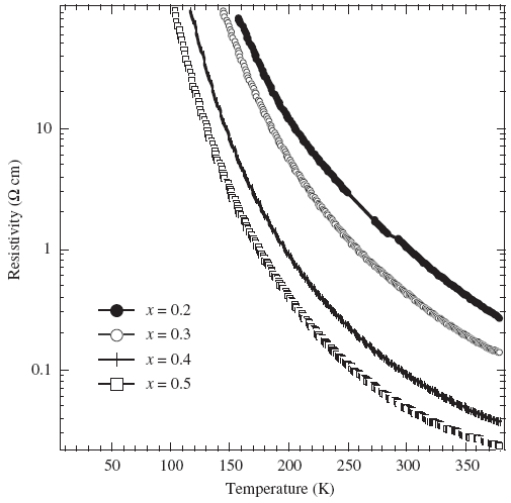

Figure 2.6. Temperature dependence of resistivity for $Pr_{1-x}Ca_xMnO_3$ (x = 0.2, 0.3, 0.4, 0.5) thin films 40 nm thick on $LaAlO_3$. After reference [75].

$Pr_{1-x}Ca_xMnO_3$ epitaxial *c*-axis-oriented thin films, in the $0.32 \leq x < 0.5$ doping range, grown on $SrTiO_3$ (001) substrate show the same type of phase separation and ordering than bulk materials [38].

In the $Pr_{0.5}Ca_{0.5}MnO_3$ films, the in plane compressive strain destabilizes the CO state [75, 76, 77], while the in plane tensile strain stabilizes the CO state [73, 74, 76, 77, 78, 79].

In particular, when $Pr_{0.5}Ca_{0.5}MnO_3$ thin films are grown on a substrate with smaller lattice parameters as $LaAlO_3$, the CO state is suppressed, owing to the lack of structural flexibility [75]. As a consequence, the CE–AF (see par. 1.11, figure 1.17) cannot be obtained. Instead of that, an insulating-ferromagnetic phase was found with a critical temperature of 240 K [80].

When $Pr_{0.5}Ca_{0.5}MnO_3$ thin films are grown on a substrate with a larger lattice constant such as $SrTiO_3$, the strain stabilizes the CO state and can significantly increase T_{CO}; for thin films (thickness less than 25 nm), values of T_{CO} above 320 K were reported [79], much higher than that of the bulk. Melting fields (cf. par. 1.11), however, are always lower (≥ 4 T [78, 81, 82]) than the bulk values, which was ascribed either to the effect of substrate clamping [81] or to the effects of disorder induced by strain relaxation [78]. The latter mechanism would explain both the thickness dependence of the melting behavior (with thicker films showing lower melting fields) and the effect of post

annealing, which relaxes strain, increases disorder, and lowers the melting fields.

It is noteworthy that, since 1990s, $Pr_{0.7}Ca_{0.3}MnO_3$ has become research subject because of a report of resistive switching in by Asamitsu *et al.* [34]. In the resistive switching phenomenon, a large change in resistance (> 1000 %) occurs on applying pulsed voltages, and the resistance can be set to a desired values by applying the appropriate voltage pulse. The materials, which show a resistive switching phenomenon as $Pr_{0.7}Ca_{0.3}MnO_3$, are the base for resistance random access memories (ReRAM). Recently, prototype ReRAM devices composed of $Pr_{0.7}Ca_{0.3}MnO_3$ and NiO have been demonstrated by Sharp Corporation and the University of Houston [83] and Samsung [84], respectively.

Moreover, the first symmetric, electrical pulse induced resistance change (EPIR), device has been fabricated, with $Pr_{0.7}Ca_{0.3}MnO_3$ active layer, which exhibits significant resistance switching under the application of electric pulses [85]. The symmetric EPIR device can be used in RRAM non-volatile memory applications.

2.5. Growth technique.

The ability to prepare films and understand their properties is of primary importance in the case of manganite, since most technological applications require high quality crystalline films and multilayers. The scientific community have profited of different deposition techniques developed during the last years for the synthesis of the first high-temperature perovskite-type superconducting oxide thin films. This resulted in the standardization of various methods, including sputtering, molecular beam epitaxy (MBE), metal–organic chemical vapour deposition (MOCVD), and pulsed laser deposition (PLD). Although this latter method has been used to make films since the 1960s, successful fabrication of $YBa_2Cu_3O_7$ (YBCO) epitaxial films, giving a good critical current, during late 1987 and early 1988, led to rapid development of this method [86, 87]. Since then, PLD has been extensively used to fabricate epitaxial films of superconducting, metallic, ferroelectric, ferromagnetic oxides and their multilayers.

The $La_{0.7}Sr_{0.3}MnO_3$, $Pr_{1-x}Ca_xMnO_3$ films and multilayers, characterized in this thesis, were fabricated using a pulsed laser deposition technique. In fact, all samples were deposited using RHEED-assisted laser ablation in the MODA (Modular facility for the Oxides Deposition and Analysis) complex system (figure 2.7 and 2.8) at the CNR-INFM Coherentia laboratory, that was designed for the study of surfaces and interfaces of oxide films.

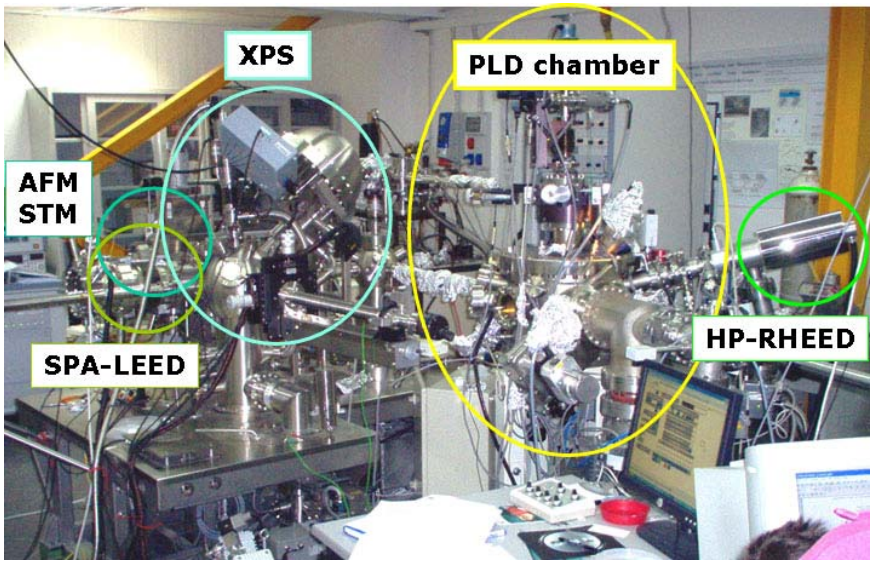

Figure 2.7. Photography of the MODA facility. The instruments are highlighted by labels.

The MODA deposition chamber (see figure 2.9) is equipped with an excimer laser (Coherent Compex 200, repetition rate 1 – 50 Hz, laser energy per pulse 100 – 600 mJ; pulse duration 10 ns, spectral width 1 pm), a multistage rotating carousel on which it is possible to mount up to six different targets, a heater capable to reach a temperature up to 1100 °C and a special High Pressure Reflection High Energy Electron Diffraction (HP-RHEED) set-up, allowing the in-situ growth monitoring also at high oxygen pressure.

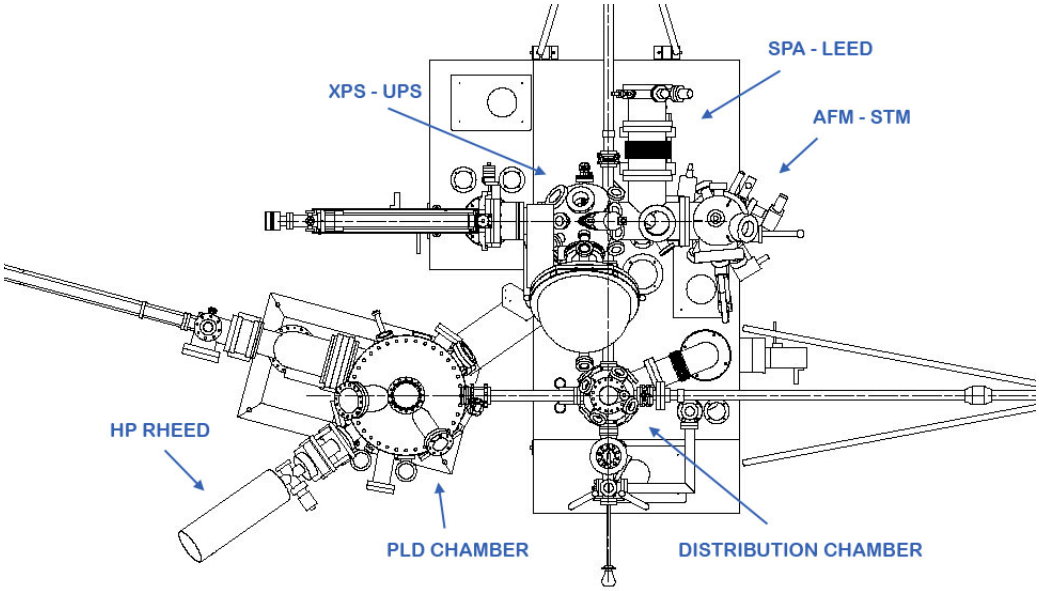

Figure 2.8. Schematic top view of the CNR-INFM Coherentia MODA system.

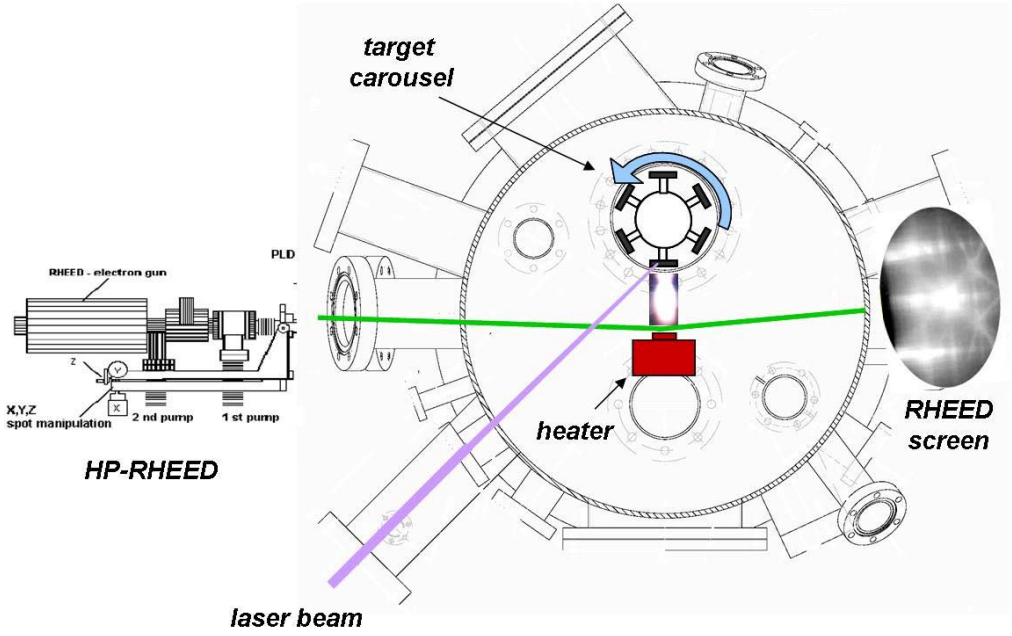

Figure 2.9. Top view of the deposition chamber and of the HP-RHEED of the MODA system.

The basic concept of the laser ablation is the following. A pulsed highly energetic laser beam, with a duration of tens of nanoseconds, hits a target of

the desired material. If the laser energy density is sufficient for ablation of the source target, the material (highly ionized and energetic particles) evaporates, perpendicular to the target surface, forming a gas plasma with a characteristic shape that is called *plume* (see figure 2.10). The plume condenses on a heated substrate placed in front of the target, forming a film on this substrate.

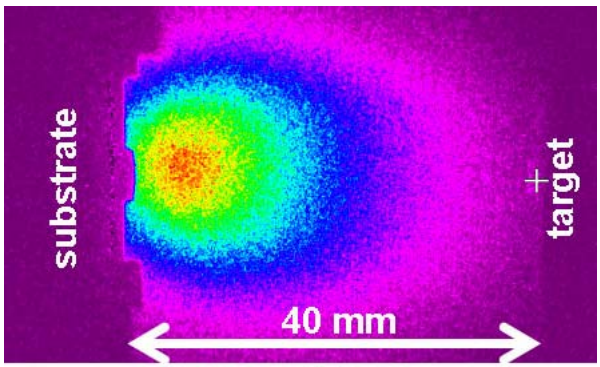

Figure 2.10. Plume expansion from the target to the substrate.

The physical quantities that are controlled are the fluence of the laser, the background oxygen pressure, the distance between target and substrate and the temperature of the substrate. Both the temperature of the substrate and the oxygen partial pressure influence the size and the shape of the plume, and consequently the deposition rate, while the choice of the energy and the frequency of the laser determine the energy of the atoms and ions that impact the substrate [88]. With such deposition technique it is possible the monitoring of the film growth during the deposition, achieving a high control of the film growth.

The HP-RHEED in-situ monitoring technique uses electron diffraction by surface atoms to provide information about the periodic rearrangement of the surface atoms. With a RHEED experimental set-up, two types of measurement can be performed: the analysis of the RHEED pattern spots intensity variation during the film growth, and the study of the RHEED pattern of a well defined surface, before and after a deposition. As example, in figure 2.11 on the left, the behaviour of the intensity of the specular spot (i.e., the (0,0) peak) recorded as a function of deposition time is showed. A single oscillation is

completed when a complete atomic layer is deposited. The intensity of the specular spot decreases by increasing the number of layers, an indication of a progressive roughening of the surface that it is common in the epitaxial growth. In figure 2.11 on the right, the typical RHEED pattern is shown; in the case of a single-domain crystalline surface, clean and atomically flat, the diffraction pattern results in sharp spots lying on concentric circles, called Laue circles. In presence of a three dimensional surface the RHEED diffraction pattern is a rectangular pattern of spots.

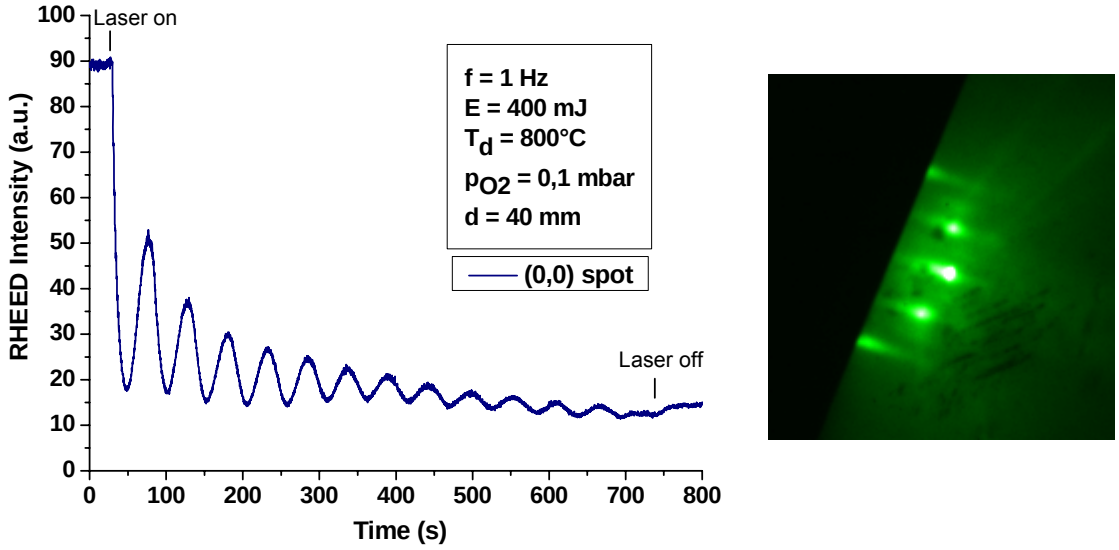

Figure 2.11. RHEED specular spot intensity measurements of $Pr_{0.7}Ca_{0.3}MnO_3$ film deposition on $SrTiO_3$ (001) (left) RHEED pattern of the deposited film (right).

Since the technological development of the oxide based devices results tightly dependent on the control of the film surfaces and the film-substrate interfaces, monitoring in-situ the film growth is fundamental to get optimal properties. In such structures, the control of the interfaces at the micro and nano-scale results of great relevance, in order to achieve the best performances. Of course, the higher degree of control has a cost in terms of easiness, because the RHEED-assisted laser ablation is far more complex than standard PLD.

CHAPTER 3

Chemical, structural and transport characterization of epitaxial films of $La_{0.7}Sr_{0.3}MnO_3$ and $Pr_{1-x}Ca_xMnO_3$.

In this chapter I will report and discuss on chemical, structural and magnetic characterization performed, by means of in-situ x-ray photoelectron spectroscopy (in MODA facility), and ex-situ high resolution x-ray diffraction, high resolution transmission electron microscopy and SQUID magnetometry, on $La_{0.7}Sr_{0.3}MnO_3$ films and $Pr_{1-x}Ca_xMnO_3$ (x = 0.3, 0.5) thin films deposited onto $SrTiO_3$ single crystal substrates. The discussion will focus on the effects of the strain on the manganites magnetic behaviour.

The films have been deposited in the MODA system using the RHEED-assisted laser ablation technique (as described in paragraph 2.3), at the CNR-INFM Coherentia laboratory in Naples.

The x-ray photoelectron spectroscopy (XPS) measurements have been performed on an Omicron photoelectron spectrometer equipped with a hemispheric analyzer Omicron EA 2000 - 125 (on the MODA system), using a Mg-Kα ($h\nu$ = 1253.6 eV) x-ray source running at 18 mA and 15 kV. The residual pressure in the spectrometer during data acquisition was always lower than 10^{-10} mbar.

High resolution x-ray diffraction and x-ray reflectivity measurements have been performed by means a 4-circles Bruker D8-Discover diffractometer (Cu anode), at the laboratories of the physics department of the University of Cagliari. The diffractometer is equipped with a Göbel mirror for parallel beam geometry and pure Kα selection and with a 2-bounces (V-Groove) monochromator (Ge 022) for $K\alpha_2$ elimination, therefore using CuKα1 (λ = 1.5406 Å) radiation with high resolution configuration. A working voltage of 40 kV and a filament current of 40 mA were employed.

The high resolution transmission electron microscopy (HREM) analysis has been performed by a Jeol 2100F electron microscope, operating at 200 kV and equipped with a field emission electron source, by Dr. A. Falqui of the Italian Institute of Technology in Genova.

Magnetic measurement have been performed using a Quantum Design MPMS5 XL5 SQUID magnetometer, equipped with a superconducting magnet producing fields up to 50 kOe, and calibrated using a Pd standard; the sensitivity for the magnetic moment being 10^{-8} emu.

3.1. Characterization of $La_{0.7}Sr_{0.3}MnO_3$ films grown on $SrTiO_3$ (001).

3.1.1. Chemical characterization.

The chemical characterization of the $La_{0.7}Sr_{0.3}MnO_3$ films grown on $SrTiO_3$ (001) has been carried out using the x-ray photoelectron spectroscopy (XPS).

The XPS measurements were performed using a pass energy for the electron analyzer of 50 eV for the survey spectrum acquisition and 40 eV for detailed spectra. To compensate for sample charging during analysis, all the binding energies were referred to the carbon *1s* signal at 285.0 eV. Spectral analysis included a Shirley background subtraction and peak fitting using mixed Gaussian-Lorentzian functions in a least-squares curve-fitting program [89] to calculate the integrated intensities (peak areas), as input data for stoichiometry calculation. From positions of the component peaks, detected in each photoelectron line, it has been possible to determine the chemical state of each species.

Quantitative analysis, that I have carried out, was done under the assumption of homogeneous sample, and has permitted to calculate the correct stoichiometry of the samples. The measurements were performed at three photoelectron take-off angles (30^o, 60^o, 90^o respect to the sample surface) with the aim to characterize the surface termination of the sample.

Elemental identification of the sample surface was performed, using the information from the survey spectrum. An example is given in figure 3.1, which shows the survey spectra, collected with a photoelectron take-off angle of 90°, from a $La_{0.7}Sr_{0.3}MnO_3$ film, with thickness t ≈ 10 nm, deposited on $SrTiO_3$ (001) substrate. The following elements with intense peaks were detected: La, Sr, Mn, O, only traces of impurities were present.

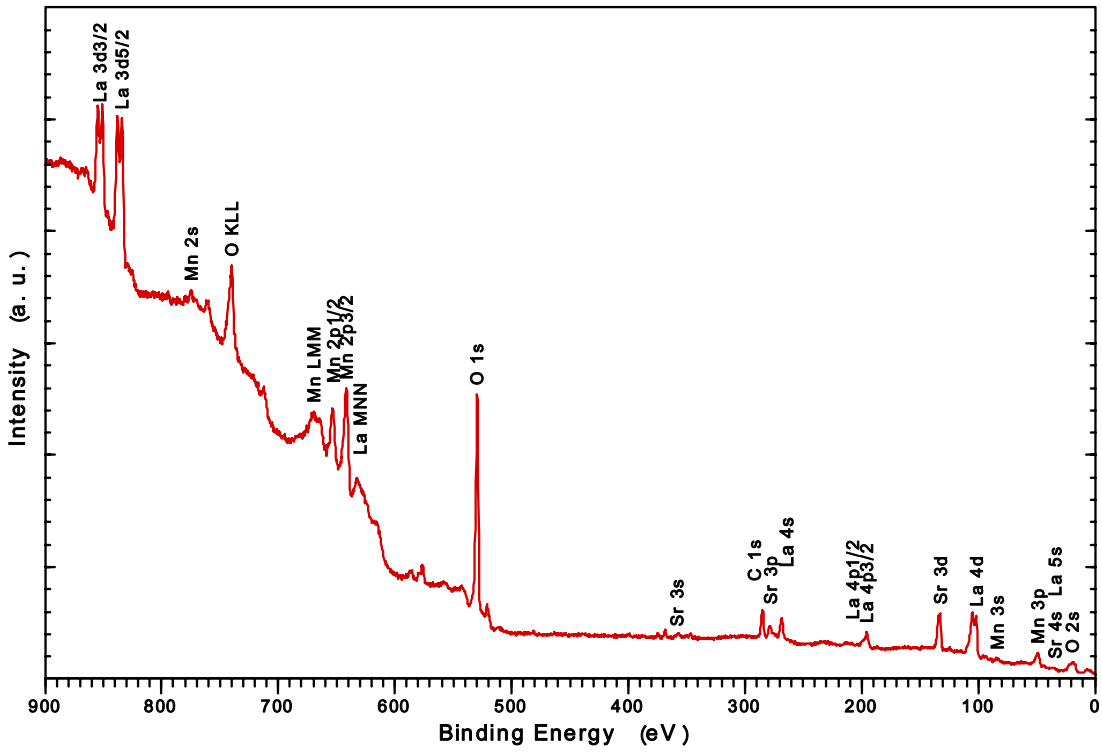

Figure 3.1. XPS survey spectra (Mg-Kα, 50 eV pass energy, 90° photoelectron take-off angle) from $La_{0.7}Sr_{0.3}MnO_3$ film grown on $SrTiO_3$ (001).

The La*4d*, Sr*3d*, Mn*2p*, and O*1s* high-resolution spectra, after the satellite subtraction and fitting, are displayed in figure 3.2.

The La*4d* XPS spectrum consists of a $4d_{5/2}$-$4d_{3/2}$ doublet with a spin–orbit splitting of 2.9 eV and. The binding energy at 102.0 ± 0.2 of the La$4d_{5/2}$ demonstrates that the oxidation state of La in $La_{0.7}Sr_{0.3}MnO_3$ film is 3+. Lanthanum has no *f* electrons; accordingly, the La*4d* core level is not distorted by multiplet splitting [90]. The intensity ratio between the components is of 1:1, in agreement with Klyushnikov et al. [90] for $La_{0.7}Ca_{0.3}MnO_3$ samples. On the high-binding-energy side of the La$4d_{5/2}$-$4d_{3/2}$ doublet, there is a satellite structure, which is due to the monopole excitation effect. In the case of La_2O_3, this effect is interpreted as the transition of an O*2p* valence electron to the unfilled shell La*4f* [90]. In our sample the satellite is separated by 4.5 eV from the La$4d_{5/2}$ peak and broadens it.

The Sr spectrum, as shown in figure 3.2, contains two features. The first is a doublet at 132.6 ± 0.2 eV binding energy, with a separation of 1.8 eV between the Sr3$d_{3/2}$ and Sr3$d_{5/2}$ peaks. The second is a doublet at 133.9 ± 0.2 eV, with the same separation of 1.8 eV between the Sr3$d_{3/2}$ and Sr3$d_{5/2}$ components. The low-energy component can be attributed to Sr in the manganite structure, while the high-binding energy component corresponds to the position of Sr in SrO [91]. So I can expect SrO termination layer for this sample.

Binding energies for the Mn2$p_{1/2}$ and Mn2$p_{3/2}$ levels are equal to 652.7 ± 0.3 eV and 641.2 ± 0.3 eV for the Mn^{3+} components, and 655.2 ± 0.3 eV and 643.7 ± 0.3 eV for the Mn^{4+} ones, respectively. The exchange splitting between the Mn2$p_{1/2}$ and Mn2$p_{3/2}$ components results of 1.5 eV, in close agreement with the Mn2*p* levels reported by Decorse *et al*. [91] for $La_{0.5}Sr_{0.5}MnO_3$ thin films.

The O*1s* spectra exhibited very complex envelopes of several contributions due to the presence of different oxidised species with different chemical states. After curve fitting (figure 3.2) three components were found at 529.3 ± 0.3 eV, 530.8 ± 0.3 eV, 532.6 ± 0.3 eV, which I can attribute to oxygen associated with Mn, La, and Sr, as done by other authors [91, 92]. In so doing, I have effectively assumed that the contributions to the O1*s* due to impurities on the surface as carbonates or carbide are really small.

The quantitative evaluation of the relative concentration of each species by the XPS data can be calculate by:

$$\%n_i = 100\ (n_i / \sum n_i)$$

where n_i is proportional to the atomic concentration of the element *i*:

$$n_i = I_i / s_i$$

where I_i is the integrated intensity of the element *i* and s_i the sensitivity factor:

$$s_i = \sigma_i \cdot L_{ij}(\gamma) \cdot \lambda_i(KE) \cdot T(KE) \cdot \cos\theta$$

which consists of the following terms: σ_i is the photoionization cross section (function of the photoelectron transition) [93], $L_{ij}(\gamma)$ is the angular asymmetry factor [94], λ_i is the inelastic mean free path [95], T(KE) is the transmission correction and θ is the take-off angle of the photoelectrons measured with respect to the surface, KE is the kinetic energy. For the used instrument I do not apply angular correction because it has a "magic angle" arrangement

(54,73° excitation source-analyser angle). The transmission correction was experimentally determined [96].

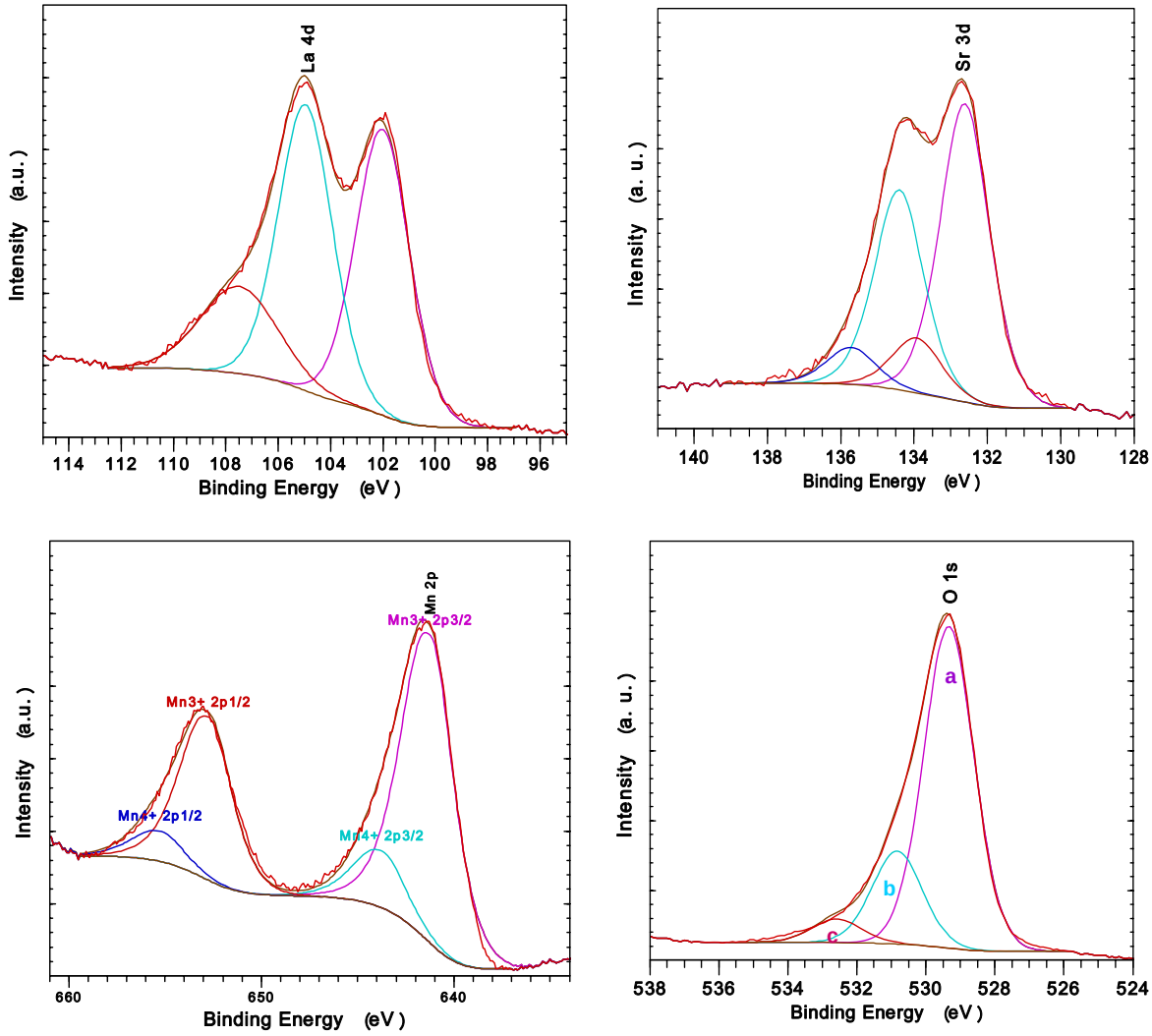

Figure 3.2. Detailed XPS spectra (Mg-Kα, 40 eV pass energy) of La*4d*, Sr*3d*, Mn*2p* (Mn^{3+} and Mn^{4+} components are indicated), and O*1s* (chemical shifts due to: a. Mn atom, b. La atom, c. Sr atom) from $La_{0.7}Sr_{0.3}MnO_3$ film grown on $SrTiO_3$ (001).

The results of the stoichiometry estimation are reported in table 3.1, not taking into account photoelectron diffraction effects, and eventual elastic scattering at low take-off angle. Within the error of such evaluation, that is typically 10%, the stoichiometry is essentially the expected one for 90° take-off. Only minor modifications of the optimum mixed-valence Mn state occur in the escape depth analyzed. However, the data of table 3.1 when decreasing the

probe depth (from 90° to 30°) point toward Mn depletion at surface, fully compatible with an outermost (La/Sr)O layer. Izumi *et al*. [97], for example, evidenced the influence of the manganite termination on the physical properties, when the manganite is a layer of a complex multilayer. Therefore, the chemical characterization results crucial in view of applications in complex multilayers, where the transport properties are determined by the interfacial properties.

θ	***La^{3+} mole fraction***	***Sr^{2+} mole fraction***	***Mn^{3+} mole fraction***	***Mn^{4+} mole fraction***	***O^{2-} mole fraction***
90°	0.73	0.31	0.73	0.20	3.00
60°	0.70	0.31	0.59	0.18	3.00
30°	0.77	0.32	0.56	0.18	3.00

Table 3.1. Relative stoichiometry of $La_{0.7}Sr_{0.3}MnO_3$ film on $SrTiO_3$ (001).

3.1.2. Structural characterization.

3.1.2.1. High resolution x-ray diffraction.

Room temperature high resolution x-ray diffraction (HRXRD) analyses were performed to characterize the structural properties of $La_{0.7}Sr_{0.3}MnO_3$ thin films, of thicknesses 13 nm and 45 nm, deposited on $SrTiO_3$ (001) substrate.

Rocking curve (also called ω scan) on the (002) symmetric reflection of the 13 nm thick film has been performed (see figure 3.3). In this measurements the crystal is rotated by an angle *ω* about an axis perpendicular to the scattering plane. Since broadening of a rocking curve is caused by film crystal structural defects, the full-width at half-maximum (FWHM) value is taken as a significant figure of merit for crystal quality. The (002) $La_{0.7}Sr_{0.3}MnO_3$ film rocking curve has FWHM = 0.022^o, which indicates an excellent degree of crystalline order and so the absence of structural defects.

HRXRD ω/2θ patterns (also called offset scans) of the (002) symmetric reflection of $La_{0.7}Sr_{0.3}MnO_3$ film on $SrTiO_3$ (001) have been performed (see figure 3.4) to characterize the crystal properties of the two deposited manganite films and to obtain the epitaxial relationship between the film and the substrate.

Well defined Pendellösung interference fringes are clearly visible in the ω/2θ scan of the (002) reflection (figure 3.4), which is another measure of the high quality structure of the films. In fact, Pendellösung fringes indicate coherent, high quality layers. From the simulation with a commercial software [98] of the ω/2θ patterns of the (002) reflection of both the films I have calculated the lattice mismatch Δc/c = - 0.013, the out of plain lattice parameter c_{film} = 3.854 ± 0.001 Å, which results compressive strained respect to the bulk a_c = 3.873 Å, and a films thickness estimation t = 10 ± 1 nm and 44 ± 1 nm, respectively.

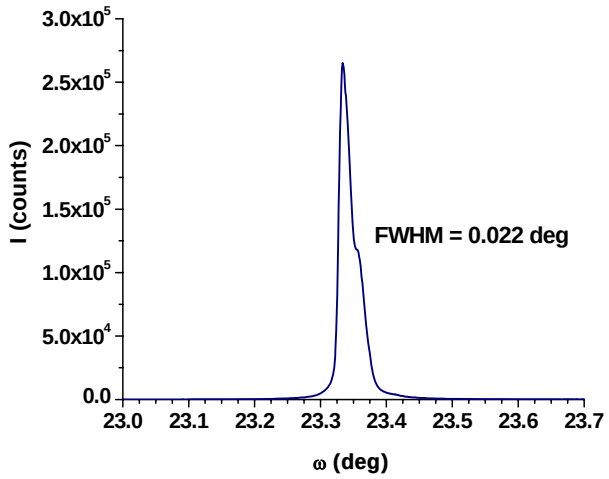

Figure 3.3. Rocking curve of the $(002)_c$ symmetric reflection of $La_{0.7}Sr_{0.3}MnO_3$ film grown on $SrTiO_3$ (001).

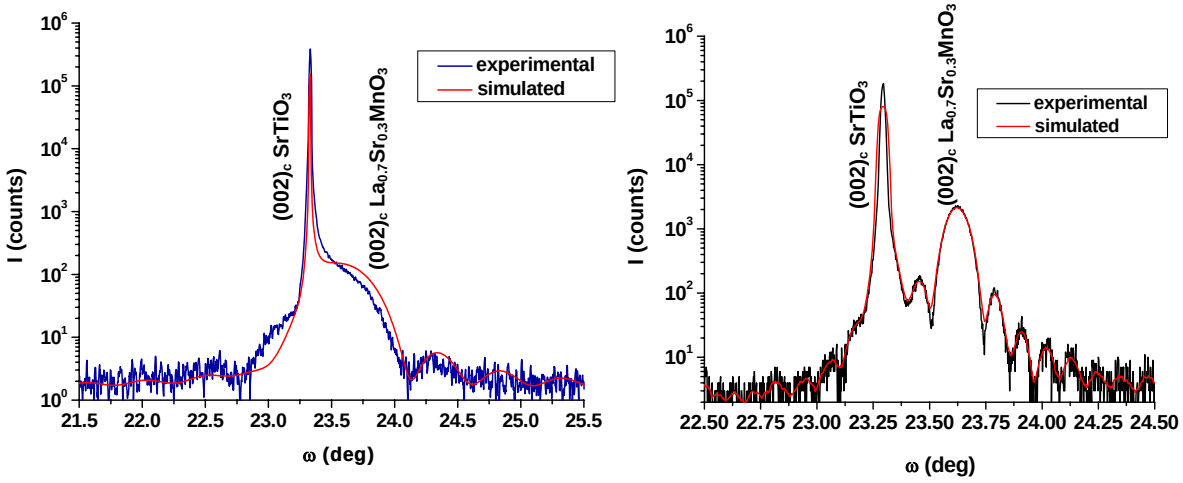

Figure 3.4. ω/2θ scan of the $(002)_c$ symmetric reflection of $La_{0.7}Sr_{0.3}MnO_3$ films grown on $SrTiO_3$ (001) with t = 10 nm (on the left) and t = 44 nm (on the right), respectively.

With the aim of evaluating the relaxation degree of the films, reciprocal space maps (RSM) have been recorder around asymmetric reflections. The collection of a RSM consists of iterated ω scans at fixed 2θ values, for a certain range of $\omega/2\theta$, around a given reciprocal node of substrate, or, alternatively, of iterated q_x scans (transverse scan) for a certain range of the q_z coordinate (longitudinal scan) around the corresponding point (q_x, q_z). The resulting two-dimensional map will contain the scattered intensity associated with the reciprocal nodes of the analyzed structure. In a pseudo-cubic approximation, if we have a relaxed material grown on the substrate, we expect to have reciprocal space nodes of both substrate and layer aligned in $\omega/2\theta$ direction, that for a asymmetrical reflection is represented by the line connecting the origin of reciprocal space (000) to the node corresponding to the asymmetric reflection of the substrate. If we have a fully strained film grown on the substrate, we have reciprocal space nodes of both substrate and layer aligned along q_z direction. In the following, the reciprocal space maps have Miller indexes H, L as (x, y) coordinates. The relation between H and L and the scattering vector q_x and q_z are:

$$q_x = \frac{2\pi}{a} H\,, \qquad q_z = \frac{2\pi}{a} L\,,$$

where a is the lattice parameter in pseudo-cubic approximation.

Being the analyzed samples constituted by $La_{0.7}Sr_{0.3}MnO_3$ (001) grown on $SrTiO_3$ (001), the $(103)_c$, $(-103)_c$ and $(113)_c$ planes are not parallel to the deposition surface. Therefore, they can be chosen to produce an asymmetric reflections. Such reflections enables one to extrapolate information related to in plane and out of plane lattice parameters. The RSMs of $(103)_c$, $(-103)_c$ and $(113)_c$ asymmetric reflections of the $La_{0.7}Sr_{0.3}MnO_3$ films deposited on $SrTiO_3$ (001), were collected following the procedure above described. Even 44 nm thick $La_{0.7}Sr_{0.3}MnO_3$ film results fully strained showing in-plane matching with the substrate lattice parameters being reciprocal space nodes of both substrate and layer aligned along q_z direction (see figure 3.5). Therefore, it is possible to conclude that $La_{0.7}Sr_{0.3}MnO_3$ film is fully strained, assuming in plane lattice parameters a = b = 3.905 ± 0.001 Å, to be compared with the pseudo-cubic bulk parameter a_c = 3.873 Å.

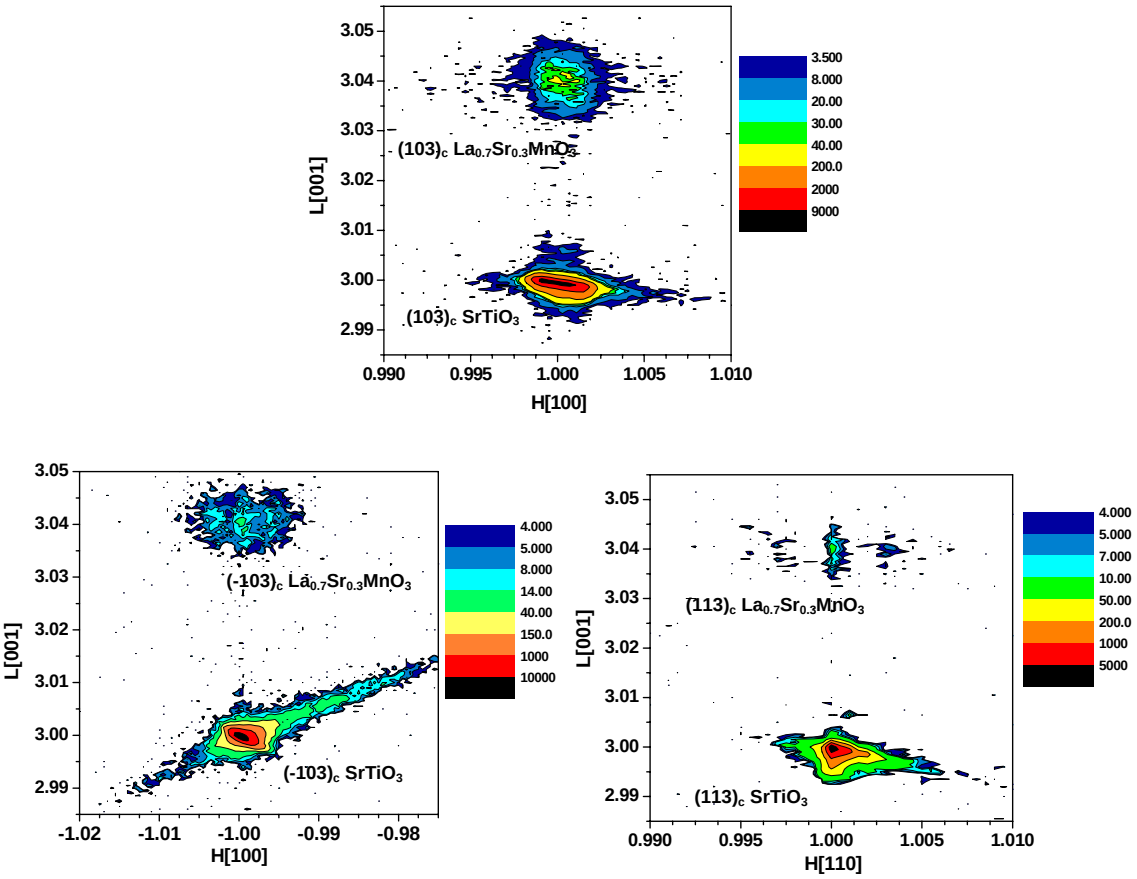

Figure 3.5. RSMs of $(103)_c$ (on the top), $(-103)_c$ (on the left) and $(113)_c$ (on the right) asymmetric reflections of $La_{0.7}Sr_{0.3}MnO_3$ film.

The $La_{0.7}Sr_{0.3}MnO_3$ film results fully strained for both thickness t = 10 nm and t = 44, possessing a tetragonal cell with lattice parameters a = b = 3.905 ± 0.001 Å and c = 3.853 ± 0.001 Å.

3.1.2.2. High resolution transmission electron microscopy.

The high resolution transmission electron microscopy (HREM) measurements and analysis have been performed with the aim to get information about the nanostructure of $La_{0.7}Sr_{0.3}MnO_3$ film grown on $SrTiO_3$ (001) and to see if and how the structural properties of the substrate influence the structure of the overgrown film.

High resolution transmission electron microscopy cross-section images on thin film of $La_{0.7}Sr_{0.3}MnO_3$ deposited onto $SrTiO_3$ (001) oriented have been collected and analyzed (figure 3.6). For cross section observation, thin electron transparent lamellae (tens of nanometers) have been prepared by means of conventional mechanical milling, followed by ion milling to achieve the necessary transparency to obtain high resolution transmission electron image.

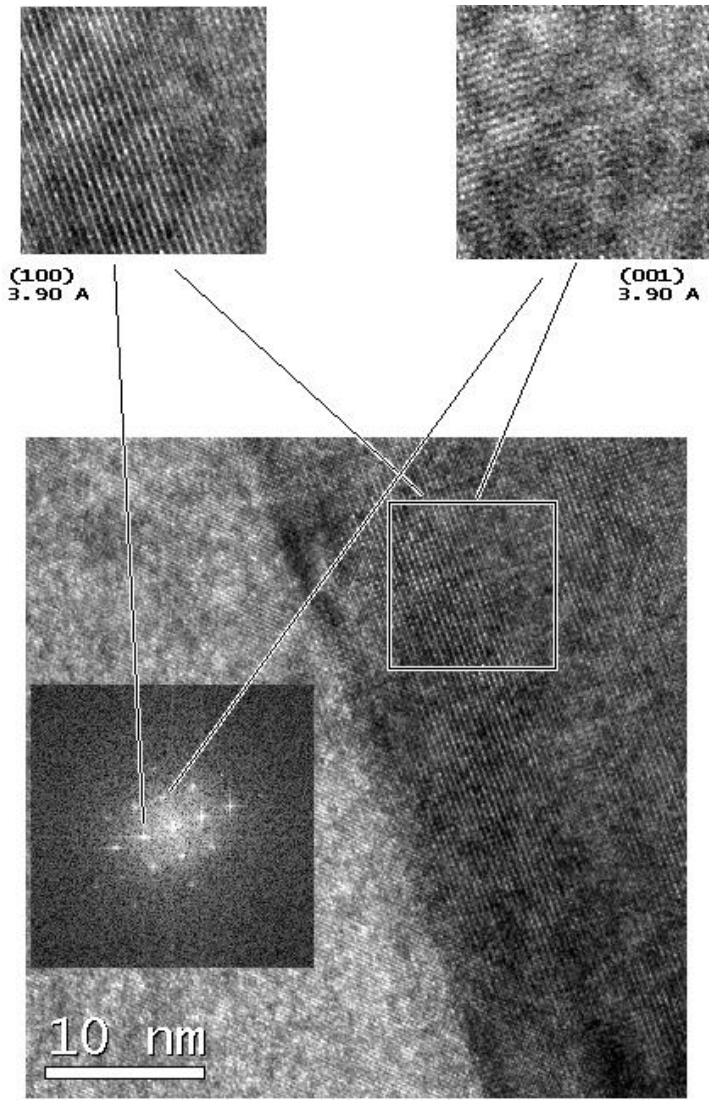

Figure 3.6. HREM analysis of $La_{0.7}Sr_{0.3}MnO_3$ film grown onto $SrTiO_3$ (001). The white square indicates the analyzed film region, the inset shows the diffraction pattern, while the two images on the top are the filtered images of the (100) and (001) planes, respectively.

The used image analysis procedure consists, firstly, in the TEM image collection. At a second step, two-dimensional fast Fourier transform (2D-FFT) was carried out on a region, selected in the film area, indicated by the white square in the collected image in figure 3.6, yielding a diffraction spectrum (shown in the inset of figure 3.6). By the mask filtering technique, chosen couples of spots, symmetric respect to the bright central one, have been selected in the diffractogram to calculate the interplanar distances and angles between different planes. For $La_{0.7}Sr_{0.3}MnO_3$ films we identified a cubic symmetry, with interplanar distances between the (100) and (001) planes equal to 3.90 Å. Finally, the inverse 2D-FFT were applied to form two filtered images (figure 3.6), which show the (100) and (001) planes, respectively.

Besides in figure 3.6 it is possible to see that the $La_{0.7}Sr_{0.3}MnO_3$ appears darker than $SrTiO_3$. There are two distinct reasons. First, during the sample preparation it was observed that $La_{0.7}Sr_{0.3}MnO_3$ is harder than $SrTiO_3$, so that a slight different in thickness is possible. Second, the electronic density of $La_{0.7}Sr_{0.3}MnO_3$ is higher, resulting in a higher absorption coefficient of the electron beam. Such measurements do not show any sign of relaxation of the $La_{0.7}Sr_{0.3}MnO_3$ structure, indicating that the film is completely strained on the substrate, in agreement with the XRD measurements. Moreover, neither dislocations nor stacking faults were found.

3.1.3. Magnetic characterization.

All the magnetic measurements are performed by applying the magnetic field along an in-plane direction, parallel to a side of the sample. Zero-field-cooled (ZFC) magnetic moments (M_{ZFC}) were measured by cooling the sample in a zero magnetic field and then increasing the temperature in a static field, while field-cooled (FC) magnetic moments (M_{FC}) were obtained by cooling the sample in the same static field.

The temperature dependence of the M_{FC} and M_{ZFC} of $La_{0.7}Sr_{0.3}MnO_3$ film (10 nm thick) grown on $SrTiO_3$ (001) were measured at 5 Oe in the range $4.2 \leq T \leq 390$ K (see figures 3.7). $La_{0.7}Sr_{0.3}MnO_3$ film grown on $SrTiO_3$ (001) exhibits a PM/FM transition at $T_C = 325 \pm 1$ K, which is a smaller temperature with respect to the bulk one ($T_C \approx 380$ K), but comparable to the other films one (T_C

= 320 K for t = 25 nm [56], T_C = 315 for t = 70 nm [61]). At 105 K the cubic to tetragonal ferroelastic transition of $SrTiO_3$ substrate, produces the visible effect in the M_{FC} and M_{ZFC} curves of $La_{0.7}Sr_{0.3}MnO_3$ film (figures 3.7).

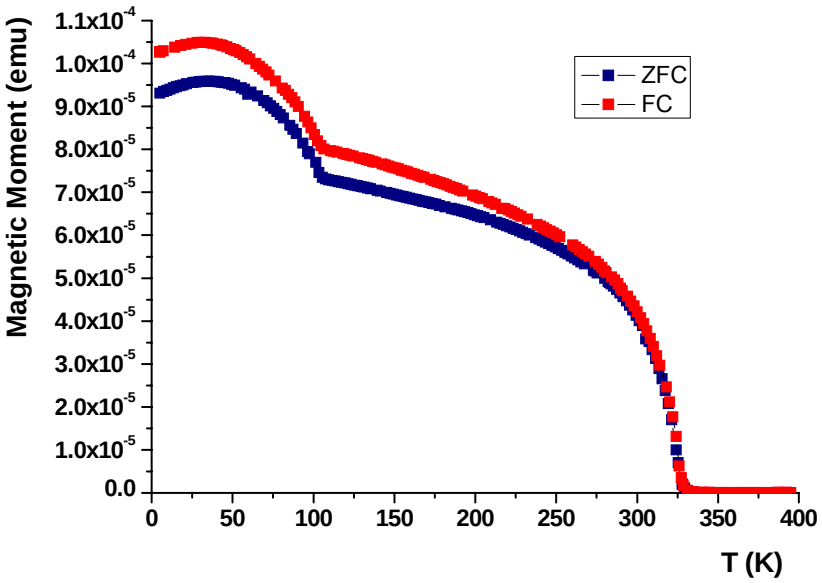

Figure 3.7. M_{ZFC} and M_{FC} curves of $La_{0.7}Sr_{0.3}MnO_3$ film obtained with a static magnetic field of 5 Oe.

3.2. Characterization of $Pr_{0.7}Ca_{0.3}MnO_3$ films grown on $SrTiO_3$ (001).

During my PhD research I have characterized a series of $Pr_{0.7}Ca_{0.3}MnO_3$ films deposited on $SrTiO_3$ (001) with the aim of determining the best deposition conditions, to optimize the growth, and to estimate the critical thickness (definition in par. 2.2). In the following I present only results on fully strained epitaxial films with thickness less than 15 nm, that is the determined critical thickness for $Pr_{0.7}Ca_{0.3}MnO_3$ films.

3.2.1. Chemical characterization.

The chemical characterization of the $Pr_{0.7}Ca_{0.3}MnO_3$ films grown on $SrTiO_3$ (001) has been carried out using the x-ray photoelectron spectroscopy (XPS). The XPS measurements and data analysis have been performed as described in par.

3.1.1, using a pass energy for the electron analyzer of 50 eV for the survey spectrum acquisition and 30 eV for detailed spectra. To compensate for sample charging during analysis, the binding energies were referred to the carbon *1s* signal at 285.0 eV.

Elemental identification of the sample surface was carried out using the information from the survey spectrum. The survey spectra, collected with a photoelectron take-off angle of 90°, from $Pr_{0.7}Ca_{0.3}MnO_3$ film deposited on $SrTiO_3$ (001) substrate, is showed in figure 3.8. The following elements with intense peaks were detected: Pr, Ca, Mn, O, only trace of impurities are present.

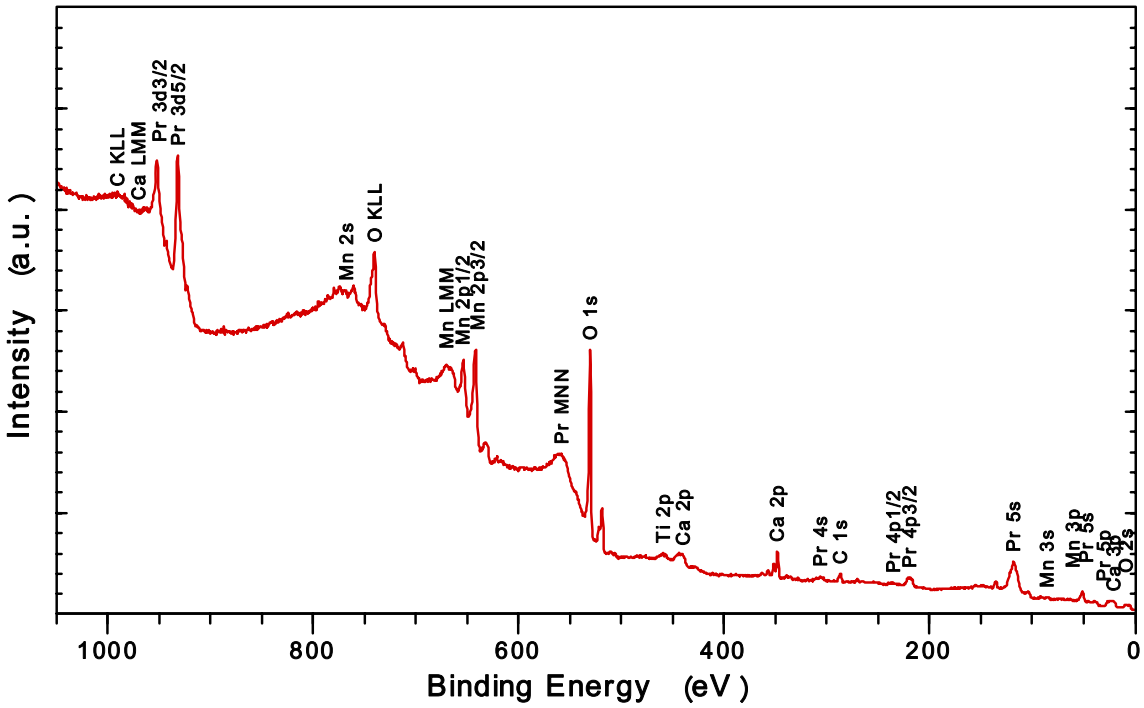

Figure 3.8. XPS survey spectra (Mg-Kα, 50 eV pass energy, 90° photoelectron take-off angle) from $Pr_{0.7}Ca_{0.3}MnO_3$ film grown on $SrTiO_3$ (001).

Quantitative analysis, that I have carried out, was done under the assumption of homogeneous sample, and has permitted to calculate the correct stoichiometry of the sample. The high resolution measurements for quantitative analysis were performed at 20° and 90° photoelectron take-off angles (respect to the sample surface) with the aim to characterize the surface termination of the sample.

High-resolution spectra after the satellite subtraction and fitting of the Pr3*d*, Ca2p, Mn*2p*, and O*1s* core levels are displayed in figure 3.9.

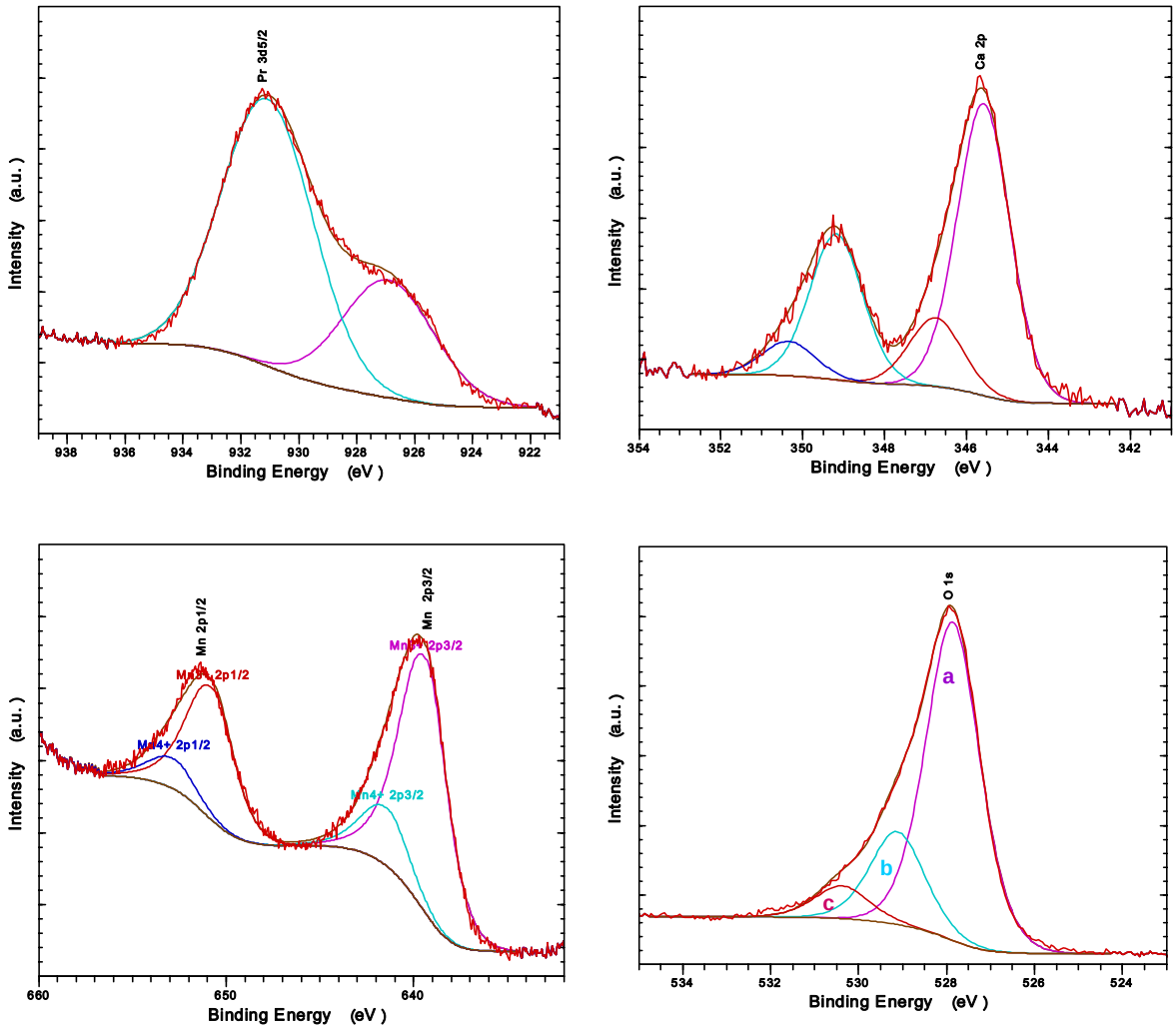

Figure 3.9. Detailed XPS spectra (Mg-Kα, 40 eV pass energy) of Pr3*d*, Ca2p, Mn*2p* (Mn^{3+} and Mn^{4+} components are indicated), and O*1s* (chemical shifts due to: a) Mn atom, b) Pr atom, c) Ca atom) from $Pr_{0.7}Ca_{0.3}MnO_3$ film grown on $SrTiO_3$ (001).

Figure 3.9 shows the core level spectrum of Pr$3d_{5/2}$ states. It contains two peaks, which can be understood by considering the exchange splitting of the Pr$3d_{5/2}$ level. In the photoelectron emission process one hole is created in the Pr$3d_{5/2}$ state. The spin state of this hole couples with the spin state of Pr*4f* holes and results in exchange splitting of the Pr$3d_{5/2}$ state. The multiplicity of the doublet thus created is four and two and hence the ratio of the integrated

intensity of the two peaks should be 2:1, which is close to the observed value. The energy separation of the doublet formed by exchange splitting is the energy difference between these two peaks, which is 4.2 eV. These two peaks were also observed in $PrCoO_3$ and $Pr_{1-x}Ca_xFeO_3$ compounds [99, 100].

The Ca*2p* spectrum, as shown in figure 3.9, contains two features at an energy separation of 1.2 eV. Both are doublet with an exchange split of 3.6 eV between the Ca2$p_{1/2}$ and Ca2$p_{3/2}$ components, as observed in CaO [100]. The low-energy component can be attributed to Ca in the manganite structure, while the high-binding energy component can correspond to the Ca in a CaO layer present in surface.

Binding energies for the Mn2$p_{1/2}$ and Mn2$p_{3/2}$ levels are separated by 1.4 eV for both the Mn^{3+} and Mn^{4+}, in close agreement with the Mn2*p* levels reported for $La_{0.7}Sr_{0.3}MnO_3$ thin films in par. 3.1.1.

The O*1s* spectra exhibited very complex envelopes of several contributions due to the presence of different oxidised species with different chemical states. After curve fitting (figure 3.9) three components were found, which I can attribute to oxygen associated with Mn, Pr, and Ca, as done for other manganites [91, 92]. In so doing, I have effectively assumed that the contributions to the O1*s* due to impurities on the surface as carbonates or carbide are really small.

The quantitative evaluation of the relative concentration of each specie by the XPS data was done as described in par. 3.1.1. The results of the stoichiometry estimation are reported in table 3.2, not taking into account photoelectron diffraction effects, and eventual elastic scattering at low take-off angle.

θ	***Pr^{3+} mole fraction***	***Ca^{2+} mole fraction***	***Mn^{3+} mole fraction***	***Mn^{4+} mole fraction***	***O^{2-} mole fraction***
90°	0.67	0.33	0.72	0.21	3.74
20°	0.60	0.40	0.35	0.74	4.26

Table 3.2. Relative stoichiometry of $Pr_{0.7}Ca_{0.3}MnO_3$ film grown on $SrTiO_3$ (001).

Within the error bar of such a evaluation, that is typically 10%, the stoichiometry is essentially the expected one for 90° take-off. Only an enrichment of oxygen content in the escape depth analyzed, due to the growth in oxygen atmosphere. However, the data of table 3.2 when decreasing the probe depth (from 90° to 20°) point toward Ca and O enrichment at surface, fully compatible with an outermost CaO layer.

3.2.2. Structural characterization.

3.2.2.1. High resolution x-ray diffraction and x-ray reflectivity.

In the following I present the *ω/2θ*, *ω*-scan (rocking curve), high resolution reciprocal space maps (RSM) and x-ray reflectivity (XRR) data of $Pr_{0.7}Ca_{0.3}MnO_3$ thin film deposited on $SrTiO_3$ (001).

In particular XRR measurements were carried out in order to estimate the thickness and the surface roughness of the films. In figure 3.10 I show the experimental XRR curve in blue and the calculated curve in red, obtained by fitting with Leptos software [98]. From the fitting we obtain the thickness *t* and the roughness *R* of $Pr_{0.7}Ca_{0.3}MnO_3$ that result: t = 9.9 ± 0.2 nm and R = 0.5 ± 0.2 nm.

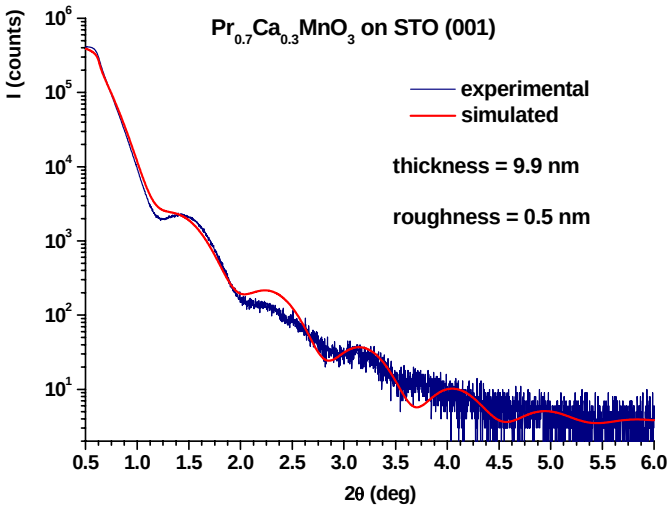

Figure 3.10. Experimental XRR curve in blue and fitting curve in red.

From the *ω/2θ* scan of the (002) cubic reflection (figure 3.11) I have calculated the lattice mismatch $\Delta c/c$ = - 0.024, and the c_{film} = 3.811 ± 0.001 Å, to be compared with the bulk parameter $c_{bulk}/2$ = 3.840 Å.

The full-width at half-maximum (FWHM) of the rocking curve of the film (002) reflection (figure 3.11) is 0.024°, indicating the excellent crystal quality.

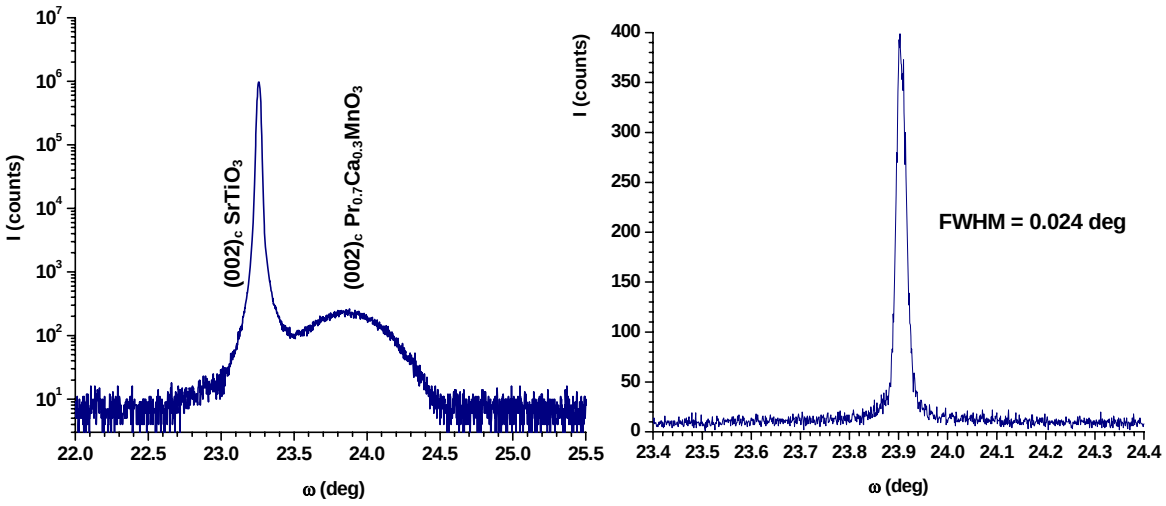

Figure 3.11. *ω/2θ* scan of the $(002)_c$ reflection of film and substrate (on the left) and film rocking curve (on the right).

The figure 3.12 shows the RSMs around the $(002)_c$ symmetric and $(-103)_c$ asymmetric reflections. In particular, the $(-103)_c$ map shows that the film maximum is aligned in H with the $SrTiO_3$ one indicating that the film is fully strained.

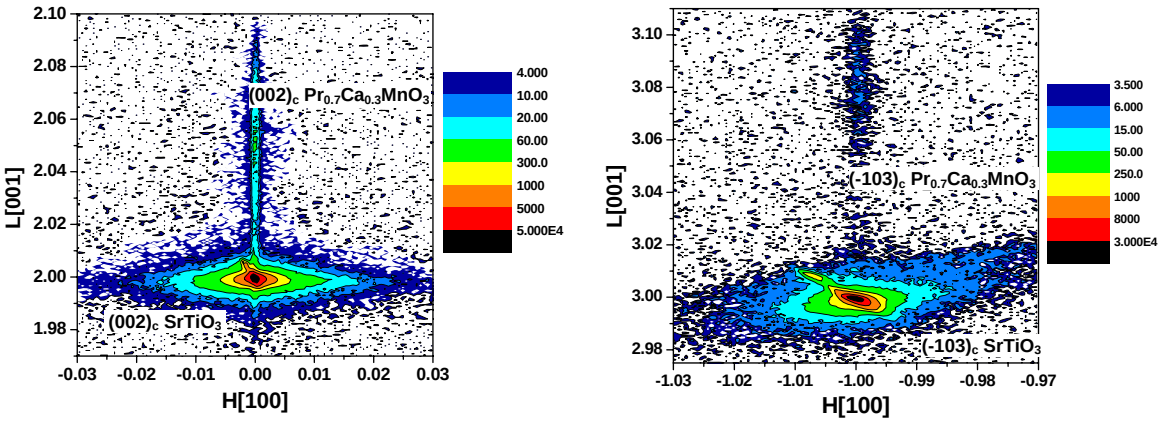

Figure 3.12. RSMs around $(002)_c$ (on the left) and $(-103)_c$ (on the right) reflections.

So I have realized that $Pr_{0.7}Ca_{0.3}MnO_3$ (a_{bulk} = 5.426 Å, b_{bulk} = 5.478 Å, c_{bulk} = 7.679 Å in the Pnma space group) has grown on $SrTiO_3$ (001), undergoing in-plane tensile strain and therefore with the in-plane lattice parameters matched with the substrate one, and with the out-of-plane parameter shorter than the bulk. Therefore, the measurements demonstrate an epitaxial growth with c-axis orientation. I can conclude that $Pr_{0.7}Ca_{0.3}MnO_3$ film is fully strained with a tetragonal cell and lattice parameters a = b = 5.522 ± 0.001 Å (as the $SrTiO_3$ face diagonal $a_c\sqrt{2}$), c = 7.622 ± 0.001 Å.

3.2.2.2. High resolution transmission electron microscopy.

High resolution transmission electron microscopy (HREM) measurements and analysis have been performed with the aim was to get information about the nanostructure of $Pr_{0.7}Ca_{0.3}MnO_3$ deposited onto $SrTiO_3$ (001) oriented and to investigate if and how the structural properties of the substrate influence the structure of the overgrown film.

High resolution transmission electron microscopy cross-section images on $Pr_{0.7}Ca_{0.3}MnO_3$ thin film deposited onto $SrTiO_3$ (001) oriented have been collected and analyzed. For cross section observation, thin electron transparent lamellae (tens of nanometers) have been prepared by means of conventional mechanical milling, followed by ion milling to achieve the necessary transparency to obtain high resolution transmission electron image.

The used image analysis procedure consists, firstly, in the TEM image collection. At a second step, two-dimensional fast Fourier transform (2D-FFT) was carried out on a region, selected in the film area, indicated by the white square in the collected image of figure 3.13, yielding a diffraction spectrum (shown in the inset of figure 3.13). By the mask filtering technique chosen couples of spot symmetric respect to the bright central one have been selected in the diffractogram to calculate the interplanar distances and angles between different planes. For $Pr_{0.7}Ca_{0.3}MnO_3$ film we identified a pseudocubic symmetry, with interplanar distances between (200) planes of 1.95 Å and between (002) planes of 1.94 Å, which means a pseudocubic lattice parameter of 3.90 ± 0.01 Å. Finally, the inverse 2D-FFT were applied to the diffraction pattern, after to have eliminated the noise with the mask technique, to form a filtered image

(shown in figure 3.13), which demonstrates the ordered growth of $Pr_{0.7}Ca_{0.3}MnO_3$ film. Such measurements do not show any sign of relaxation of the $Pr_{0.7}Ca_{0.3}MnO_3$ structure, indicating that the film is completely strained on the substrate, in agreement with the XRD measurements. Moreover, neither dislocations nor stacking faults were found.

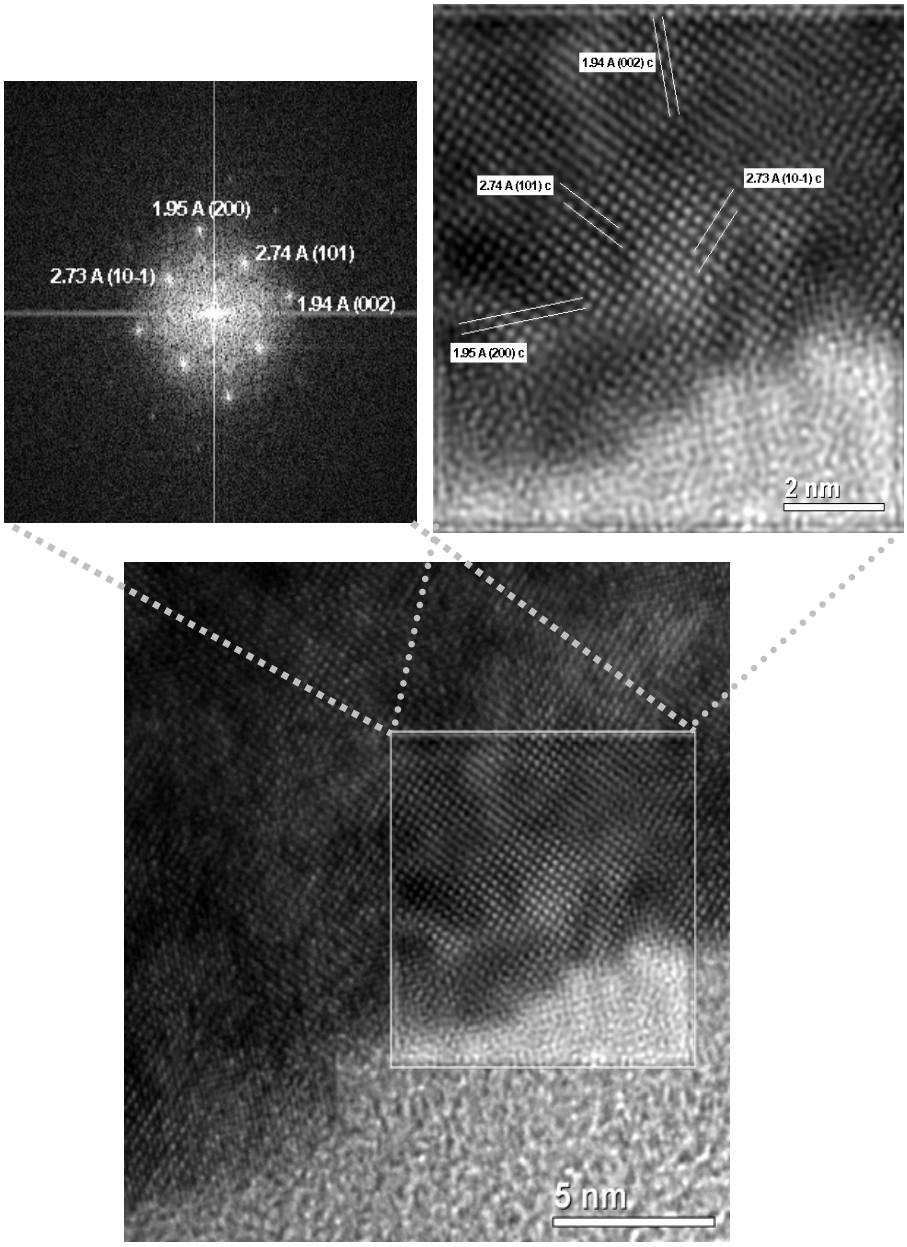

Figure 3.13. HREM analysis of $Pr_{0.7}Ca_{0.3}MnO_3$ film grown onto $SrTiO_3$ (001). The white square indicates the analyzed film region, on the left top the diffraction pattern, on the right top the filtered images, with the indication of (200), (002), (101) and (10-1) planes, are shown.

3.2.3. Magnetic characterization.

All the magnetic measurements have been performed by applying the magnetic field along an in-plane direction, parallel to a side of the sample.

The temperature dependence of the spontaneous magnetic moment (figure 3.14) and the M_{FC} and M_{ZFC} curve of $Pr_{0.7}Ca_{0.3}MnO_3$ grown on $SrTiO_3$ (001) were measured at different field strengths (25 Oe, 100 Oe, 250 Oe, 500 Oe, 750 Oe, 1000 Oe, 1500 Oe, 2000 Oe, 2500 Oe, 4000 Oe, 5200 Oe) in the range $4.2 \leq T \leq 380$ K.

There is experimental evidence of a paramagnetic/ferromagnetic transition with a Curie temperature $T_C = 121 \pm 1$ K, determined at zero magnetic field (figure 3.14).

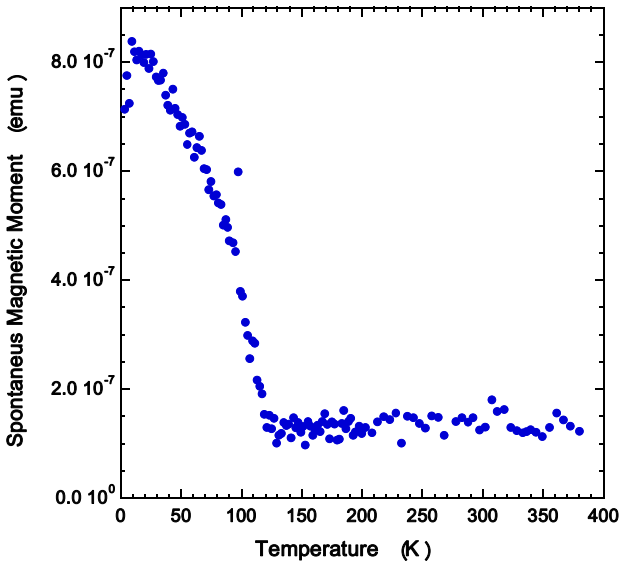

Figure 3.14. Spontaneous magnetic moment versus temperature.

Examples of the behavior observed are given in figure 3.15, which reports chosen M_{FC} and M_{ZFC} curves corresponding to the fields of 25 Oe, 250 Oe, 750 Oe, 1500 Oe, 2500 Oe, 4000 Oe and 5200 Oe in the measured range of temperature. In the low temperature range (below the PM/FM transition temperature), magnetization results dependent on the sample thermal history: a bifurcation between M_{ZFC} and M_{FC} is apparent at an irreversibility temperature

T_{irr}, which is the temperature value at which the irreversible magnetic moment, defined as $\Delta M = M_{FC} - M_{ZFC}$, becomes different from zero, indicating the onset of a freezing process.

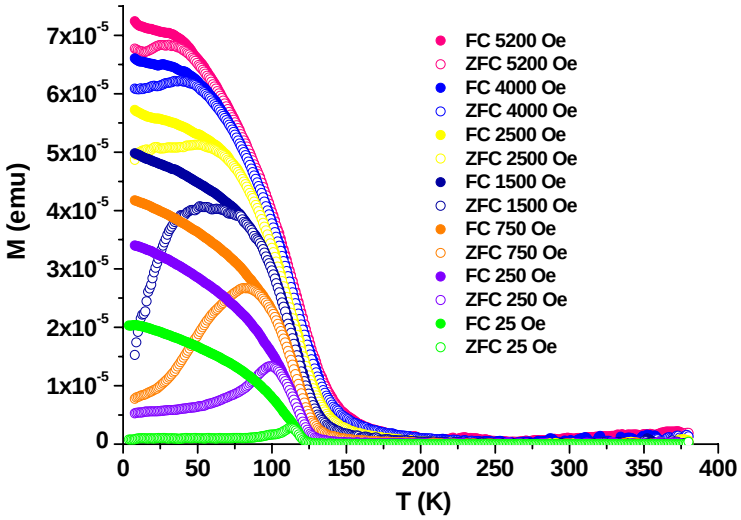

Figure 3.15. M_{ZFC} and M_{FC} curves obtained with static magnetic fields for $Pr_{0.7}Ca_{0.3}MnO_3$ film grown on $SrTiO_3$ (001).

Specifically, it appears that the temperature T_{irr}, that indicates the onset of the freezing process, decreases as H increases according to $T_{irr} \propto H^{2/3}$ (see fig. 3.16, where I report the T_{irr} determined by M_{ZFC} and M_{FC} curves measured at field of 25 Oe, 100 Oe, 250 Oe, 500 Oe, 750 Oe, 1 kOe, 1.5 kOe, 2 kOe). This field dependence corresponds to the so-called de Almeida-Thouless (AT) line given by $H_{AT}(T)/\Delta J \propto (1-T/T_{irr})^{3/2}$ [101]. It marks the starting point of the many-valley structure of phase space leading to diverging relaxation times and to nonergodic behaviour. In addition, the presence of a maximum in M_{ZFC} at the temperature T_{max} is observed at low field (25 Oe), that broadens at higher fields, while T_{max} shifts to lower values together with the corresponding T_{irr}. In figure 3.16 also T_{max}, determined by M_{ZFC} curves, is reported versus $H^{2/3}$, at 25 Oe, 100 Oe, 250 Oe, 500 Oe, 750 Oe, 1 kOe, 1.5 kOe, and 2 kOe magnetic fields. So also T_{max} follows the AT line.

The linear extrapolation of the AT lines of T_{max} to $H = 0$ (shown in the figure 3.16) provides a way of determining the spin-freezing transition

temperature T_f, that in this case results equal to 115 ± 2 K. The use of the AT lines is frequently reported in literature for the determination of the transition temperature of various and different frustrated magnetic systems, which show spin-glass behaviour (see, for instance, references 102, 103 and 104).

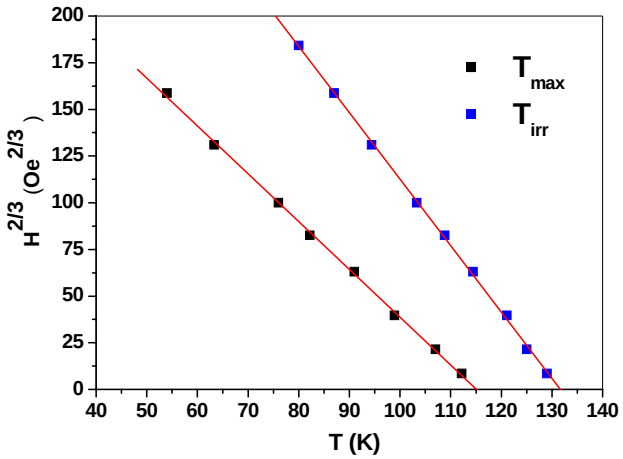

Figure 3.16. Field dependence of the transition temperatures T_{irr} as determined by M_{ZFC} and M_{FC} curves (blue points), and of T_{max} as determined by M_{ZFC} (black points), showing the De Almeida-Thouless lines for $Pr_{0.7}Ca_{0.3}MnO_3$ film grown on $SrTiO_3$ (001).

Another important piece of evidence of the spin-glass behaviour is the time dependence of the remanent magnetization below T_f when the external magnetic field is turned off after crossing T_f. At this point the remanent magnetization typically relaxes following a stretched exponential function of the time t,

$$M(t) = M(0) \exp [a\, t^{(1-b)}]$$

where $M(0)$ is the magnetization value at the beginning of the relaxing process.

The time dependence of remanent magnetization of the sample cooled in a field of 500 Oe was recorded immediately after the field was turned off at 90 K. I present the experimental curve and the fitting in figure 3.17.

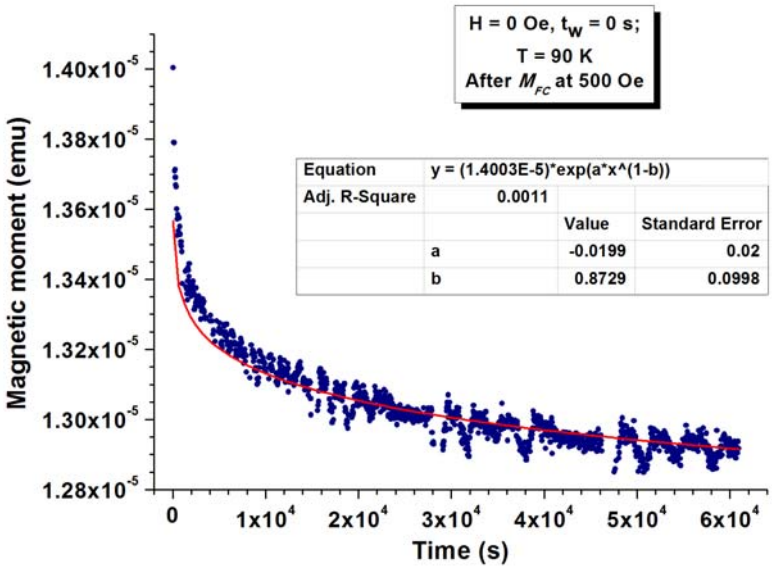

Figure 3.17. *M*(*t*) isothermal relaxation curve measured after M_{FC} down to 90 K, in an external field of 5 kOe, in blue, the fitting has been reported in red.

M_{ZFC} *and* M_{FC} curves were also measured applying the magnetic fields of 25 Oe and 100 Oe in a direction rotated of 90° around the out-of-plane direction of the sample (not presented here) in order to exclude the presence of anisotropy, that in fact was absent.

The irreversible magnetic behaviour of $Pr_{0.7}Ca_{0.3}MnO_3$ can be ascribed to a reentrant spin glass (RSG), because it is also possible to identify a Curie temperature T_C above both T_{max} and T_{irr}. As described by Ito [105], a RSG has to be considered a mixed phase of a long range ferromagnetic phase and a SG phase. The mechanism of the RSG transition is that, when the long range order is established at T_C, some amount of disordered (not aligned) spins exists in the long range ferromagnetic network. With decreasing temperature, even some of the spins participating to the long range order escape from the ordered network, resulting in an increasing amount of the frustrated spins. On further lowering temperature, the frustrated spins freeze at the freezing temperature T_f. I propose to relate the observed magnetic behaviour to the phase separation scenario described in par 1.11 for $Pr_{0.7}Ca_{0.3}MnO_3$ in the bulk form. Therefore, the observed RSG phase has origin from the competition between the antiferromagnetic phase and the ferromagnetic one. In conclusion, I can

suppose that there is the presence of a coreshell-type structure, in which the core is ferromagnetic and metallic while the shell is spin disordered and insulating. This picture has already been used for $La_{0.7}Sr_{0.3}MnO_3$ films with twinned structural domain, in which a RSG phase also has been observed [59], for $La_{0.7}Sr_{0.3}MnO_3$ nanoparticles with surface spin-glass layers formation [106] and for polycrystalline films of $La_{0.7}Sr_{0.3}MnO_3$ which, beside the ferromagnetic core, display spin glass phases related to grain boundaries and grain surfaces [107].

3.3. Characterization of $Pr_{0.7}Ca_{0.3}MnO_3$ films grown on $SrTiO_3$ (110).

3.3.1. Structural characterization.

The structural characterization of $Pr_{0.7}Ca_{0.3}MnO_3$ deposited on $SrTiO_3$ (110) was performed by XRR and HRXRD measurements as above described (in par. 2.1.2). First of all, I have estimate by XRR measurements and fitting the thickness and roughness of $Pr_{0.7}Ca_{0.3}MnO_3$ deposited on $SrTiO_3$ (110), which result: t = 8.4 ± 0.2 nm and R = 0.4 ± 0.2 nm. In figure 3.18 I show the curve in blue with the fitting curve in red.

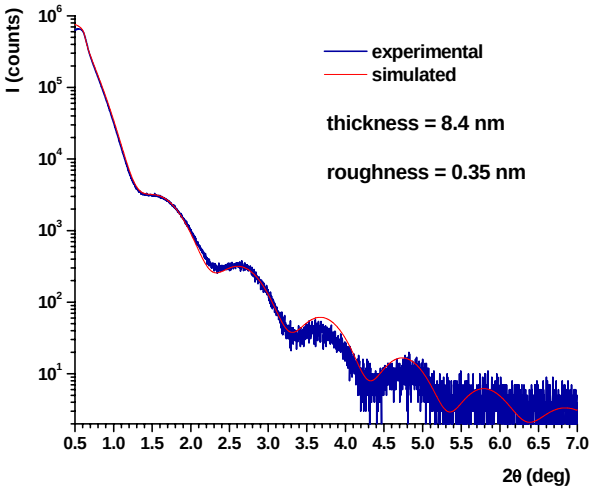

Figure 3.18. Experimental XRR curve in blue and fitting curve in red.

In the following, the complete HRXRD characterization is presented.

First, I want to describe how $Pr_{0.7}Ca_{0.3}MnO_3$ film (a_{bulk} = 5.478 Å, b_{bulk} = 7.679 Å, c_{bulk} = 5.426 Å in the Pnma space group) grows on $SrTiO_3$ substrate (110) oriented. $SrTiO_3$ (110) has the (001) face in-plane, and so in-plane lattice parameters are 3.905 Å and $a_c\sqrt{2}$ = 5.522 Å. The film results $[001]_{orth}$ oriented, i.e. with the $[001]_{orth}$ axis perpendicular to the substrate plane $(110)_c$. From the ω/2θ scan of the $(110)_c$ symmetric reflection (figure 3.19) I have calculated the lattice mismatch Δc/c = -0.02, and the c_{film} = 5.410 ± 0.001 Å, to be compared with the bulk parameter c_{bulk} = 5.426 Å.

The full-width at half-maximum (FWHM) of the film rocking curve (figure 3.19) is 0.021°, so the crystallinity of the films is excellent.

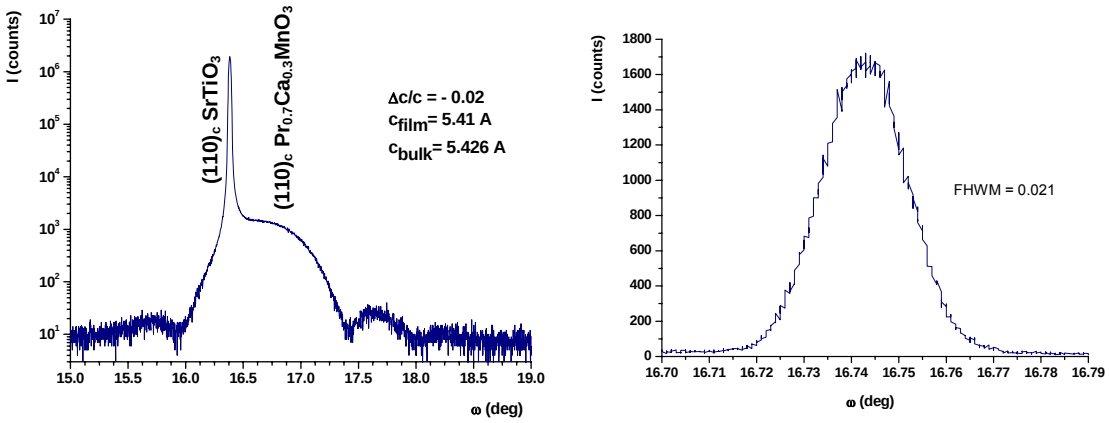

Figure 3.19. ω/2θ scan of the $(110)_c$ reflection (on the left) and film rocking curve (on the right).

The figure 3.20 shows the RSMs around the $(110)_c$ symmetric and $(310)_c$, $(22\text{-}2)_c$ asymmetric reflections, respectively. In particular the $(310)_c$ and $(22\text{-}2)_c$ maps show that the film maximum is aligned in H with the $SrTiO_3$ one indicating that the film is fully tensile strained.

So I have realized that $Pr_{0.7}Ca_{0.3}MnO_3$ grown on $SrTiO_3$ (110), being under in-plane tensile strain, shows the in-plane lattice parameters matched with the substrate ones, and the out-of-plane parameter *c* shorter than the bulk one. The measurements demonstrate an epitaxial growth on $SrTiO_3$ (110). I can conclude that $Pr_{0.7}Ca_{0.3}MnO_3$ film is fully strained with lattice parameters a =

5.522 ± 0.001 Å, b = 7.810 ± 0.001 Å, and c = 5.410 ± 0.001 Å in the orthorhombic Pnma space group.

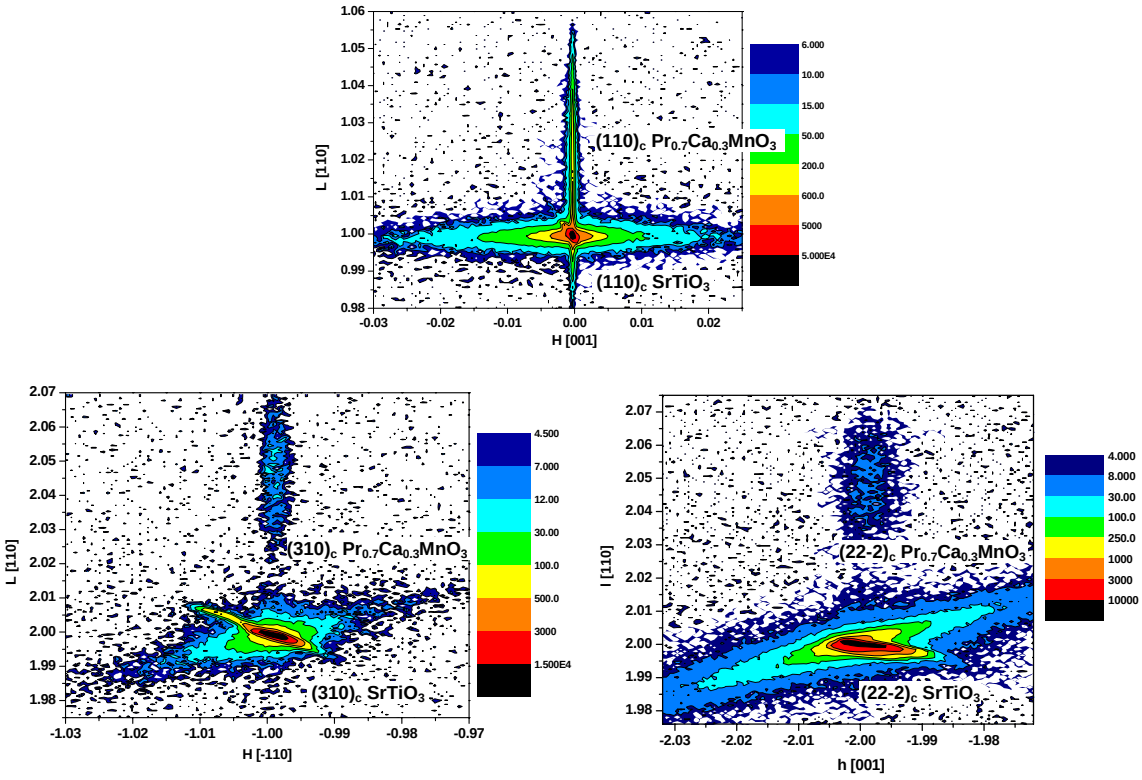

Figure 3.20. RSMs around $(110)_c$ reflection, $(310)_c$ reflection and $(22\text{-}2)_c$ reflection.

3.3.2. Magnetic characterization.

In the following I present the magnetization measurements on $Pr_{0.7}Ca_{0.3}MnO_3$ grown on $SrTiO_3$ (110). All the magnetic measurements have been performed applying the magnetic field parallel to a side of the sample, along the b_{orth} axis in-plane direction.

The temperature dependence of the spontaneous magnetic moment and the M_{FC} and M_{ZFC} versus temperature of $Pr_{0.7}Ca_{0.3}MnO_3$ were measured for 5 Oe and 10 kOe magnetic field and the M_{FC} at 1 kOe, in the range $4.2 \leq T \leq 380$ K (see figures 3.21).

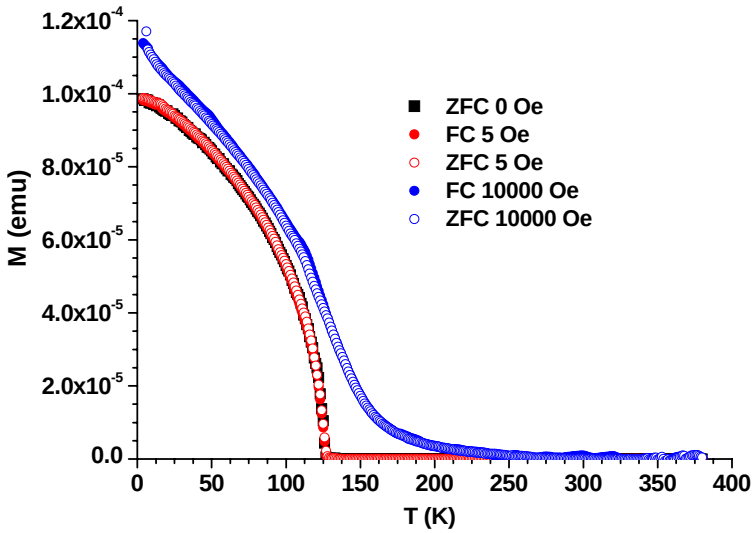

Figure 3.21. Spontaneous magnetic moment, M_{ZFC} and M_{FC} curves versus temperature. obtained with a static magnetic field of 5 Oe, 10000 Oe for $Pr_{0.7}Ca_{0.3}MnO_3$ film grown on $SrTiO_3$ (110).

There is experimental evidence of a PM/FM transition at 127 ± 1 K (see figure 3.21), the T_C is determinate at zero magnetic field.

This result is relevant for the future applications in device. In fact, with this kind of biaxial tensile strain, produced by $SrTiO_3$ (110), no signs of phase separation, present in bulk $Pr_{0.7}Ca_{0.3}MnO_3$ [36], are visible, while only a pure long-range FM order below T_C is observable.

3.4. Characterization of $Pr_{0.5}Ca_{0.5}MnO_3$ films grown on $SrTiO_3$ (001).

3.4.1. Structural characterization.

The structural characterization of $Pr_{0.5}Ca_{0.5}MnO_3$ deposited on $SrTiO_3$ (001) was performed by XRR and HRXRD measurements as above described (in par. 2.1.1). First of all, I have estimate by XRR measurements and fitting the thickness t and the roughness R of $Pr_{0.5}Ca_{0.5}MnO_3$ deposited on $SrTiO_3$ (110), which result: t = 9.5 ± 0.2 nm and R = 0.5 ± 0.2 nm. In figure 3.22 I show the experimental XRR curve in blue with the fitting curve in red.

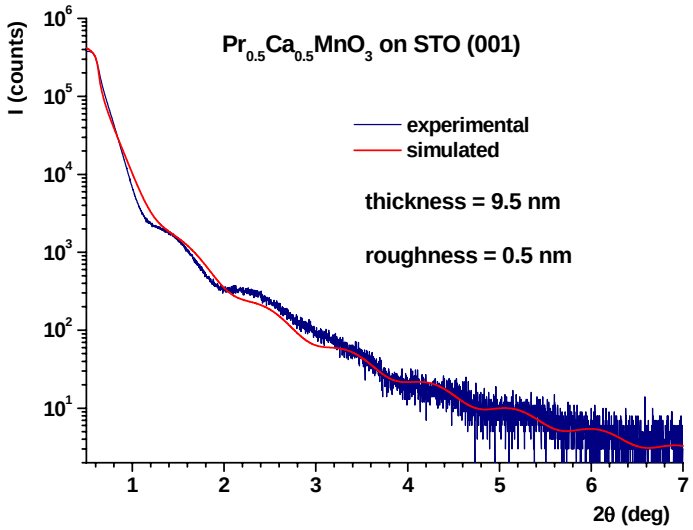

Figure 3.22. Experimental XRR curve in blue and fitting curve in red.

I remind that $Pr_{0.5}Ca_{0.5}MnO_3$ has bulk lattice parameters a = 5.395 Å, b = 5.403 Å, c = 7.612 Å in the Pbnm space group. The cubic lattice parameter of $SrTiO_3$ is 3.905 Å ($a_c\sqrt{2}$ = 5.522 Å).

From the ω/2θ scan of the (002) cubic reflection (figure 3.23) I have calculated the lattice mismatch Δc/c = - 0.04, and the c_{film} = 3.747 ± 0.001 Å, to be compared with the bulk parameter c/2 = 3.806 Å.

The full-width at half-maximum (FWHM) of the film rocking curve (figure 3.23) is 0.026°, so the crystallinity is excellent.

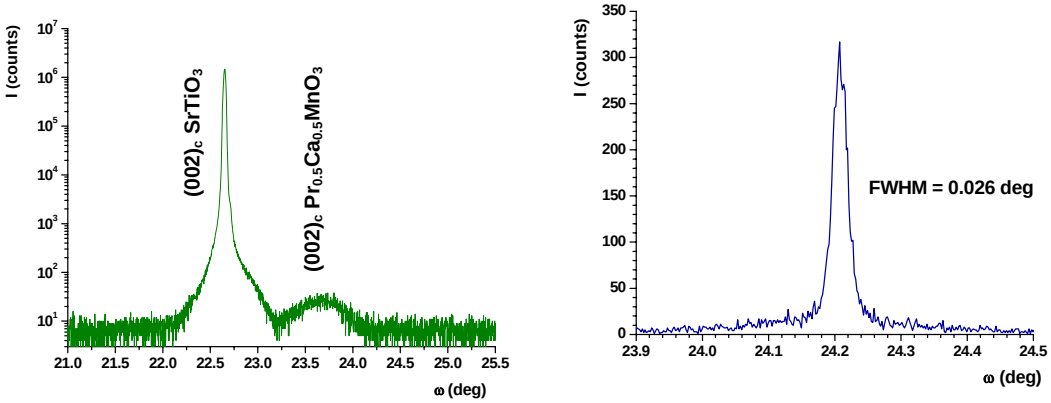

Figure 3.23. ω/2θ scan of the $(002)_c$ reflection of film and substrate and $(002)_c$ film rocking curve.

The figure 3.24 shows the RSMs around the $(002)_c$ symmetric and $(-103)_c$ asymmetric reflections of substrate and $Pr_{0.5}Ca_{0.5}MnO_3$. In particular the $(-103)_c$ map shows that the film maximum is aligned in H with the $SrTiO_3$ one indicating that the film is fully strained.

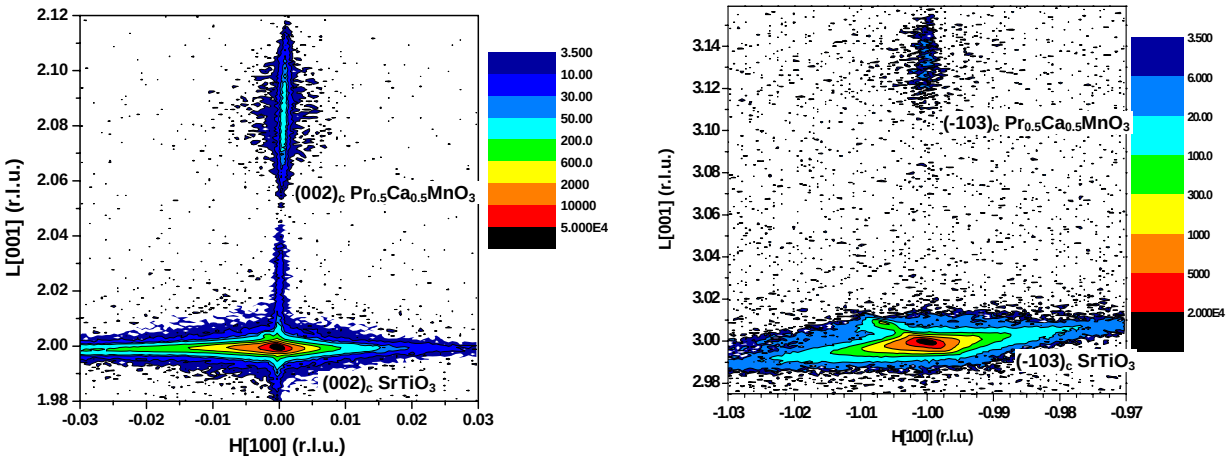

Figure 3.24. RSMs around $(002)_c$ symmetric reflection and $(-103)_c$ asymmetric reflection.

So I have realized that $Pr_{0.5}Ca_{0.5}MnO_3$ film grows on $SrTiO_3$ (001), undergoing in-plane tensile strain, shows the in-plane lattice parameters matched with the substrate ones, and the out-of-plane parameter c shorter than the bulk one. The measurements demonstrate an epitaxial growth with c-axis orientation. I can conclude that $Pr_{0.5}Ca_{0.5}MnO_3$ film is fully strained with a tetragonal cell and lattice parameters a = b = 5.522 ± 0.001 Å (as the $SrTiO_3$ face diagonal $a_c\sqrt{2}$) and c = 7.494 ± 0.001 Å.

3.4.2. Magnetic characterization.

In the following I present the magnetization measurements on $Pr_{0.5}Ca_{0.5}MnO_3$ grown on $SrTiO_3$ (001). All the magnetic measurements are performed applying the magnetic field along the [001] in-plane direction, parallel to a side of the sample.

The temperature dependence of the M_{FC} and M_{ZFC} of $Pr_{0.5}Ca_{0.5}MnO_3$ was measured for different field strengths (1 kOe, 7.5 kOe and 20 kOe) in the range $4.2 \leq T \leq 380$ K (see figure 3.25).

As it is possible to see from the figures 3.26, the $Pr_{0.5}Ca_{0.5}MnO_3$ film deposited on $SrTiO_3$ (001) presents a paramagnetic behaviour. The increase of magnetization above ~ 350 K may be related to a possible melting of the CO state, even though a more complete investigation should be devoted to this controversial subject. Besides, a bump seems to be present at around 150 K in the curves at 20 kOe (figure 3.26), that could be associated to the AFM transition present in the $Pr_{0.5}Ca_{0.5}MnO_3$ bulk at around 180 K.

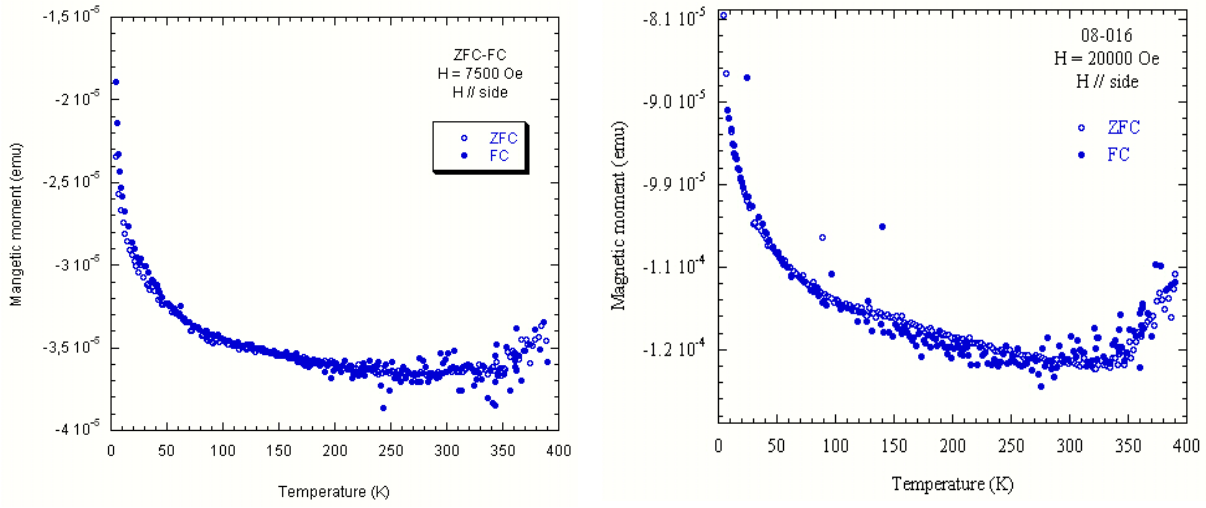

Figure 3.25. M_{ZFC} and M_{FC} curves obtained with the static magnetic fields of 7.5 kOe (on the left) and 20 kOe (on the right).

Therefore, the effect of the tensile strain on $Pr_{0.5}Ca_{0.5}MnO_3$ is a strong weakening in the charge ordering/antiferromagnetic order in favour of a paramagnetic behaviour.

3.5. Characterization of $Pr_{0.5}Ca_{0.5}MnO_3$ films grown on $SrTiO_3$ (110).

3.5.1. Structural characterization.

The structural characterization of $Pr_{0.5}Ca_{0.5}MnO_3$ deposited on $SrTiO_3$ (110) was performed by XRR and HRXRD measurements as above described (in par.

2.1.1). First of all, I have estimated by XRR measurements and fitting the thickness and roughness of $Pr_{0.5}Ca_{0.5}MnO_3$ deposited on $SrTiO_3$ (110): t = 7.4 ± 0.2 nm and R = 0.5 ± 0.2 nm. In figure 3.26 I show the experimental XRR curve in blue with the fitting curve in red.

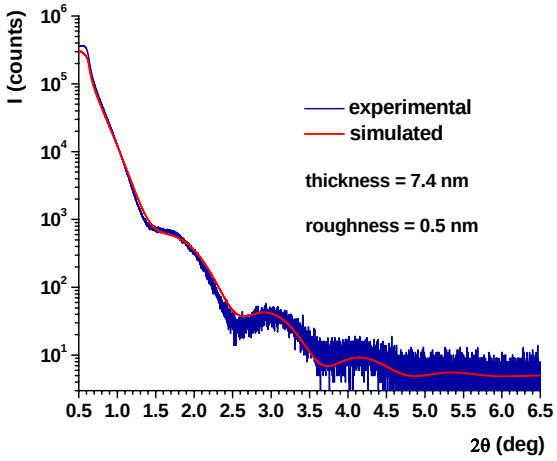

Figure 3.26. Experimental XRR curve in blue and fitting curve in red.

From the ω/2θ scan of the (002) cubic reflection (figure 3.27) I have calculated the lattice mismatch Δc/c = -0.03, and the c_{film} = 5.380 ± 0.001 Å, to be compare with the bulk parameter c = 5.403 Å.

The FWHM of the film rocking curve (figure 3.27) is 0.020°, so the crystallinity is excellent.

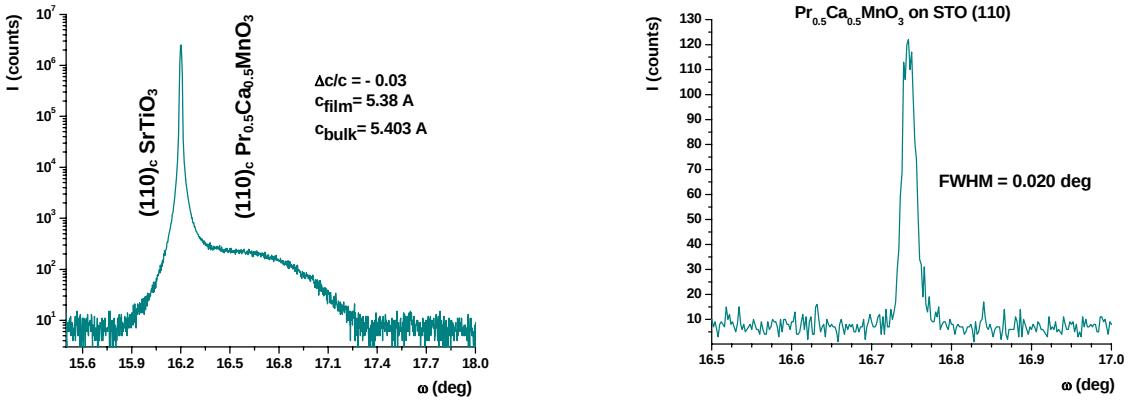

Figure 3.27. ω/2θ scan and film rocking curve of the (110) reflection.

The figure 3.28 shows the RSMs around the (110) symmetric and (22-2) asymmetric reflections, respectively. In particular the (22-2) map shows that the film maximum is aligned in H with the $SrTiO_3$ one, indicating that the film is fully strained.

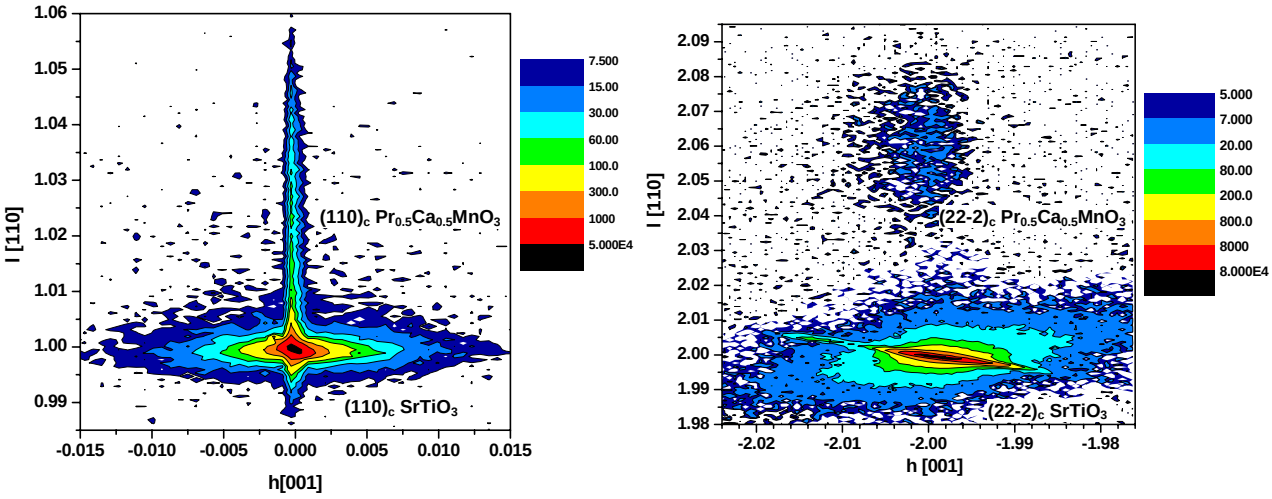

Figure 3.28. RSMs around $(110)_c$ symmetric reflection (on the left) and $(22\text{-}2)_c$ asymmetric reflection (on the right).

Therefore, for $Pr_{0.5}Ca_{0.5}MnO_3$ film the measurements demonstrate an epitaxial growth on $SrTiO_3$ (110), undergoing in-plane tensile strain and therefore with the in-plane lattice parameters matched with the substrate ones, and with the out-of-plane parameter c shorter than the bulk one. I can conclude that $Pr_{0.7}Ca_{0.3}MnO_3$ film is fully strained with a = 5.522 ± 0.001 Å, b = 7.810 ± 0.001 Å, and c = 5.380 ± 0.001 Å lattice parameters in the orthorhombic Pnma space group, to be compared with the bulk ones a = 5.403 Å, b = 7.612 Å, c = 5.395 Å.

3.5.2. Magnetic characterization.

In the following I present the magnetization measurements on $Pr_{0.5}Ca_{0.5}MnO_3$ grown on $SrTiO_3$ (110). All the magnetic measurements have been performed

applying the magnetic field parallel to a side of the sample, along the b_{orth} axis in-plane direction.

The temperature dependence of the spontaneous magnetic moment at H = 0 and the M_{FC} and M_{ZFC} of $Pr_{0.5}Ca_{0.5}MnO_3$ were measured for different field strengths (25 Oe, 50 Oe, 100 Oe, 250 Oe, 500 Oe, 1 kOe, 2.5 kOe and 5 kOe) in the range $4.2 \leq T \leq 380$ K.

There is not experimental evidence of any long range order at zero magnetic field (figure 3.29).

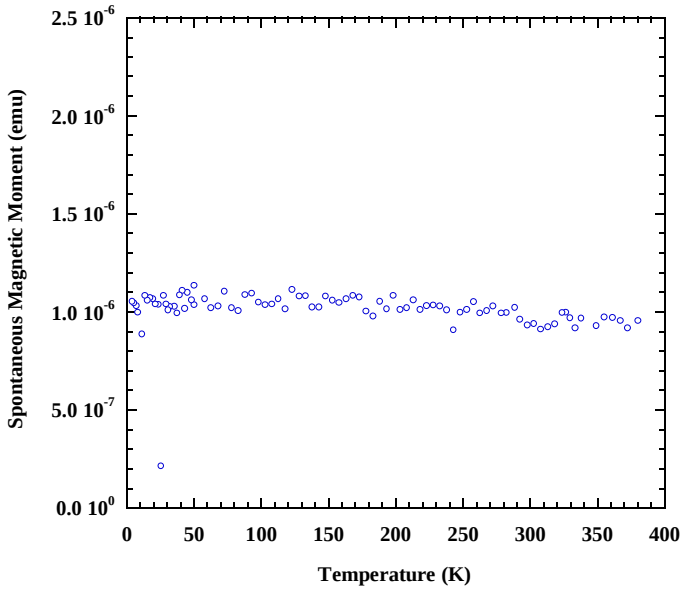

Figure 3.29. Spontaneous magnetic moment versus temperature.

Examples of the magnetic behavior observed are given in figure 3.30, which reports chosen M_{FC} and M_{ZFC} curves corresponding to the fields of 50 Oe, 250 Oe, 2500 Oe, and 5000 Oe in the measured range of temperature.

In the low temperature range, the magnetic moment results dependent on the sample thermal history, as for $Pr_{0.7}Ca_{0.3}MnO_3$ grown on $SrTiO_3$ (001) (par. 3.2.3). A bifurcation between M_{ZFC} and M_{FC} is apparent at T_{irr}, , indicating the onset of a freezing process, in addition, the presence of a maximum in M_{ZFC} at the temperature T_{max} is observed at low field (50 Oe), that broadens at higher fields, while T_{max} shifts to lower values together with the corresponding T_{irr}. The T_{max} and T_{irr} field dependences, showed in figure 3.31 (at fields of 50

Oe, 100 Oe, 250 Oe, 500 Oe, 1 kOe, 2.5 kOe), correspond also for this film to de Almeida-Thouless (AT) line given by $H_{AT}(T)/\Delta J \propto (1-T/T_{irr})^{3/2}$ [101].

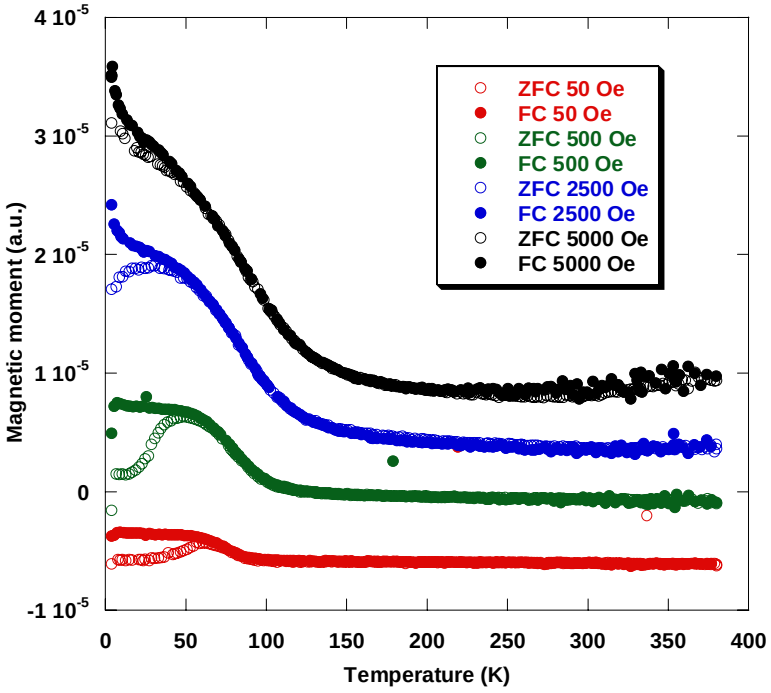

Figure 3.30. M_{ZFC} and M_{FC} curves obtained with static magnetic fields for $Pr_{0.5}Ca_{0.5}MnO_3$ film grown on $SrTiO_3$ (110).

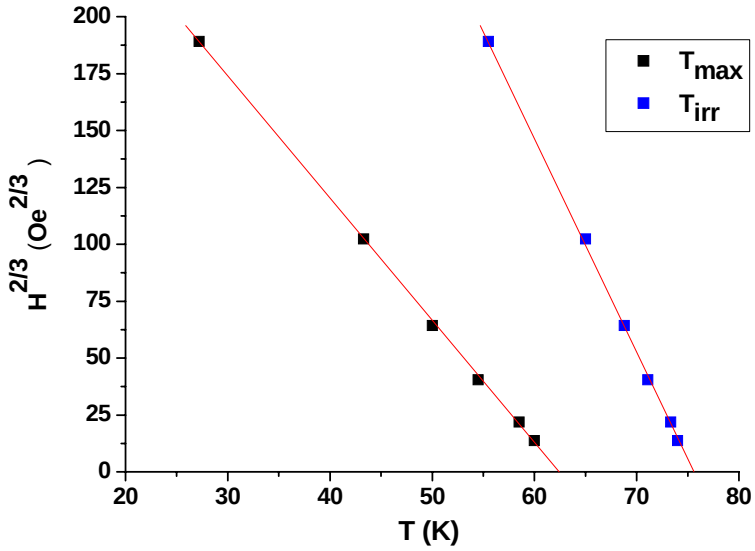

Figure 3.31. Field dependence of the transition temperatures T_{irr} as determined by M_{ZFC} and M_{FC} curves (blue points), and of T_{max} as determined by M_{ZFC} (black points), showing the De Almeida-Thouless lines for $Pr_{0.5}Ca_{0.5}MnO_3$ film grown on $SrTiO_3$ (110).

The linear extrapolation of the AT lines of T_{max} at H = 0 (shown in the figure 3.2) provides a way of determining the spin-freezing transition temperature T_f (as already discuss in par. 3.2.3), that in this case results equal to 62 ± 2 K.

Another important piece of evidence of the spin-glass like behaviour is the time dependence of the remanent magnetization below T_f when the external magnetic field is turned off after crossing T_f. Also the remanent magnetization below T_f relaxes following the typically stretched exponential function of the time t,

$$M(t) = M(0)\ exp\ [a\ t^{(1-b)}]$$

where $M(0)$ is the magnetization value at the beginning of the relaxing process.

The time dependence of remanent magnetization of the sample cooled in a field of 500 Oe was recorded immediately after the field was turned off at 50 K. I present the experimental curve and the fitting in figure 3.32.

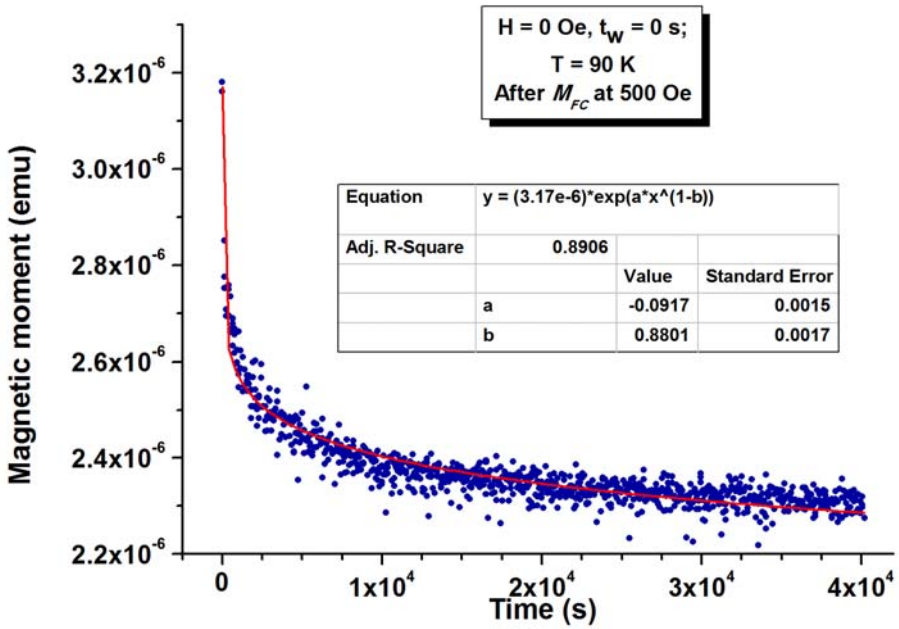

Figure 3.32. $M(t)$ isothermal relaxation curve measured after M_{FC} down to 50 K, in an external field of 500 Oe, in blue, the fitting has been reported in red.

Thus, these results confirm the appearance of a spin glass (SG) state at low temperature in $Pr_{0.5}Ca_{0.5}MnO_3$ grown on $SrTiO_3$ (110).

In polycrystalline $Pr_{0.5}Ca_{0.5}MnO_3$ Cao *et al*. [108] found a ground state formed by FM clusters, in a background of FM and CE-type FM matrix competing interactions. The competing interaction freeze some spin and form a cluster RSG, which shows the AFM cluster nature of RSG.

On the contrary, in our case we do not find any trace of long range magnetic order. Therefore, the effect of the tensile strain, induced by the epitaxial growth of $Pr_{0.5}Ca_{0.5}MnO_3$ on $SrTiO_3$ (110), is to destabilize the CO/AFM phase with a probable formation of ferromagnetic domains. One can easily consider that the existence of different kinds of magnetic domains (that do not give a long range order) are at the origin of the magnetic frustration, that turns out in the spin-glass like state.

Several studies performed on manganites have revealed that for these materials the antiferro-ferromagnetic competition favours a spin-glass like state at low temperature. This has been showed for $Pr_{1-x}Ca_xMnO_3$ with $0.25 \leq x < 0.50$, in the bulk form, but not for 0.5 composition, that Maignan *et al*. [109] found to be perfectly charge ordered antiferromagnet. Also $(Tb/La)_{2/3}Ca_{1/3}MnO_3$ [110] and $Eu_{0.58}Sr_{0.42}MnO_3$ exhibit both a spin-freezing temperature $T_{SG} \sim 45$ K [111], and the $Pr_{0.7}(Ca,Sr)_{0.3}MnO_3$ series, where a rather similar magnetic behavior was obtained with $T_{SG} \sim 95$K [112], too.

3.6. Summary.

In this chapter I have discuss the results of the characterization of chosen $La_{0.7}Sr_{0.3}MnO_3$ and $Pr_{1-x}Ca_xMnO_3$ films. To sum up the following general properties have been found, all films resulting epitaxial, with the correct stoichiometry and with an excellent crystal quality.

The $La_{0.7}Sr_{0.3}MnO_3$ films deposited on $SrTiO_3$ (001) have a paramagnetic/ferromagnetic transition at about 320 K.

I have demonstrated that the magnetism of $Pr_{1-x}Ca_xMnO_3$ films are strongly influenced by the strain, finding that there is a big difference between the two chosen growth orientations (001) and (110).

In particular, the $Pr_{0.7}Ca_{0.3}MnO_3$ films deposited on $SrTiO_3$ (001) have a reentrant spin glass behaviour with a paramagnetic/ferromagnetic transition at about 120 K and a transition to a glass state at lower temperature (notable result for the fundamental physics), while deposited on $SrTiO_3$ (110) is a ferromagnet with a pure paramagnetic/ferromagnetic transition at about 130 K (significant result in view of future device applications).

Furthermore, the $Pr_{0.5}Ca_{0.5}MnO_3$ films deposited on $SrTiO_3$ (001) are paramagnetic with only weak signs of the charge ordered/antiferromagnetic phase present in the bulk compound, while deposited on $SrTiO_3$ (110) are spin glasses with freezing temperature of about 60 K.

CHAPTER 4

Structural and transport characterization of epitaxial multilayers of manganites.

$La_{0.7}Sr_{0.3}MnO_3/SrTiO_3$ and $Pr_{0.7}Ca_{0.3}MnO_3/La_{0.7}Sr_{0.3}MnO_3$ multilayers have been deposited onto $SrTiO_3$ single crystal substrate (001) oriented, using a RHEED-assisted laser ablation technique in the MODA system (as described in paragraph 2.3), at the CNR-INFM Coherentia laboratory in Naples. Thanks to the RHEED control, it is possible a precise control of the layer sequence, which is extremely important for the realization of devices.

In this chapter I will report and discuss on structural and magnetic characterization performed on two decalayers constituted by alternate layers of five unit cells (in pseudocubic approximation) of $La_{0.7}Sr_{0.3}MnO_3$ intercalated with $SrTiO_3$ or with $Pr_{0.7}Ca_{0.3}MnO_3$, respectively. The characterization of $La_{0.7}Sr_{0.3}MnO_3/SrTiO_3$ and $Pr_{0.7}Ca_{0.3}MnO_3/La_{0.7}Sr_{0.3}MnO_3$ multilayers has been performed by means of ex-situ high resolution x-ray diffraction, high resolution transmission electron microscopy and SQUID magnetometry. The discussion will be focalized on the induced strain at the interfaces and on the effect of the spacer (the diamagnetic $SrTiO_3$ or the RSG $Pr_{0.7}Ca_{0.3}MnO_3$) on the magnetic properties of $La_{0.7}Sr_{0.3}MnO_3$ multilayers.

4.1. Characterization of $La_{0.7}Sr_{0.3}MnO_3/SrTiO_3$ multilayer grown on $SrTiO_3$ (001) oriented.

4.1.1. Structural characterization.

4.1.1.1. High resolution x-ray diffraction.

In the following I present the *ω/2θ*, *ω*-scan (rocking curve), high resolution reciprocal space maps (RSM) of the decalayer constituted by alternate layers of five unit cells (in pseudocubic approximation) of $La_{0.7}Sr_{0.3}MnO_3$ and $SrTiO_3$ grown on $SrTiO_3$ (001).

From the *ω/2θ* scan of the (002) cubic reflection (figure 4.1) I have calculated the out-of-plain medium lattice parameter c_{multi} = 3.887 ± 0.001 Å,

that is an intermediate value between c_{LSMO} = 3.854 Å and c_{STO} = 3.905 Å. By the fitting with Leptos software [98] I have calculated the thickness of each single layer (that, within the error bar of such a evaluation, corresponds to five cells of thickness) and so the total multilayer thickness that results equal to 38 nm. In figure 4.1 the experimental *ω/2θ* curve in green and the calculated curve in red are showed.

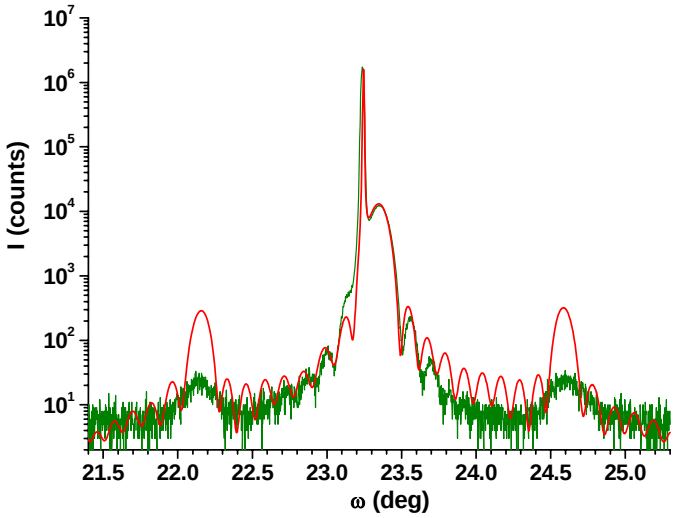

Figure 4.1. *ω/2θ* scan of the $(002)_c$ reflection of the $La_{0.7}Sr_{0.3}MnO_3/SrTiO_3$ multilayer.

The full-width at half-maximum (FWHM) of the $La_{0.7}Sr_{0.3}MnO_3/SrTiO_3$ multilayer rocking curve (figure 4.2) is 0.020°, indicating the excellent crystal quality of the sample.

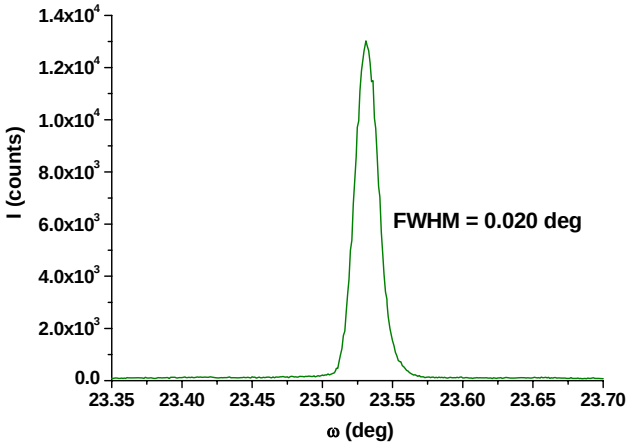

Figure 4.2. Rocking curve of the $(002)_c$ reflection of the $La_{0.7}Sr_{0.3}MnO_3/SrTiO_3$ multilayer.

The figure 4.3 shows the RSMs around the $(002)_c$ symmetric and $(0\text{-}13)_c$ asymmetric reflections, respectively. In particular the $(0\text{-}13)_c$ map shows only a maximum for $La_{0.7}Sr_{0.3}MnO_3$ that is aligned in H with the $SrTiO_3$ one, indicating that the multilayer is fully strained in the growing plane.

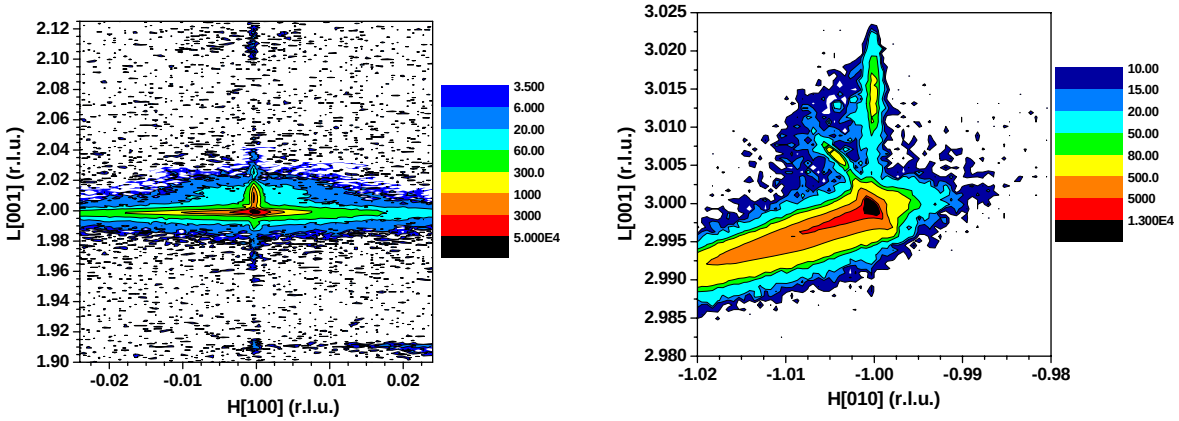

Figure 4.3. RSMs around $(002)_c$ symmetric reflection and $(0\text{-}13)_c$ asymmetric reflection of the $La_{0.7}Sr_{0.3}MnO_3/SrTiO_3$ multilayer.

4.1.1.2. High resolution scanning transmission electron microscopy.

High resolution scanning transmission electron microscopy measurements were performed on $La_{0.7}Sr_{0.3}MnO_3/SrTiO_3$ multilayer grown onto $SrTiO_3$ (001), by Claudia Cantoni at Oak Ridge National Laboratory in Eastern Tennessee (U.S), using an aberration corrected 100 kV scanning transmission electron microscope (STEM) with a cold field emission electron gun to acquire atomic resolution images.

Figure 4.4 shows a high angular annular dark field (HAADF) Z-contrast STEM image from an ion milled longitudinal cross-section of a $La_{0.7}Sr_{0.3}MnO_3/SrTiO_3$ multilayer grown onto $SrTiO_3$ (001) oriented. Z-contrast imaging uses electrons scattered from a thin (~ 20 nm) sample to form an image of the atoms. Because the scattered intensity depends on the atomic number (Z) of the chemical element being probed, the image intensity provides a means to distinguish the atoms with different atomic number. Z-contrast imaging is particularly suited to the viewing of interfaces, grain boundaries, and defects in materials that cannot be analyzed using indirect measurements. Such

measurement on the $La_{0.7}Sr_{0.3}MnO_3/SrTiO_3$ multilayer grown onto $SrTiO_3$ (001) (figure 4.4) shows a regular periodicity with alternate brighter $La_{0.7}Sr_{0.3}MnO_3$ (with higher Z) and darker $SrTiO_3$ (with lower Z) layers. The interfaces between each different layer are clearly visible. Figure 4.4 shows also a growth with no sign of relaxation of the multilayer structure, in agreement with the HRXRD measurements. Moreover, neither dislocations nor stacking faults were found.

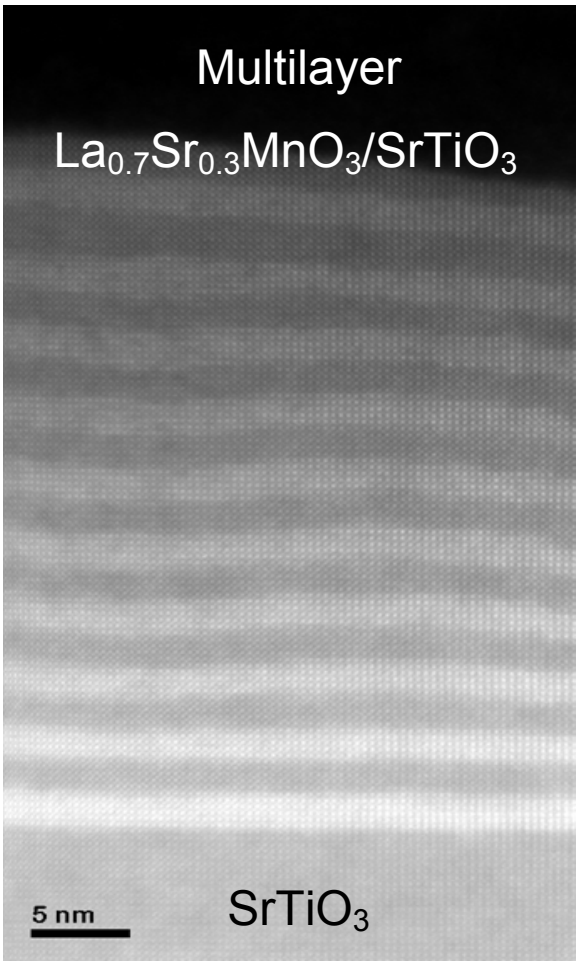

Figure 4.4. HAADF Z-contrast STEM image from a longitudinal cross-section of $La_{0.7}Sr_{0.3}MnO_3/SrTiO_3$ multilayer grown onto $SrTiO_3$ (001), the bright layers being $La_{0.7}Sr_{0.3}MnO_3$ and the darker $SrTiO_3$.

4.1.2. Magnetic characterization.

In the following I present the magnetization measurements of $La_{0.7}Sr_{0.3}MnO_3/SrTiO_3$ multilayer grown on $SrTiO_3$ (001). All the magnetic

measurements have been performed by applying the magnetic field parallel to a side of the sample, along the [100] in-plane direction.

The temperature dependence of the spontaneous magnetic moment and the M_{FC} and M_{ZFC} versus temperature were measured for 5 Oe, 25 Oe, 75 Oe, 150 Oe, 250 Oe, 500 Oe and 1000 Oe magnetic fields, in the range $4.2 \leq T \leq 380$ K.

Examples of the observed behavior are given in figure 4.5, which reports some selected M_{FC} and M_{ZFC} curves corresponding to the fields of 5 Oe, and 500 Oe in the measured range of temperature.

There is experimental evidence of a PM/FM transition at 180 ± 1 K (see figure 4.5); the T_C is determined at zero magnetic field.

A second transition is visible at low field at around 105 K. I want to point out that at 105 K the $SrTiO_3$ undergoes a ferroelastic transition from the cubic to the tetragonal structure. So I can attribute the second transition to the effect of the diamagnetic $SrTiO_3$ ferroelastic transition on the $La_{0.7}Sr_{0.3}MnO_3$ ferromagnetic layers.

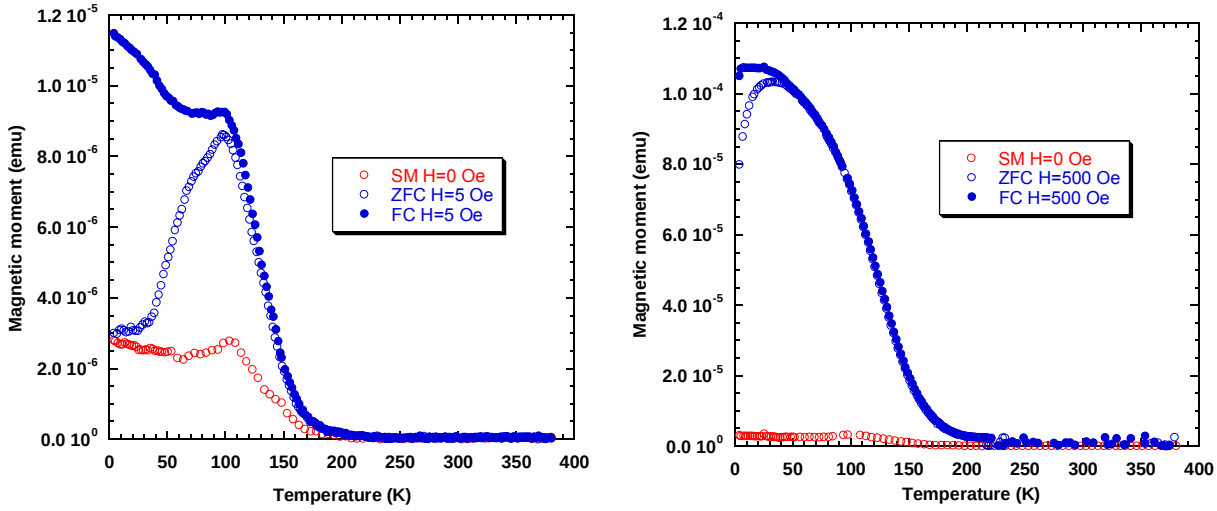

Figure 4.5. Spontaneous magnetic moment, M_{ZFC} and M_{FC} curves versus temperature, obtained with a static magnetic field of 5 Oe (on the left) and 500 Oe (on the right) for $La_{0.7}Sr_{0.3}MnO_3/SrTiO_3$ multilayer grown on $SrTiO_3$ (001).

Besides, in the low temperature range (below the PM/FM transition temperature), magnetization results dependent on the sample thermal history:

a bifurcation between M_{ZFC} and M_{FC} is apparent at an irreversibility temperature T_{irr}, which is the temperature value at which the irreversible magnetic moment, defined as $\Delta M = M_{FC} - M_{ZFC}$, becomes different from zero, indicating the onset of a freezing process. In addition, the presence of a maximum in M_{ZFC} at the temperature T_{max} is observed at low field (5 Oe), that broadens at higher fields, while T_{max} shifts to lower values (500 Oe). The T_{irr} field dependence is showed in figure 4.6 (at fields of 5 Oe, 25 Oe, 75 Oe, 150 Oe, 250 Oe, 500 Oe, 1 kOe), that corresponds to de Almeida-Thouless (AT) line given by $H_{AT}(T)/\Delta J \propto (1-T/T_{irr})^{3/2}$ [101].

The linear extrapolation of the AT lines of T_{irr} at $H = 0$ (shown in the figure 4.6) provides a way of determining the temperature, at which the spins start to freeze, that in this case results equal to 147 ± 2 K.

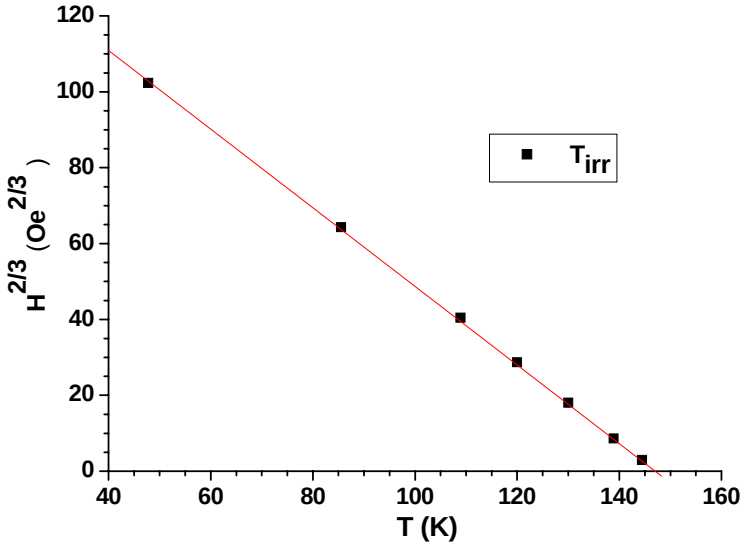

Figure 4.6. Field dependence of the transition temperatures T_{irr} as determined by M_{ZFC} and M_{FC} curves, showing the De Almeida-Thouless line for $La_{0.7}Sr_{0.3}MnO_3/SrTiO_3$ multilayer grown on $SrTiO_3$ (001).

The behaviour observed is typical of a spin glass material. The irreversible magnetic behaviour of $La_{0.7}Sr_{0.3}MnO_3/SrTiO_3$ multilayer grown on $SrTiO_3$ (001) can be ascribed to a re-entrant spin glass (RSG), because it is also possible to identify a Curie temperature T_C above both T_{max} and T_{irr}. As described in par. 3.2.3, a RSG has to be considered a mixed phase of a long range ferromagnetic

phase and a SG phase. I propose to relate the observed magnetic behaviour to the weakening of the double exchange of $La_{0.7}Sr_{0.3}MnO_3$ due to the diamagnetic $SrTiO_3$ spacer.

In figure 4.7 the hysteresis cycle measured at 5 K is reported. The coercitive field is of 330 ± 5 Oe, so I can classify the $La_{0.7}Sr_{0.3}MnO_3/SrTiO_3$ multilayer grown on $SrTiO_3$ (001) as a hard ferromagnetic material.

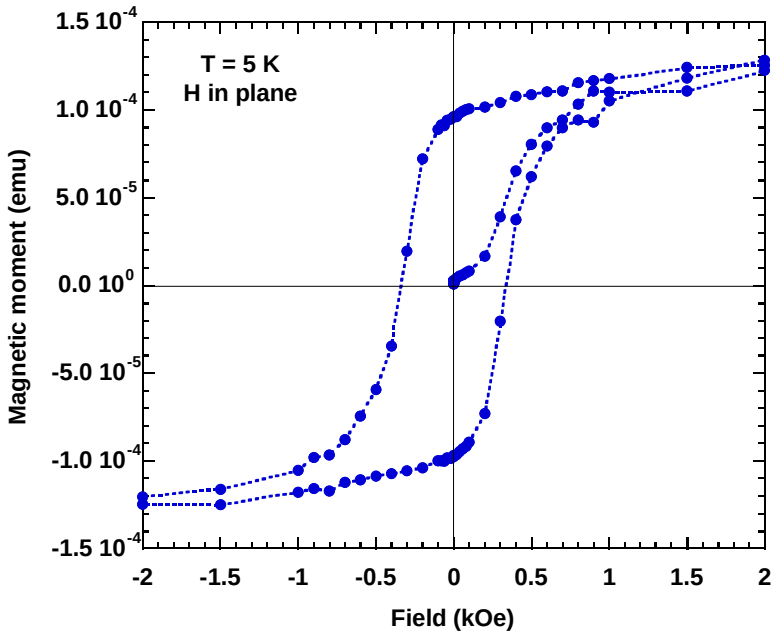

Figure 4.7. Hysteresis cycle versus magnetic field measured at 5 K, for $La_{0.7}Sr_{0.3}MnO_3/SrTiO_3$ multilayer grown on $SrTiO_3$ (001).

One of the possible origins of such described magnetic behaviour can be ascribed to the formation of a dead layer near the $La_{0.7}Sr_{0.3}MnO_3/SrTiO_3$ interfaces, in which the ferromagnetism of $La_{0.7}Sr_{0.3}MnO_3$ is locally deteriorated. As a physical model for the formation of the dead layer, it has been proposed that the charge transfer at the interface induces a hole-overdoped $La_{0.7}Sr_{0.3}MnO_3$ layer which is dominated by the antiferromagnetic spin canting [113, 114]. The competition between this originated antiferromagnetism at the interfaces and the ferromagnetism of $La_{0.7}Sr_{0.3}MnO_3$ layers can originate and explain the observed reentrant spin glass behaviour.

4.2. Characterization of $Pr_{0.7}Ca_{0.3}MnO_3/La_{0.7}Sr_{0.3}MnO_3$ multilayer grown on $SrTiO_3$ (001) oriented.

4.2.1. Structural characterization.

4.2.1.1. High resolution x-ray diffraction.

The structural characterization of the decalayer $Pr_{0.7}Ca_{0.3}MnO_3/La_{0.7}Sr_{0.3}MnO_3$ constituted by alternate layers of five unit cells (in pseudocubic approximation) of $Pr_{0.7}Ca_{0.3}MnO_3$ and $La_{0.7}Sr_{0.3}MnO_3$ grown on $SrTiO_3$ (001) was performed by HRXRD measurements as above described (in par. 2.1.1). In the following I present the reflectivity curve, *ω/2θ*, *ω*-scan (rocking curve), and high resolution reciprocal space maps (RSM).

From the *ω/2θ* scan of the (002) cubic reflection (figure 4.8) I have calculated the out-of-plain medium lattice parameter c_{multi} = 3.833 ± 0.001 Å, that is an intermediate value between c_{LSMO} = 3.854 Å and c_{PCMO} = 3.811 Å, calculated above for the films grown on $SrTiO_3$ (001). By the fitting with Leptos software [98] I have calculated the thickness of each single layer (the mean value being 1.9 nm) and so the total one that is equal to 37 nm. In figure 4.8 the experimental *ω/2θ* curve in blue and the calculated curve in red are showed.

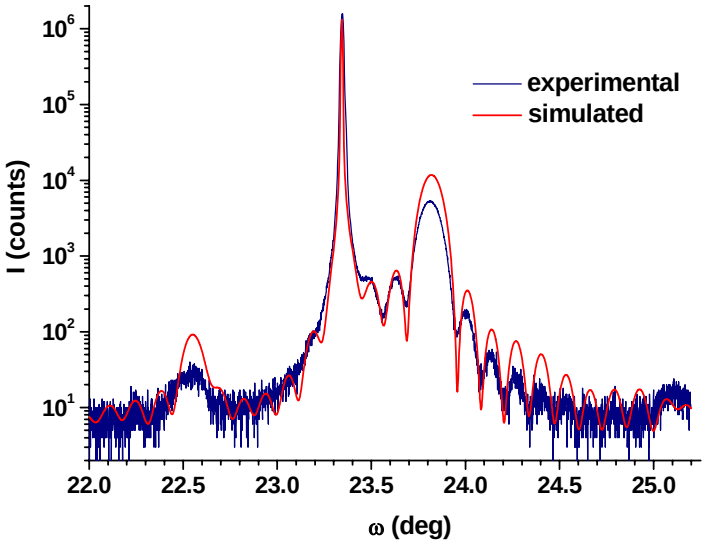

Figure 4.8. *ω/2θ* scan of the $(002)_c$ reflection of $Pr_{0.7}Ca_{0.3}MnO_3/La_{0.7}Sr_{0.3}MnO_3$ multilayer.

The full-width at half-maximum (FWHM) of the sample rocking curve (figure 4.9) is 0.029°, indicating a good crystal quality of the multilayer.

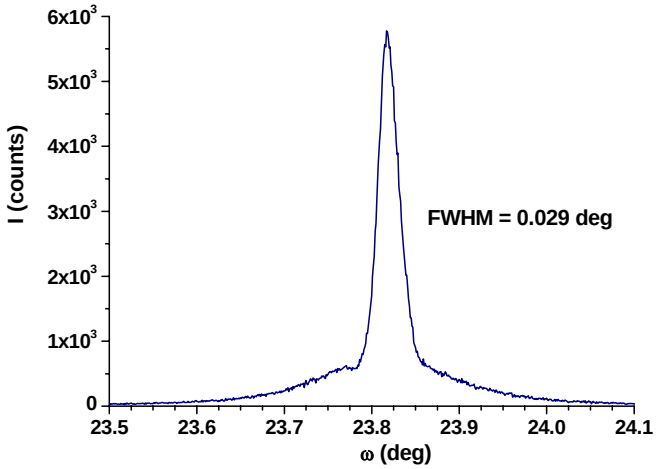

Figure 4.9. $Pr_{0.7}Ca_{0.3}MnO_3/La_{0.7}Sr_{0.3}MnO_3$ multilayer rocking curve of the $(002)_c$ reflection.

The figures 4.10 and 4.11 show the RSMs around the $(002)_c$ symmetric, $(-130)_c$ and $(-1-13)_c$ asymmetric reflections. In particular the $(-130)_c$ and $(-1-13)_c$ maps show only a maximum for the system $Pr_{0.7}Ca_{0.3}MnO_3/La_{0.7}Sr_{0.3}MnO_3$ that is aligned in H with the $SrTiO_3$ one, indicating that the multilayer is fully strained.

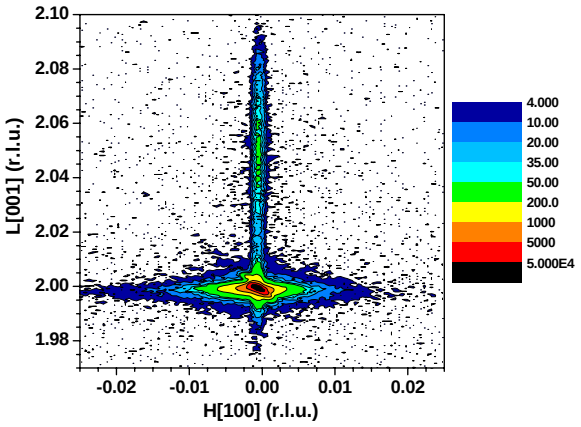

Figure 4.10. RSM around $(002)_c$ symmetric reflection of $Pr_{0.7}Ca_{0.3}MnO_3/La_{0.7}Sr_{0.3}MnO_3$ multilayer.

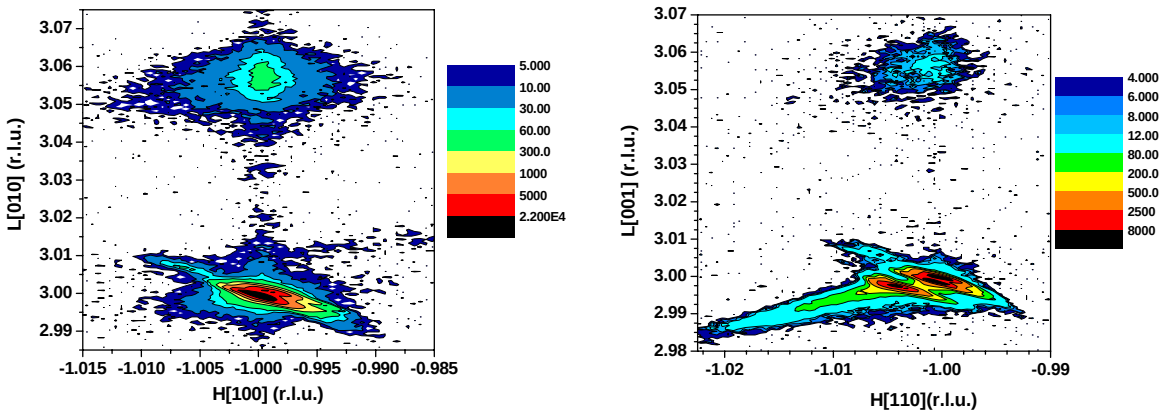

Figure 4.11. RSMs around $(-130)_c$ and $(-1-13)_c$ asymmetric reflections of $Pr_{0.7}Ca_{0.3}MnO_3/La_{0.7}Sr_{0.3}MnO_3$ multilayer.

4.2.1.2. High resolution scanning transmission electron microscopy and partially resolved EEL spectroscopy.

High resolution transmission electron microscopy measurements were performed on $Pr_{0.7}Ca_{0.3}MnO_3/La_{0.7}Sr_{0.3}MnO_3$ multilayer grown on $SrTiO_3$ (001), by Claudia Cantoni, at Oak Ridge National Laboratory in Eastern Tennessee (U.S). The measurements were performed using an aberration corrected 100 kV scanning transmission electron microscope (STEM) equipped with a Nion aberration corrector and an Enfina electron energy-loss (EEL) spectrometer to simultaneously acquire atomic resolution images, and spatially-resolved EEL spectra with sub-nanometre spatial resolution.

Figure 4.12 shows a high angular annular dark field HAADF Z-contrast STEM image from an ion milled longitudinal cross-section of a $Pr_{0.7}Ca_{0.3}MnO_3/La_{0.7}Sr_{0.3}MnO_3$ multilayer grown onto $SrTiO_3$ (001) oriented. The technique has been described in par. 4.1.1.2. Bright atoms in figure 4.12 are A-site atoms, of the ABO_3 perovskite structures, the dashed line indicates the interface section between the substrate and the multilayer. The image proves the overall excellent crystal quality.

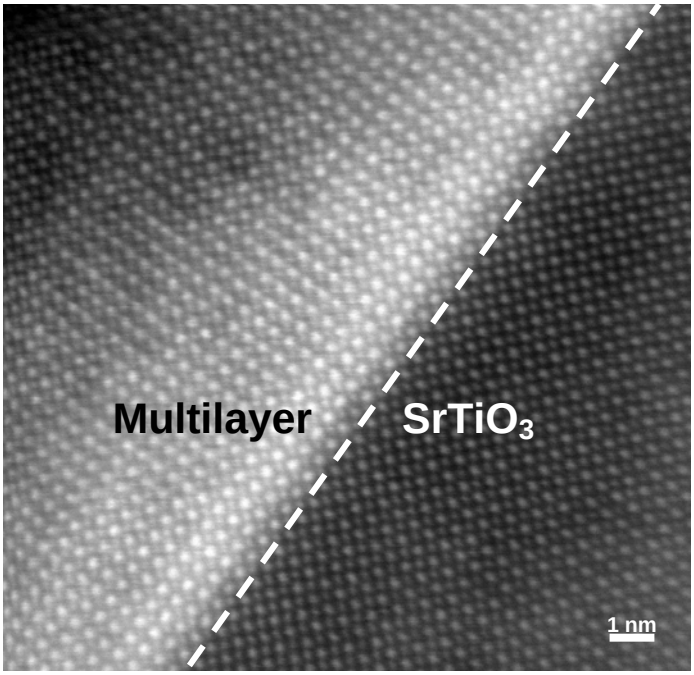

Figure 4.12. Z-contrast HAADF STEM image from a cross-section of $Pr_{0.7}Ca_{0.3}MnO_3/La_{0.7}Sr_{0.3}MnO_3$ multilayer grown onto $SrTiO_3$ (001).

The EELS technique is sensitive to the local structure, chemical composition, oxidation of the elements and bonding. The EELS spectra were acquired along the green line shown in the Z-contrast image showed in figure 4.13. Each spectrum is then processed to extract the integrated intensity of each element, which is finally plotted as function of position (see figure 4.13). Each data point for Ca, Ti, Mn, La, and Pr in the graph is extracted from a single EELS spectrum.

The Pr intensity is compared to the annular dark field (ADF) image intensity, obtained in the same scan in figure 4.13. The EELS signal from Pr shows that each layer is made by 5 unit cell with a thickness of 1.95 nm, the same periodicity appearing in the ADF signal.

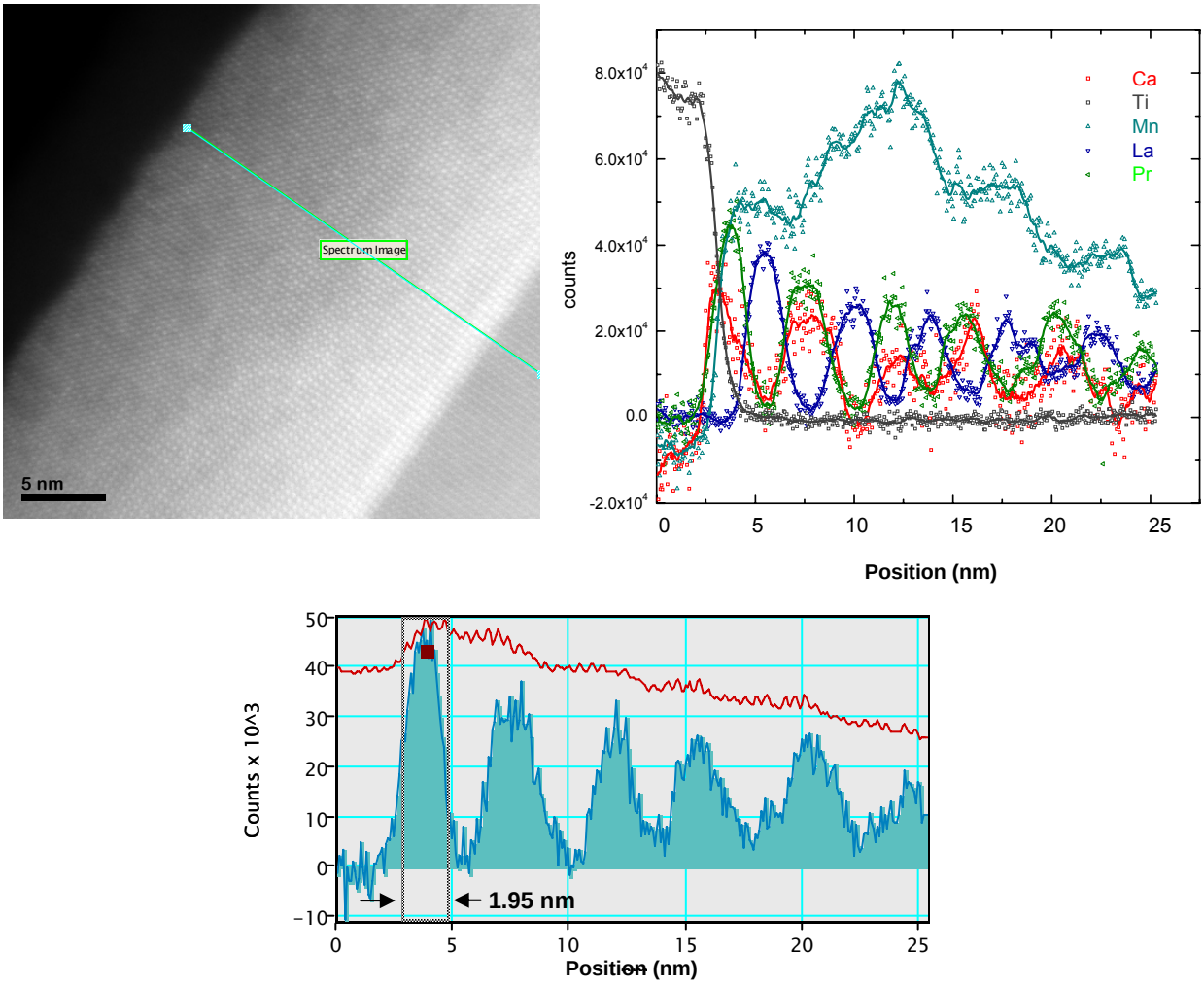

Figure 4.13. HREM analysis of $Pr_{0.7}Ca_{0.3}MnO_3/La_{0.7}Sr_{0.3}MnO_3$ multilayer grown onto $SrTiO_3$ (001).

Atomic scale elemental maps can also be obtained from an EEL spectrum image. In this case a EEL spectrum is acquired at each point of a fine grid in the rectangle indicated in the image in figure 4.14. The spectra are then processed to extract the integrated intensities of the elements. The results of the analysis are reported in figure 4.14, where each pixel of the elemental images comes from an EEL spectrum. The atomic columns of La, Pr, Ca, Ti and Mn have been visualized as two-dimensional images.

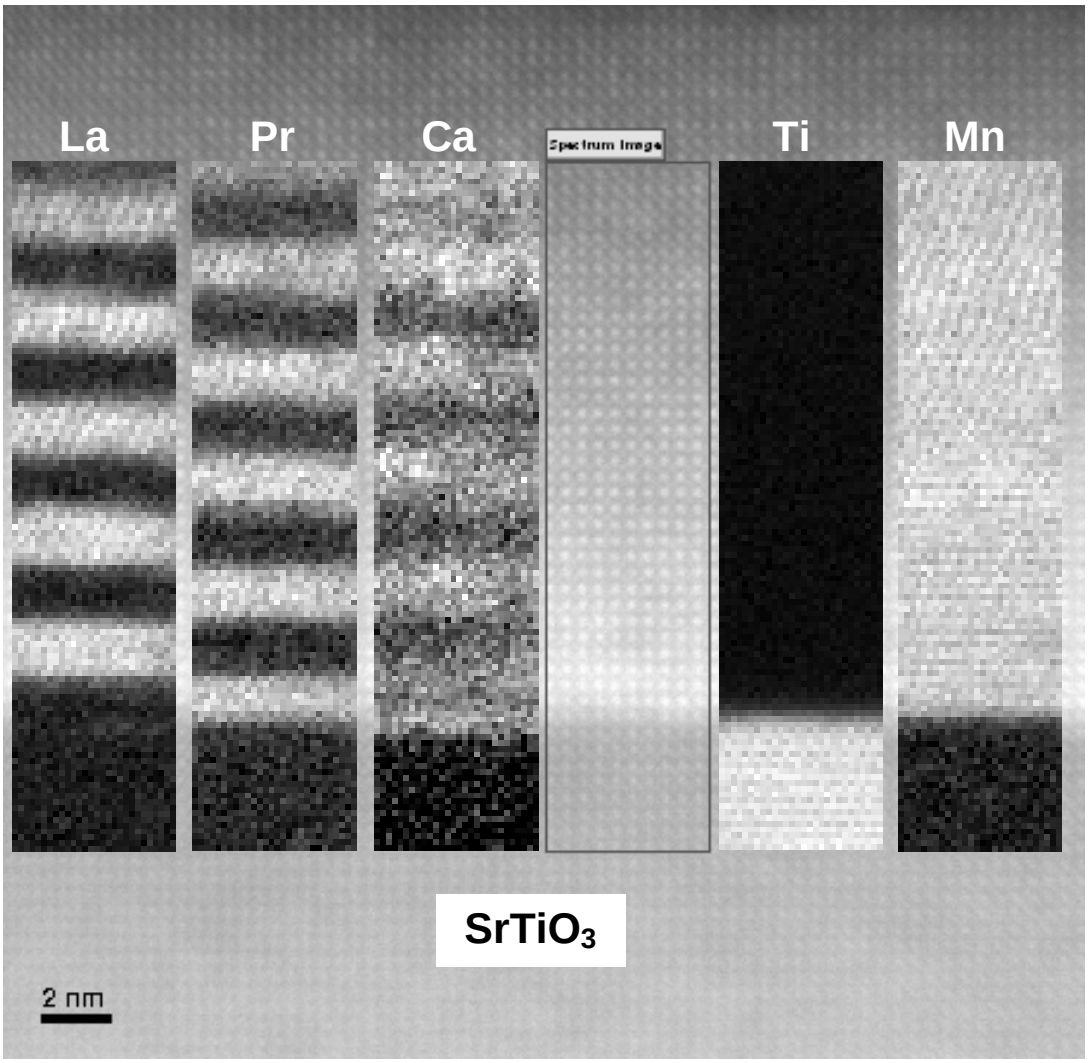

Figure 4.14. EELS maps of $Pr_{0.7}Ca_{0.3}MnO_3/La_{0.7}Sr_{0.3}MnO_3$ multilayer grown onto $SrTiO_3$ (001).

Therefore the EELS profiles and maps (figures 4.13 and 4.14) allow to chemically resolve the single elements. Such measurements and analysis confirm a regular epitaxial growth, with no sign of relaxation of the multilayer structure, in agreement with the HRXRD measurements. Moreover, neither dislocations nor stacking faults were found.

4.2.2. *Magnetic characterization.*

In the following I present the magnetization measurements of $Pr_{0.7}Ca_{0.3}MnO_3/La_{0.7}Sr_{0.3}MnO_3$ multilayer grown on $SrTiO_3$ (001). All the magnetic measurements have been performed by applying the magnetic field parallel to a side of the sample, along the [100] in-plane direction.

The temperature dependence of the spontaneous magnetic moment and the M_{FC} and M_{ZFC} versus temperature were measured for 50 Oe and 500 Oe magnetic fields, in the range $4.2 \leq T \leq 380$ K (see figures 4.15).

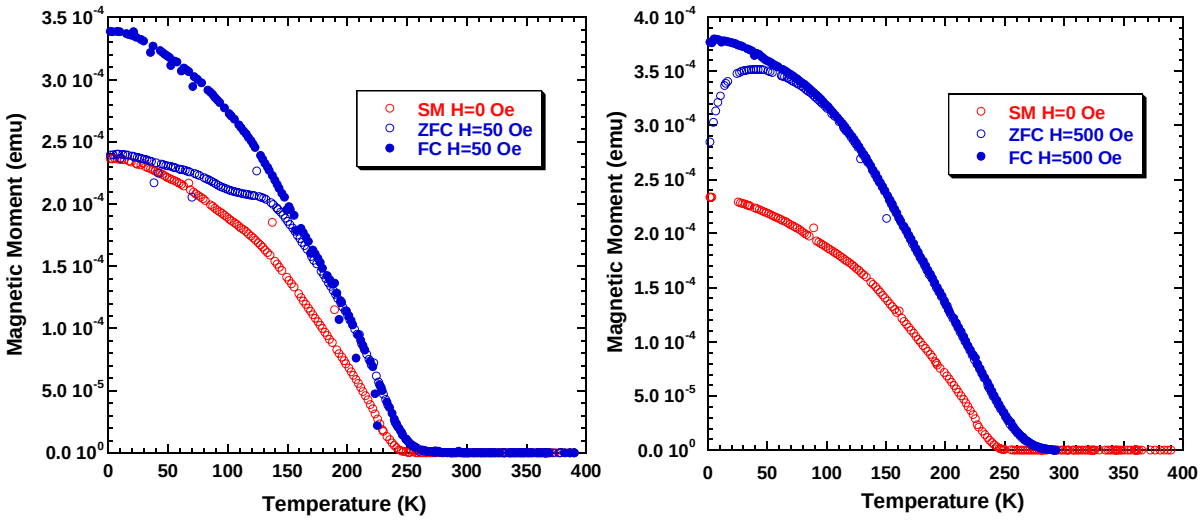

Figure 4.15. Spontaneous magnetic moment, M_{ZFC} and M_{FC} curves versus temperature, obtained with a static magnetic field of 50 Oe (on the left) and 500 Oe (on the right), applied along the [100] in-plain direction, for $Pr_{0.7}Ca_{0.3}MnO_3/La_{0.7}Sr_{0.3}MnO_3$ multilayer grown on $SrTiO_3$ (001).

There is experimental evidence of a PM/FM transition at 250 ± 1 K (see figure 4.15), the T_C being determinate at zero magnetic field. A second transition is visible at low magnetic field (50 Oe) at around 130 K in the M_{ZFC}, but nothing is observable in the M_{FC}. I want to point out that at around 120 K (determined at H=0 Oe) $Pr_{0.7}Ca_{0.3}MnO_3$ undergoes a paramagnetic/ferromagnetic transition. So I can attribute the first transition at higher temperature to the $La_{0.7}Sr_{0.3}MnO_3$ ferromagnetic layers, while the second

transition at lower temperature could be due to the effect of the $Pr_{0.7}Ca_{0.3}MnO_3$ layers ferromagnetic transition.

M_{ZFC} and M_{FC} curves were also measured applying the magnetic fields of 100 Oe along the [001] out-of-plain direction of the sample (see figure 4.16) in order to exclude the presence of anisotropy. In this case both the two transition are present in the M_{FC} curve. Therefore the [001] direction results the magnetic hard axis for the $La_{0.7}Sr_{0.3}MnO_3$ that has its paramagnetic/ferromagnetic transition at 250 K, and the easy axis for the $Pr_{0.7}Ca_{0.3}MnO_3$, that has its transition at around 130 K. Otherwise the [100] in-plane direction results the magnetic easy axis for $La_{0.7}Sr_{0.3}MnO_3$ and the hard one for $Pr_{0.7}Ca_{0.3}MnO_3$.

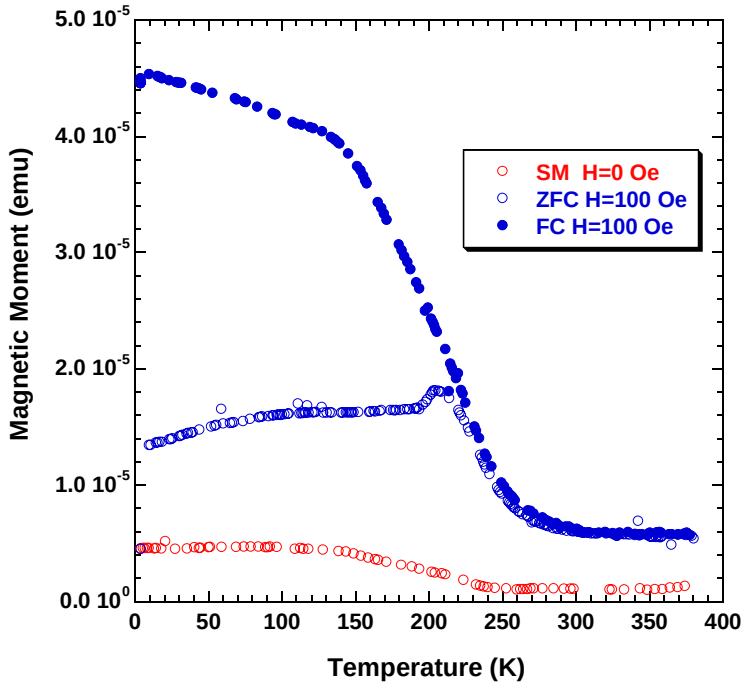

Figure 4.16. Spontaneous magnetic moment, M_{ZFC} and M_{FC} curves versus temperature, obtained with a static magnetic field of 100 Oe, applied along the [001] out-of-plain direction, for $Pr_{0.7}Ca_{0.3}MnO_3/La_{0.7}Sr_{0.3}MnO_3$ multilayer grown on $SrTiO_3$ (001).

In figure 4.17 the hysteresis cycle measured at 5 K, with the field applied in the [100] in plane direction, is reported. The coercitive field is of 639 ± 5 Oe, so I can classify the $Pr_{0.7}Ca_{0.3}MnO_3/La_{0.7}Sr_{0.3}MnO_3$ multilayer grown on $SrTiO_3$ (001) as a hard ferromagnetic material.

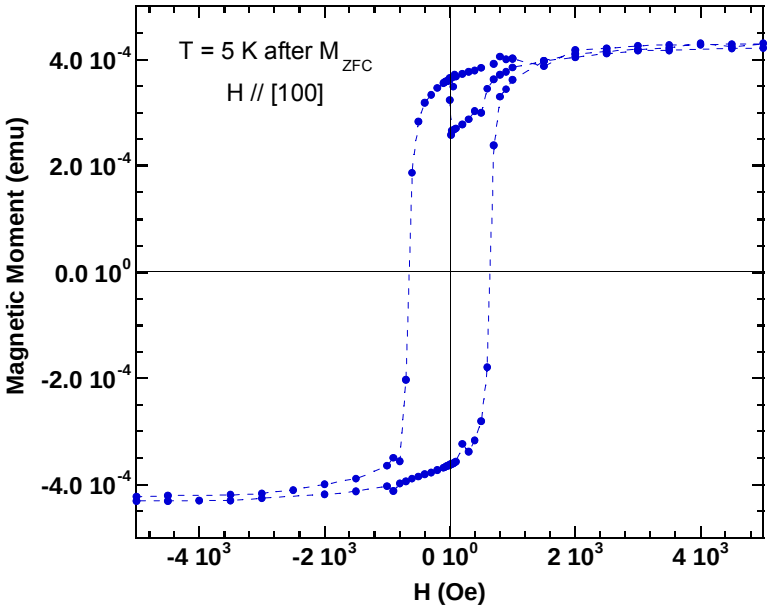

Figure 4.17. Hysteresis cycle versus magnetic field measured at 5 K, for $Pr_{0.7}Ca_{0.3}MnO_3/La_{0.7}Sr_{0.3}MnO_3$ multilayer grown on $SrTiO_3$ (001).

There are only a few reports on $Pr_{0.7}Ca_{0.3}MnO_3/La_{0.7}Sr_{0.3}MnO_3$ multilayers in the literature dealing with magnetic properties [115, 116, 117], but in those cases they consider $Pr_{0.7}Ca_{0.3}MnO_3/La_{0.7}Sr_{0.3}MnO_3$ as a FM-metal/AFM-insulator superlattice system, while in my case I have a FM-metal/FM-insulator multilayer. So it is not easy a comparison between my and their results. I can only compare the Curie temperature that Mukhopadhyay and Das [117] found at 200 K with our T_C at 250 K, that is evidently a better result, being a higher temperature.

4.3. Comparison between the $La_{0.7}Sr_{0.3}MnO_3/SrTiO_3$ and $Pr_{0.7}Ca_{0.3}MnO_3/La_{0.7}Sr_{0.3}MnO_3$ multilayers grown on $SrTiO_3$ (001) oriented.

The multilayers $La_{0.7}Sr_{0.3}MnO_3/SrTiO_3$ and $Pr_{0.7}Ca_{0.3}MnO_3/La_{0.7}Sr_{0.3}MnO_3$ grown onto $SrTiO_3$ (001) are deposited in the same conditions and with the same number of layers. The structural measurements have demonstrated that the growth is epitaxial and the crystalline structure is of excellent quality.

The magnetic properties of the $La_{0.7}Sr_{0.3}MnO_3/SrTiO_3$ and $Pr_{0.7}Ca_{0.3}MnO_3/La_{0.7}Sr_{0.3}MnO_3$ multilayers grown on $SrTiO_3$ (001) oriented are similar; both the two kind of multilayers have a paramagnetic/ferromagnetic transition (at around 180 K for $La_{0.7}Sr_{0.3}MnO_3/SrTiO_3$ and at around 250 K for $Pr_{0.7}Ca_{0.3}MnO_3/La_{0.7}Sr_{0.3}MnO_3$), and they can be classified as hard ferromagnet.

At low temperature (below the PM/FM transition) $Pr_{0.7}Ca_{0.3}MnO_3/La_{0.7}Sr_{0.3}MnO_3$ multilayer is a stable ferromagnets while the $La_{0.7}Sr_{0.3}MnO_3/SrTiO_3$ multilayer has a spin glass behaviour that makes it a reentrant spin glass.

Being the two multilayers identical in thickness of layers, the differences can be only attributed to the different spacers that in a case is $SrTiO_3$, and in the other $Pr_{0.7}Ca_{0.3}MnO_3$. A possible reason for the differences, to investigate further, is the fact that $SrTiO_3$ is a centrosymmetric crystal, while the $Pr_{0.7}Ca_{0.3}MnO_3$ is a polar crystal, with a non-centrosymmetric charge distribution and a net electric polarization [118]. Therefore I propose that while in $La_{0.7}Sr_{0.3}MnO_3/SrTiO_3$ multilayer there is the formation of a dead layer, due to the charge transfer at the interfaces (as described in par. 4.1.2), that inhibits a good ferromagnetic behaviour, in the case of $Pr_{0.7}Ca_{0.3}MnO_3/La_{0.7}Sr_{0.3}MnO_3$ multilayer, not being a charge transfer at the interfaces between the two manganites, there is a reduction of the dead layer, that gives as global result a stable ferromagnetic behaviour.

I want to point out that the reduction of the dead layer in $Pr_{0.7}Ca_{0.3}MnO_3/La_{0.7}Sr_{0.3}MnO_3$ multilayers is a relevant result, resulting functional in the design of new improved spin valves and magnetic tunnel junctions. To sum up I have demonstrate the potentiality of $La_{0.7}Sr_{0.3}MnO_3$ and $Pr_{1-x}Ca_xMnO_3$ in the field of the spintronics multilayer devices, in which they can find application, as a natural development of this work.

Conclusions

The aim of this thesis was to demonstrate that the perovskite manganites $La_{0.7}Sr_{0.3}MnO_3$ and $Pr_{1-x}Ca_xMnO_3$ are interesting candidates for the design and development of devices, with particular reference to spintronics devices based on multilayers, as spin valves and magnetic tunnel junctions.

To develop this idea, it was first necessary to achieve the full control of the growth of epitaxial $La_{0.7}Sr_{0.3}MnO_3$ and $Pr_{1-x}Ca_xMnO_3$ films. The analyzed films have been deposited using a RHEED-assisted laser ablation technique in the MODA system, at the CNR-INFM Coherentia laboratory, located at the Physics Department of the University of Naples "Federico II".

I characterized a very large set of samples, demonstrating that the used deposition technique can be successfully employed to get epitaxial growth, excellent quality samples, being the final results related to the level of control and of complexity of the used process. Moreover I demonstrated that, with an appropriate choice of the substrate, it is possible, by the application of strain, to influence the physical properties of the manganite thin films.

I have confirmed that the physical properties of the $La_{0.7}Sr_{0.3}MnO_3$ and $Pr_{1-x}Ca_xMnO_3$ films are strongly dependent on the structure and microstructure. In particular, the results presented in this thesis concern the characterization of the chemistry of the samples, by x-ray photoemission spectroscopy, the structure, by high resolution x-ray diffraction, with particular attention devoted to the investigation of epitaxy and strain, and also by high resolution transmission electron microscopy. The manganites films have showed very interesting magnetic properties, characterized by M(T) and M(H) measurements performed by SQUID magnetometry.

Finally, the structural and magnetic characterization of different complex epitaxial multilayers has been performed, demonstrating the potentiality of $La_{0.7}Sr_{0.3}MnO_3$ and $Pr_{1-x}Ca_xMnO_3$ in the fascinating field of the multilayer spintronics devices, related to the capability to take advantage of its peculiar physical properties.

In summary, the main findings of this work are the following.

(1) <u>$La_{0.7}Sr_{0.3}MnO_3$ and $Pr_{1-x}Ca_xMnO_3$ thin films.</u>

$La_{0.7}Sr_{0.3}MnO_3$ films deposited on $SrTiO_3$ (001) have a paramagnetic/ferromagnetic transition at about 320 K; $Pr_{0.7}Ca_{0.3}MnO_3$ films deposited on $SrTiO_3$ (001) have a reentrant spin glass behaviour with a paramagnetic/ferromagnetic transition at about 120 K and a transition to a glass state at lower temperature; $Pr_{0.7}Ca_{0.3}MnO_3$ films deposited on $SrTiO_3$ (110) are ferromagnetic with a paramagnetic/ferromagnetic transition at about 130 K. Furthermore, $Pr_{0.5}Ca_{0.5}MnO_3$ films deposited on $SrTiO_3$ (001) are essentially paramagnetic, while the $Pr_{0.5}Ca_{0.5}MnO_3$ films deposited on $SrTiO_3$ (110) are spin glasses with freezing temperature of about 60 K.

(2) $La_{0.7}Sr_{0.3}MnO_3/SrTiO_3$ and $Pr_{0.7}Ca_{0.3}MnO_3/La_{0.7}Sr_{0.3}MnO_3$ multilayers.

The magnetic properties of the $La_{0.7}Sr_{0.3}MnO_3/SrTiO_3$ and $Pr_{0.7}Ca_{0.3}MnO_3/La_{0.7}Sr_{0.3}MnO_3$ multilayers grown on $SrTiO_3$ (001) are very similar; both have a paramagnetic/ferromagnetic transition (at about 180 K for $La_{0.7}Sr_{0.3}MnO_3/SrTiO_3$ and at about 250 K for $Pr_{0.7}Ca_{0.3}MnO_3/La_{0.7}Sr_{0.3}MnO_3$), and they can be classified as hard ferromagnets. The difference between the two types of multilayer is that $La_{0.7}Sr_{0.3}MnO_3/SrTiO_3$ has a spin glass behaviour at low temperature (below the PM/FM transition), that makes it a reentrant spin glass; while $Pr_{0.7}Ca_{0.3}MnO_3/La_{0.7}Sr_{0.3}MnO_3$ is a stable ferromagnet with a paramagnetic/ferromagnetic transition at 250 K.

I propose that while in $La_{0.7}Sr_{0.3}MnO_3/SrTiO_3$ multilayers the formation of dead layers at the interfaces, due to the charge transfer, inhibits a good ferromagnetic behaviour, in the case of $Pr_{0.7}Ca_{0.3}MnO_3/La_{0.7}Sr_{0.3}MnO_3$ multilayer, there is a reduction of the dead layer, not being a charge transfer at the interfaces between the two manganites, that gives as global result a stable ferromagnetic behaviour. I want to point out that the reduction of the dead layer in $Pr_{0.7}Ca_{0.3}MnO_3/La_{0.7}Sr_{0.3}MnO_3$ multilayers is a relevant result, resulting functional in the design of new improved spin valves and magnetic tunnel junctions.

In consideration of the results obtained and presented in this PhD Thesis, I can conclude that the techniques are mature for the design and development of new spintronics devices, as a natural development of this work.

Bibliography

[1] G. H. Jonker, J. H. Van Santen, *Physica* **16**, 337 (1950).

[2] P. G. Radaelli, D. E. Cox, M. Marezio, S.-W. Cehong, P. Schifer, A. P. Ramirez, *Phys. Rev. Lett.* **75**, 4488 (1995).

[3] P. G. Radaelli, M. Marezio, H. Y. Hwang, S.-W. Cehong, B. Batlogg, *Phys. Rev. B* **54**, 8992 (1996).

[4] L. Wu, R. F. Klie, Y. Zhu, Ch. Jooss, *Phys. Rev. B* **76**, 174210 (2007).

[5] V. M. Goldschmidt, *Naturwissenschaften* **14**, 477 (1926).

[6] J. P. Zhou, J. T. McDevitt, J. S. Zhou, H. Q. Yin, J. B. Goodenough, Y. Gim Q. X. Jia, *Appl. Phys. Lett.*, **75**, 1146 (1999).

[7] Y. Tokura, *Rep. Prog. Phys.* **69**, 797 (2006).

[8] A. M. Haghiri-Gosnet, J. P. Renard, *J. Phys. D: Appl. Phys.* **36**, R127 (2003).

[9] A. J. Millis, *Theory of CMR Manganites*, in *Colossal Magnetoresistive Oxides*, ed. Y. Tokura, Gordon and Breach, London (1999).

[10] L. P. Gor'kov, V. Z. Kresin, *Physics Reports* **400**, 149 (2004).

[11] H. A. *Jahn,* E. *Teller*, *Proc*. *Roy*. *Soc*. **A161**, 220 (1937).

[12] T. Chatterji, B. Ouladdiaf, P. Mandal, B. Bandyopadhyay, B.Ghosh, *Phys. Rev.* B **66**, 054403 (2002).

[13] S. Mori, C. H. Chen, S.-W. Cheong Nature **392**, 473 (1998).

[14] H. A. Kramers, *Physica* **1**, 182 (1934).

[15] P. W. Anderson, *Phys.Rev.* **79**, 350 (1950).

[16] C. Zener, *Phys. Rev.* **82**, 403 (1951).

[17] P. W. Anderson, H. Hasegawa, *Phys.Rev. B* **100**, 675 (1955).

[18] A. J. Millis, P. B. Littlewood, B. I. Shraiman, *Phys. Rev. Lett.* **74**, 5144 (1995).

[19] A. J. Millis, *Nature* **392**, 147 (1998).

[20] S. Blundell, *Magnetism in condensed matter*, Oxford U.P., New York, (2001).

[21] M. Uehara, S. Mori, C.H. Chen, S.W. Cheong, *Nature* **399**, 560 (1999).

[22] A. Moreo, M. Mayer, A. Feiguin, S. Yunoki, E. Dagotto, *Phys. Rev. Lett.* **84**, 5568 (2000).

[23] K. Dörr, J.M. De Teresa, K.-H. Müller, D. Eckert, T.Walter, E. Vlakhov, K. Nenekov, L. Shultz, *J. Phys: Cond Matt* **12**, 7099 (2000).

[24] D. Saurel, A. Brûlet, A. Heinemann, C. Martin, S. Mercone, C. Simon, *Phys. Rev. B* **73**, 094438 (2006).

[25] Y. Murakami, J. P. Hill, D. Gibbs, M. Blume, I. Koyama, M. Tanaka, H. Kawata, T. Arima, Y. Tokura, K. Hirota, Y. Endoh, *Phys. Rev. Lett.* **81**, 582 (1998).

[26] A. Urushibara, Y. Morimoto, T. Arima, A. Asamitsu, G. Kido, Y. Tokura, *Phys. Rev. B* **51**, 14103 (1995).

[27] S. Quezel-Ambrunaz, *Bull. Soc. Franc. Minér. Crist.* **91**, 339 (1968).

[28] Z. Jirák, S. Krupička, Z. Šimša, M. Dlouhá, S. Vratislav, *J. Magn. Magn. Mat.* **53**, 153 (1985).

[29] J. Barratt, M. R. Lees, G. Balakrishnan, D. McK Paul, *Appl. Phys. Lett.* **68**, 424 (1996).

[30] Y. Tomioka, A. Asamitsu, Y. Moritomo, Y. Tokura, *J. Phys. Soc. Jap.* **64**, 3626 (1995).

[31] M. Fiebig, K. Miyano, Y. Tomioka, Y. Tokura, *Science* **280**, 1925 (1998)

[32] V. Kiryukhin, D. Casa, J.P. Hill, B. Keimer, A. Vigliante, Y. Tomioka, Y. Tokura, *Nature* **386**, 813 (1997).

[33] Y. Moritomo, H. Kuwahara, Y. Tomioka, Y. Tokura, *Phys. Rev. B* **55**, 7549 (1997)

[34] A. Asamitsu, Y. Tomioka, H. Kuwahara, Y. Tokura, *Nature* **388**, 50 (1997).

[35] H. Sha, F. Ye, Pengcheng Dai, J. A. Fernandez-Baca, Dalgis Mesa, J. W. Lynn, Y. Tomioka, Y. Tokura, J. Zhang, *Phys. Rev. B* **78**, 052410 (2008).

[36] F. Rivadulla, M. A. López-Quintela, L. E. Hueso, C. Jardón, A. Fondado, J. Rivas, M. T. Causa, R. D. Sánchez, *Solid State Comm.*, **110**, 179 (1999).

[37] P. G. Radaelli, R. M. Ibberson, D. N. Argyriou, H. Casalta, K. H. Andersen, S.-W. Cheong, J. F. Mitchell, *Phys. Rev. B* **63**, 172419 (2001).

[38] Ch. Jooss, L. Wu, T. Beetz, R. F. Klie, M. Beleggia, M. A. Schofield, S. Schramm, J. Hoffmann, Y. Zhu, *Proc. Natl. Acad. Sci. U.S.A.* **104**, 13597 (2007).

[39] D. Saurel, A. Brulet, A. Heinemann, C. Martin, S. Mercone, C. Simon, *Phys. Rev. B* **73**, 094438 (2006).

[40] M. Rini, R. Tobey, N. Dean, J. Itatani, Y. Tomioka, Y. Tokura, R. W. Schoenlein, A. Cavalleri, *Nature* **449**, 72 (2007).

[41] Z. Jirak, F. Damay, M. Hervieu, C. Martin, B. Raveau, G. Andre, F. Bouree, *Phys. Rev. B* **61**, 1181 (2000).

[42] A. Trokiner, A. Yakubovskii, S. Verkhovskii, A. Gerashenko, D. Khomskii *Phys. Rev. B* **74**, 092403 (2006).

[43] M. Tokunaga, N. Miura, Y. Tomioka, Y. Tokura, *Phys. Rev. B* **57**, 5259 (1998).

[44] K. Chahara, T. Ohno, M. Kasai, Y. Kozono, *Appl. Phys. Lett.* **63**, 1990 (1993).

[45] R. von Hemlolt, J. Wecker, B. Holzapfel, L. Schultz, K. Samwer, *Phys. Rev. Lett.* **71**, 2331 (1993).

[46] J. O'Donnel, M. Onellion, M. S. Rzchowski, J. N. Eckstein, I. Bozovic, *Phys. Rev. B* **54**, R6841 (1996).

[47] J. M. Phillips, *J. Appl. Phys.* **79**, 1829 (1996).

[48] R. Sum, H. P. Lang, H. J. Guntherodt, *Physica C* **242**, 174 (1995).

[49] M. Kawasaki, K. Takahashi, T. Maeda, R. Tsuchiya, M. Shinohara, O. Ishiyama, T. Yonezawa, M. Yoshimoto, H. Koinuma, *Science* **266**, 1540 (1994).

[50] F. S. Galasso, *Perovskites and High T_c Superconductors*, Gordon and Breach, New York, 1990.

[51] G. Koster, G. Rijnders, D. H. A. Blank, H. Rogalla, *Physica C* **339**, 215 (2000).

[52] T. Hikita, T. Hanada, M. Kudo, M. Kawai, *J. Vac. Sci. Technol. A* **11**, 2649 (1993).

[53] M. Radovic, N. Lampis, P. Perna, Z. Ristic, M. Salluzzo, F. Miletto Granozio, U. Scotti di Uccio, C. M. Schlepütz, *Applied Physics Letters,* submitted.

[54] G. Rijnders, The Initial Growth of Complex Oxides: Study and manipulation, Doctoral Thesis, University of Twente, (2001)

[55] A. J. Millis, T. Darling, A. Migliori, *J. Appl. Phys*. **83**, 1588 (1998).

[56] F. Tsui, M. C. Smoak, T. K. Nath, C. B. Eom, *Appl. Phys. Lett.* **76**, 2421 (2000).

[57] T. Kanki, H. Tanaka, T. Kawai, *Phys. Rev.* B **64**, 224418 (2001).

[58] A. Abrutis, V. Plausinaitiene, V. Kubilius, A. Teiserskis, Z. Saltyte, R. Butkute, J. Serateur, *Thin Solid Films* **413**, 32 (2002).

[59] A. Geddo Lehmann, C. Sanna, N. Lampis, F. Congiu, G. Concas, L. Maritato, C. Aruta, A. Yu. Petrov, *Eur. Phys. J. B* **55**, 337 (2007).

[60] A. Tebano, C. Aruta, P. G. Medaglia, F. Tozzi, G. Balestrino, A. A. Sidorenko, G. Allodi, R. De Renzi, G. Ghiringhelli, C. Dallera, L. Braicovich, N. B. Brookes, *Phys. Rev. B* **74**, 245116 (2006).

[61] Y. P. Lee, S. Y. Park, Y. H. Hyun, J. B. Kim, V. G. Prokhorov, V. A. Komashko, V. L. Svetchnikov, *Phys. Rev. B* **73**, 224413 (2006).

[62] C. Aruta, G. Ghiringhelli, A. Tebano, N. G. Boggio, N. B. Brookes, P. G. Medaglia, G. Balestrino, *Phys. Rev. B* **73**, 235121 (2006).

[63] J. Dho, N. H. Hur, I. S. Kim, Y. K. Park, *J. Appl. Phys.* **94**, 7670 (2003).

[64] S. Jin, G. Gao, W. Wu, X. Zhou, *J. Phys. D: Appl. Phys.* **40**, 305 (2007).

[65] J. Dho, Y. N. Kim, Y. S. Hwang, J. C. Kim, N. H. Hur, *Appl. Phys. Lett.* **82**, 1434 (2003).

[66] R. Di Capua, C. A. Perroni, V. Cataudella, F. Miletto Granozio, P. Perna, M. Salluzzo, U. Scotti di Uccio, R. Vaglio, *J. Phys.: Cond. Matter* **18**, 8195 (2006).

[67] M. Mathew, F. M. Postima, J. C. Lodder, R. Jansen, G. Rijnders, D. H. A. Blank, *Appl. Phys. Lett.* **87**, 242507 (2005).

[68] R. V. Demin, L. I. Koroleva, A. M. Balbashov, *J. Magn. Magn. Mater.* **177**, 871 (1998).

[69] L. I. Koroleva, R. V. Demin, A. V. Kozlov, D. M. Zashchirinskii, Ya. M. Mukovskii, *J. Exp. Theor. Phys.* **104**, 76 (2007).

[70] C. Thiele, K. Dorr, O. Bilani, J. Rodel, L. Schultz, *Phys. Rev. B* **75**, 054408 (2007).

[71] M. Fujimoto, H. Koyama, Y. Nishi, T. Suzuki, S. Kobayashi, Y. Tamai, N. Awaya, *J. Am. Ceram. Soc.* **90** 2205 (2007).

[72] I. MacLaren, Z. L. Wang H. S. Wang, Q. Li, *Phil. Mag. A* **82**, 1405 (2002).

[73] W. Prellier, Ch. Simon, A. M. Haghiri-Gosnet, B. Mercey, B. Raveau, *Phys. Rev. B* **62**, R16337 (2000).

[74] W. Prellier, Ch. Simon, B. Mercey, M. Hervieu, A. M. Haghiri-Gosnet, D. Saurel, Ph. Lecoeur, B. Raveau, *J. Appl. Phys.* **89**, 6612 (2001).

[75] A. Maniwa, K. Okano, I. Ohkubo, H. Kumigashira, M. Oshima, M. Lippmaa, M. Kawasaki, H. Koinuma, *J. Mag. Mag. Mat.* **310**, 2237 (2007).

[76] W. Prellier, E. R. Buzin, Ch. Simon, B. Mercey, M. Hervieu, S. de Brion, G. Chouteau, *Phys. Rev. B* **66**, 024432 (2002).

[77] R. K. Zheng, C. Chao, H. L. W. Chan, C. L. Choy, H. S. Luo, *Phys. Rev. B* **75**, 024110 (2007).

[78] Z. Q. Yang, R. W. A. Hendrikx, P. J. M. van Bentum, J. Aarts, *Europhys. Lett.* **58**, 864 (2002).

[79] Z. Q. Yang, Y. Q. Zhang, J. Aarts, M. Y. Wu, H. W. Zandbergen, *Appl. Phys. Lett.* **88**, 072507 (2006).

[80] A. M. Haghiri-Gosnet, M. Hervieu, Ch. Simon, B. Mercey, B. Raveau, *J. Appl. Phys.* **88**, 3545 (2000).

[81] W. Prellier, A. M. Haghiri-Gosnet, B. Mercey, Ph. Lecoeur, M. Hervieu, Ch. Simon, B. Raveau, *Appl. Phys. Lett.* **77**, 1023 (2000).

[82] Y. Q. Zhang, Y. L. Zhu, Z. D. Zhang, J. Aarts, *J. Appl. Phys.* **101**, 063919 (2007).

[83] W. W. Zhuang, W. Pan, B. D. Ulrich, J. J. Lee, L. Stecker, A. Burmaster, D. R. Evans, S. T. Hsu, M. Tajiri, A. Shimaoka, K. Inoue, T. Naka, N. Awaya, K. Sakiyama, Y. Wang, S. Q. Liu, N. J. Wu, A. Ignatiev, *IEDM Tech. Dig.* 193 (2002).

[84] I. G. Baek, M. S. Lee, S. Seo, M. J. Lee, D. H. Seo, D. S. Suh, J. C. Park, S. O. Park, H. S. Kim, I. K. Yoo, U. I. Chung, J. T. Moon, *IEDM Tech. Dig.* 587 (2004).

[85] X. Chen, N. J. Wu, J. Strozier, A. Ignatiev*, Appl. Phys. Lett.* **87**, 233506 (2005).

[86] D. Dijkkamp, T. Venkatesan, X. D. Wu, S. A. Shaheen, N. Jisrawi, Y. H. Min-Lee, W. L. Mclean, M. Croft, *Appl. Phys. Lett*. **51**, 619 (1987).

[87] A. Inam, M. S. Hegde, X. D. Wu, T. Venkatesan, P. England, P. F. Miceli, E. W. Chase, C. C. Chang, J.-M. Tarascon, J. B. Wachtman, *Appl. Phys. Lett*. **53**, 908 (1988).

[88] D. B. Chrisey, G. K. Hubler, *Pulsed laser deposition of thin films*, John Wiley & Sons (1994).

[89] CASA XPS software, version 2.3, CASA Software Ltd., U.K..

[90] O. I. Klyushnikov, V. V. Sal'nikov, N. M. Bogdanovich, *Inorg. Mater.* **38**, 261 (2002).

[91] P. Decorse, E. Quenneville, S. Polulin, M. Meunier, A. Yelon, F. Morin, *J. Vac. Sci. Technol. A* **19**, 910 (2001).

[92] J. Liang, H. Weng, *Ind. Eng. Chem. Res.* **32**, 2563 (1993).

[93] J. H. Scofield, *J. Electron Spectrosc. Relat. Phenom.* **8**, 129 (1976).

[94] R. F. Reilman, A. Msezane, S. T. Manson, *J. Electron Spectrosc. Relat. Phenom.* **8**, 389 (1976).

[95] M.P. Seah, W.A. Dench. *Surf. Interf. Anal.* **1**, 2 (1979).

[96] P. Ruffieux, P. Schwaller, O. Gröning, L. Schlapbach, P. Groning, Q. C. Herd, D. Funnemann, J. Westermann, *Rev. Sci. Instrum.* **71**, 3634 (2000).

[97] M. Izumi, Y. Konishi, T. Nishihara, S. Hayashi, M. Shinohara, M. Kawasaki, Y. Tokura, *Appl. Phys. Lett.* **73**, 2497 (1998).

[98] LEPTOS software, version 2.03, Bruker-AXS, Karlsruhe, Germany.

[99] S. K. Pandey, A. Kumar, S. M. Chaudhari, A. V. Pimpale, *J. Phys.: Condens. Matter* **18**, 1313 (2006).

[100] S. K. Pandey, R. Bindu, P. Bhatt, S. M. Chaudhari, A. V. Pimpale, *Physica B* **365**, 47 (2005).

[101] J. R. L. De Almeida, D. J. Thouless, *J. Phys. A* **11**, 983 (1978).

[102] J. A. Mydosh, *Spin Glasses - An experimental introduction,* Taylor and Francis, London, UK (2003).

[103] S. Chatterjee, A. K. Nigam, *Phys. Rev. B* **66**, 104403 (2002).

[104] B. Martinez, X. Obradors, Ll. Balcells, A. Rouanet, C. Monty, *Phys. Rev. Lett.* **80**, 181 (1998).

[105] A. Ito, *Riken Review* **27,** 18 (2000).

[106] T. Zhu, B. G.Shen, J. R.Sun, H. W. Zhao, W. S. Zhan, *Appl. Phys. Lett.* **78**, 3863 (2001).

[107] X. S. Wu, W. Cai, X. P. Zhang, Y. G. Zhao, L. Lu, *J. Phys.: Condens. Matter* **17**, 6981 (2005).

[108] G. Cao, J. Zhang, S. Wang, J. Yu, C. Jing, S. Cao, X. Shen, *J. Magn*. *Magn*. Mater. **301**, 147 (*2006*).

[109] A. Maignan, C. Martin, F. Damay, B. Raveau, *Z. Phys. B: Condens. Matter* **104**, 21 (1997).

[110] J. M. De Teresa, M. R. Ibarra, J. Garcia, J. Blasco, C. Ritter, P. A. Algarahel, C. Marquina, A. Del Moral, *Phys. Rev. Lett.* **76**, 3392 (1996).

[111] A. Sundaresan, A. Maignan, B. Raveau, *Phys. Rev. B* **55**, 5596 (1997).

[112] A. Maignan, U. V. Varadaraju, F. Millange, B. Raveau, *J. Magn. Magn. Mater.* **168**, L237 (1997).

[113] M. Izumi, Y. Ogimoto, Y. Okimoto, T. Manako, P. Ahmet, K. Nakajima, T. Chikyow, M. Kawasaki, Y. Tokura, *Phys. Rev. B* **64**, 064429 (2001).

[114] M. Izumi, Y. Ogimoto, T. Manako, M. Kawsaki, Y. Tokura, *J. Phys. Soc. Jpn.* **71**, 2621 (2002).

[115] D. Niebieskikwiat, L. E. Hueso, M. B. Salamon, N. D. Mathur, *J. Appl. Phys.* **99**, 08C903 (2006).

[116] D. Niebieskikwiat, L. E. Hueso, J. A. Borchers, N. D. Mathur, M. B. Salamon *Phys. Rev. Lett.* **99**, 247207 (2007).

[117] S. Mukhopadhyay, I. Das, *EPL* **83**, 27003 (2008).

[118] D. V. Efremov, J. van den Brink, D. I. Khomskii, *Nature Mater.* **3**, 853 (2004).

Ringraziamenti

Desidero ringraziare tutti coloro che mi hanno permesso di realizzare questo lavoro di ricerca.

In particolare ringrazio il Prof. Ruggero Vaglio e il Prof. Umberto Scotti di Uccio, supervisori della mia tesi di dottorato, per quanto mi hanno dato sia sul piano scientifico che umano.

Un grazie particolare al Dott. Milan Radovic, che ha preparato i campioni che ho caratterizzato in questa tesi, senza il quale quindi questo lavoro non sarebbe stato possibile.

Ringrazio tutto il gruppo del laboratorio Moda in particolare il Dott. Fabio Miletto, per i suoi preziosi consigli, il Dott. Marco Salluzzo, la Dott.ssa Gabriella De Luca, il Dott. Roberto di Capua, il Dott. Paolo Perna e il Dott. Zoran Ristic per le sempre interessanti discussioni scientifiche e per il loro incoraggiamento nei momenti di difficoltà.

Ringrazio tutto il gruppo di Cagliari, in particolare la Dott.ssa Alessandra Geddo Lehmann per i suoi consigli sempre puntuali e preziosi, il Dott. Franco Congiu, il Dott. Danilo Addari e il Dott. Francesco Scano per il supporto e le utilissime discussioni scientifiche.

Ringrazio inoltre, il Dott. Andrea Falqui e la Dott.ssa Claudia Cantoni per le misure di microscopia.

Ringrazio tutti i miei amici che mi hanno incoraggiato nei momenti di pessimismo.

Un grazie particolare va a mio nonno Michele, che occuperà sempre un posto speciale nel mio cuore, e ai miei zii Gianni, Maria Teresa e Rita che non mi hanno mai fatta sentire sola, riempiendomi di ogni attenzione durante la mia permanenza in Campania.

Un ringraziamento enorme va a mio marito Massimiliano, che mi ha sempre incoraggiata in questa esperienza, nonostante i sacrifici che ci ha richiesto.

Infine un grazie ai miei genitori, Annamaria e Giorgio, e ai miei fratelli, Christian e Massimiliano, che mi sono sempre vicini, facendomi sentire coccolata ed amata.